# Study of the thermosalient effect in N’-2-Propylidene-4-hydroxybenzohydrazide and the derivatives of oxitropium bromide

**Klaser, Teodoro**

**Doctoral thesis / Disertacija**

**2021**

*Degree Grantor / Ustanova koja je dodijelila akademski / stručni stupanj:* **University of Zagreb, Faculty of Science / Sveučilište u Zagrebu, Prirodoslovno-matematički fakultet**

*Permanent link / Trajna poveznica:* https://urn.nsk.hr/urn:nbn:hr:217:537975

*Rights / Prava:* In copyright / Zaštićeno autorskim pravom.

*Download date / Datum preuzimanja:* **2024-03-29**




*Repository / Repozitorij:*

Repository of the Faculty of Science - University of Zagreb








University of Zagreb

Faculty of Science

Department of Physics

Teodoro Klaser

# Study of the thermosalient effect in *N*'-2-Propylidene-4-hydroxybenzohydrazide and the derivatives of oxitropium bromide

DOCTORAL THESIS

Supervisor:

Associate professor, Željko Skoko, PhD

Zagreb, 2021



Sveučilište u Zagrebu

Prirodoslovno-matematički fakultet

Fizički odsjek

Teodoro Klaser

# Istraživanje termoodskočnog efekta u *N*'-2-Propiliden-4-hidroksibenzohidrazidu i derivatima oksitropium bromida

DOKTORSKI RAD

Mentor:

izv. profesor dr. sc. Željko Skoko

Zagreb, 2021

## Supervisor CV

Dr. sc. **Željko Skoko** is an associate professor at the Department of Physics, Faculty of Science, University of Zagreb. He graduated physics at the Department of Physics of the Faculty of Science in 2000, where he also received his PhD. in 2008. He was employed as an assistant at the Department of Physics in 2000 and was elected assistant professor in 2010. Between 2009 and 2010 he was a postdoc fellow at Osaka University in Osaka, Japan, where he was elected a specially appointed assistant professor.

The main areas of his scientific interest are experimental physics of condensed matter, powder and single crystal X-ray diffraction, structural and microstructural studies, electron microscopy, thermosalient and photosalient materials, metals and alloys, functional and doped metal oxides, and energy storage materials.

As of March 2021, he had published 53 scientific papers which were cited 834 times, with an h-index of 15. He delivered 20 oral presentations at international and domestic scientific conferences, one of which was plenary and three invited. He also presented three invited lectures at domestic and foreign institutions. He was the principal investigator of two Croatian Science Foundation projects (research project and career development project for young researchers), one scientific research project of the Ministry of Science, Education and Sports, three bilateral projects, and six projects of the Croatian Academy of Sciences and Arts Foundation. He has been a collaborator on numerous competitive scientific research projects.

He was a supervisor of two doctoral dissertations and has mentored eighteen graduate theses and one postdoctoral fellowship, as well as two student research projects that were awarded the Rector's Award. He is the Head of the Laboratory for microstructural investigations at the Department of Physics, a member of the Board of the Croatian Crystallographic Society, the Board of the Croatian Microscopic Society, and one of the founders of the Croatian Association of Crystallographers. Also, he holds a position of the Head of the State Commission for Competition in Physics. He was the chair of the organizing and scientific committee of one international scientific conference and a member of the organizing and scientific committees of a dozen international scientific conferences.

He holds six courses in undergraduate and graduate studies at the Departments of Physics and Mathematics of the Faculty of Science, and three courses in doctoral studies at the Departments of Physics and Chemistry.

# Acknowledgments

*I am most grateful to my parents, Đuzepe and Gordana, and my brother Klaudijo who have always been there for me, supporting and advising me. Without them, this work would have never been completed.*

*I have read once, while considering my further career in the research field: "Your PhD supervisor will be one of the most influential people in your academic life. Throughout the course of your doctorate, your supervisor will play the role of mentor, confidant, cheerleader, and advisor. They will be crucial to your PhD's success so it's important to make a prudent choice." Now, I can definitely say, I was so lucky to have made the best possible choice. That choice is Željko, he introduced me to the field of X-ray powder diffraction in the solid-state physics and thought me how to properly conduct my research work. He inspired me to broaden my scientific horizons and encouraged me to present my results with greatest passion. Thanks for everything, Željko! I am very grateful to Jasminka, without her help with interpretation of data, especially from the chemical point of view, this work would not be so powerful. Thank you, a lot, Jasminka!*

*I am also grateful to all of friends that I made during my PhD studies that have helped me during my research and my studies. Thank you, Filip, for sharing with me your technical knowledge in the laboratory. Nenad, thank you for your help with the programming and revision of my Croatian. Thank you, Oskar, for your help in laboratory work with sample preparation and analysis. But among all, I am most grateful to you guys for your friendship which was so very important for me during my stay at the Department of physics.*

*I would also like to thank all the staff at the Department but especially Dražen and Ivan, who made my days at the Department jolly funny and full of laughter. Thanks also to Jasna and Marko who helped me with the administrative part, always with much patience.*

*At the end, I must thank my dearest Teja, meeting her slowed down my PhD thesis writing pace but gave me the greatest energy and love that I have needed to finish it.*

*Teodoro*

## Abstract

Thermosalient materials, or more colloquially called *jumping crystals*, are a class of materials that exhibit mechanical motion as a response to the thermal stimulus. Such materials, which are capable of extremely fast and, more important, controllable energy conversion are extremely important candidates for active actuating elements, such as flexible electronic switches, displays, artificial muscles, microfluidic valves and gates, heat sensors etc. New examples of thermosalient materials are emerging on a daily basis but yet, due to the exclusivity and individuality of the phenomenon, plus the complexity of analytical methods for its characterization, the reasons behind this colossal self-actuation remain unexplained and this thesis aims to address this lack of understanding.

In this thesis two thermosalient systems, *N*'-2-propylidene-4-hydroxybenzohydrazide and oxitropium bromide, as well as their derivatives were extensively studied. In the case of *N*'-2-propylidene-4-hydroxybenzohydrazide, existence of the negative linear compressibility was experimentally proven and as well as its coupling to the negative thermal expansion. Raman measurements proved the previous theoretical suggestion of the phonon softening while approaching phase transition, and this softening helps the system transform from one thermosalient phase to another. Also, the mechanism of negative thermal expansion – the main reason for the existence of the thermosalient effect - and negative linear compressibility was fully determined.

Oxitropium bromide was extensively studied in this thesis regarding its thermal behaviour prior to the polymorphic phase transition, once again proving the need of the negative thermal expansion for thermosalient properties. Two of its derivatives were prepared: scopolamine bromide hydrate and scopolamine bromide which exhibited thermosalient effect based on two novel mechanisms, previously not reported in the literature. Jumping of the crystals of scopolamine bromide hydrate is caused by the release of the water from the crystal lattice, whereas the crystals of the scopolamine bromide jump without any phase transition or chemical change and its mechanism is not yet understood.



### Key words

*Thermosalient effect; jumping crystals; X-ray powder diffraction; Non-ambiental measurements; Negative thermal expansion; Negative linear compressibility; Wine-rack motive; Microactuators; Artificial muscles; N'-2-propylidene-4-hydroxybenzohydrazide; Oxitropium bromide: High-pressure X-ray diffraction; Hot-stage microscopy; Raman spectroscopy; Density functional theory (DFT); Phase transitions.*

# PROŠIRENI SAŽETAK

## Uvod

Termoodskočni kristali su jedinični kristali za koje se smatra da su kandidati za aktivne aktuatorske elemente u organskim mikrouređajima. Pojam "*termoodskočni učinak*" prvi su put 1983. godine upotrijebili Etter i Siedle, promatrajući skakanje kristala (fenilazofenil)paladij heksafluoroacetilacetonata. [1] Kristali, naravno, reagiraju na različite načine kada su izloženi promjenama temperature, tlaka, kemijskog okruženja ili svjetlosti. Kada se kristali podvrgnu grijanju ili hlađenju, očekuje se da dolazi do kemijskih reakcija poput oksidacije ili termičkog raspada, ili pak do neke fizičke promjene poput faznih prijelaza, sublimacije ili taljenja, ali izuzetno je egzotično kada kristali, zbog dovođenja toplinske energije, počnu skočiti. U znanstvenoj dano je nekoliko primjera organskih [2] [3] [4] ali i anorganskih kristala [5] koji iskazuju ovo osebujno ponašanje prilikom temperaturnih faznih pretvorbi. Poskakivanje ili skakanje kristala, vidljivo na makroskali, obično je povezano s termički izazvanim polimorfnim faznim prijelazom iz niskotemperaturne forme u visokotemperaturnu formu. Ovakvi materijali koji pružaju mehanički odgovor na promjenu temperature nazivaju se termoodskočni materijali, ili kolokvijalno nazvani "skočikristali". [6] Osim što je vizualno atraktivan i općenito vrlo zabavan, ovaj je učinak posebno važan i sa znanstvenog i s tehnološkog gledišta, budući da ti materijali predstavljaju medije za pretvorbu toplinske energije u mehanički rad. Često, iako su poznate strukture obje termoodskočne faze (niskotemperaturne i visokotemperaturne), makrostrukturne manifestacije koje prate taj fazni prijelaz ostaju značajna misterija. Većina termoodskočnih faznih prijelaza su topotaktički i izosimetrični. Kristalne strukture dvaju polimorfa (prije i nakon faznog prijelaza) vrlo su slične. Neznatno različito pakiranja i neki pomaci dijelova molekula dijelova dovode do dramatičnih promjena u parametrima jediničnih ćelija (10% ili više).

Termoodskočni materijali među najbržim su materijalima u smislu brzine fazne pretvorbe koja je martenzitnog tipa i uključuje kolektivno gibanje molekula i dešava se $10^4$-$10^5$ puta brže od ostalih, nekooperativnih, prijelaza u istim ili drugim materijalima. Na primjer, brzina gibanja ravnine među termoodskočnim fazama u (fenilazofenil)paladij heksafluoracetilacetonatu je 0,54 m $s^{-1}$, što odgovara broju od 1,227 × $10^9$ molekula po sekundi koje doživljavaju pretvorbu. Ova brzina gibanja četiri je reda veličine brža od brzine drugog, ne-termoodskočnog prijelaza u ovom materijalu gdje se ravnina među fazama kreće brzinom

$4{,}34 \times 10^{-5}$ m $s^{-1}$ i $1{,}026 \times 10^{5}$ transformiranih molekula u sekundi. Ova brzina također je mnogo veća od uobičajenih spin-crossover prijelaza (niski spin-visoki spin), koji se događaju na vremenskoj skali od $10^{-5}$ m $s^{-1}$.[7] Jedan od najintrigantnijih aspekata termoodskočnih materijala povezan je s jednim neobičnim svojstvom u fizici čvrstog stanja - prisutnost negativnog toplinskog rastezanja u korelaciji s negativnom kompresibilnosti s vrijednostima koje su obično red veličine veće u odnosu na tipične organske, a čak i anorganske materijale. Vrijednosti (negativnih) koeficijenata kompresibilinosti u termoodskočnim materijalima usporedive se samo s onima od molekulskih mreža, klase spojeva koji iskazuju najizraženije ponašanje negativne linearne kompresibilnosti. [9]

U ovoj disertaciji korišten je sinergijski pristup koji kombinira opsežne eksperimentalne metode i teorijske proračune, a usmjeren je, ne toliko na trenutak same termoodskočne fazne pretvorbe, već na procese koji prethode manifestaciji termoodskočnog učinka, posebno na ulogu negativnog toplinskog rastezanja u mehanizmu termoodskočnog učinka i njegove korelacija s negativnom linearnom kompresibilnosti, ali također i s važnosti niskoenergetskih fonona koji potpomažu u faznom prijelazu. Istraživanja u ovoj disertaciji usmjerena su prema dvjema, uvjetno rečeno, različitim ciljnim skupinama termoodskočnih spojeva; prvo, *na materijale u kojima je učinak već poznat i uočen* i drugo, *na potencijalne termoodskočne materijale koji su kemijski / strukturno / funkcionalno slični materijalima s utvrđenim termoodskočnim učinkom*. *N*'-propiliden-4-hidroksibenzohidrazid je materijal u kojem je opažen termoodskočni učinak, ali nije u potpunosti razriješen. Iz pregleda dosada provedenog istraživanja očito je da još uvijek treba potvrditi (ili odbiti) dvije pretpostavke: (*i*) postojanje negativne linearne kompresibilnosti a i (*ii*) važnost uloge niskoenergetskih fonona u termoodskočnim faznim pretvorbama. Budući da se mehanizam koji stoji iza termoodskočnog učinka ne može u potpunosti objasniti na temelju do sada obavljenih pokusa, a zasigurno ga nije moguće predvidjeti, smatrali smo potrebnim proširiti istraživanja na skupinu spojeva dobivenih odabranom i pažljivom modifikacijom spojeva u kojem je prethodno potvrđeno postojanje učinka. Za očekivati je da će termoodskočni učinak biti izuzetno osjetljiv na suptilne promjene kemijskog sastava (promjena aniona, promjena funkcionalne skupine, promjena broja funkcionalnih skupina, promjena položaja funkcionalnih skupina unutar aromatskog prstena) i ova ispitivanja termoodskočnih derivata imala su za cilj utvrđivanje specifičnih kemijskih / strukturnih parametara potrebnih za termoodskočno ponašanje. Predstavnik druge skupine, derivatne skupine, je oksitropijum bromid. Važno je naglasiti da glavni cilj nije bio, nužno, dobivanje novih termoodskočnih spojeva, već

prikupljanje što više informacija o spojevima koji su dobiveni modifikacijom trenutnih termoodskočnih spojeva. Smatrali smo da bez obzira pokazuju li novi spojevi termoodskočno ponašanje ili ne, usporedba podataka o izvornim termoodskočnim materijalima s podacima o njihovim derivatima u svakom će slučaju pomoći u rasvjetljavanju faktora odgovornih za postojanje termoodskočnog učinka te nam pružiti smjernice za modeliranje novih termoodskočnih materijala.

Na prvi pogled istraživanje termoodskočnih materijala čini se zabavnim, proučavanje ovog primamljiv učinka, s kristalima koji radosno skaču uokolo, baš kao vrećica kokica. No, ulazeći dublje u finese ovog fascinantnog efekta, otkriva se da zapravo postoji složeni pozadinski mehanizam odgovoran za skakanje kristala koji zahtijeva upotrebu velikog broja eksperimentalnih i teorijskih metoda koje leže na granici između fizike, kemije, kristalografije, matematike i inženjerstva materijala.

## Eksperimentalne i teorijske metode

### Rendgenska difrakcija

Rendgenska difrakcija je nedestruktivna tehnika za strukturnu karakterizaciju kristalnih materijala. Temelji se na činjenici da se rendgenske zrake raspršuju pod određenim kutovima na skupovima mrežnih ravnina unutar uzorka i konstruktivnom interferencijom ovih zraka dolazi do stvaranja difrakcijskih maksimuma. Ova metoda pruža informacije o kristalnoj strukturi, fazama, preferiranoj orijentaciji kristalita (teksturi) i ostalim strukturnim parametrima, kao što su prosječna veličina kristalita, kristalnost, deformacije i kristalni defekti. Valna duljina rendgenskih zraka koje se koriste u eksperimentu je reda Ångströma (1 Å = $10^{-10}$ m) što se podudara s tipičnom međuatomskom udaljenošću u kristalu. Elektronska gustoća se može rekonstruirati iz difrakcijske slike dobivene raspršenjem rendgenskih zraka na periodičkom uređenju molekula ili atoma u kristalu. U ovom radu korištene su dvije difrakcijske tehnike: (i) rendgenska difrakcija u polikristalu i (ii) rendgenska difrakcija u jediničnom kristalu. Podaci dobiveni rendgenskom difrakcijom u polikristalu utočnjavani su Rietveldovom metodom, koja koristi pristup najmanjih kvadrata s ciljem utočnjavanja teorijskog difrakcijskog maksimama dok se ne postigne podudaranje s mjerenim maksimumom. Ova metoda prvenstveno je primijenjena na utočnjavanje maksimuma dobivenih neutronskom difrakcijom ali se vrlo uspješno koristi i na podatke dobivene rendgenskom difrakcijom. Informacije dobivene utočnjavanjem podataka rendgenske difrakcije u polikristalu su nešto nepreciznije od informacija dobivenih iz podataka rendgenske

difrakcije u jediničnom kristalu budući da se trodimenzionalne informacije iz recipročne rešetke komprimiraju u jednu dimenziju kod difrakcijske slike iz polikristala.
U okviru ove disertacije obavljani su difrakcijski eksperimenti pri različitim neambijentalnim uvjetima: pri niskoj temperaturi, visokoj temperaturi, te pod visokim tlakom.

### Termičke metode

Termičke tehnike, poput diferencijalne termičke analize ili diferencijalne pretražne kalorimetrije, temelje se na kalorimetrijskoj analizi i koriste se za proučavanje promjena u tvari u ovisnosti o temperaturi. [53] Diferencijalna pretražna kalorimetrija detektira endotermne i egzotermne prijelaze, i služi određivanje temperatura pretvorbi i entalpije krutina i tekućina u ovisnosti o temperaturi. Za razliku od klasične kalorimetrije, gdje se uzorak stavlja u izoliranu komoru kako bi se nadziralo njegovo primanje i otpuštanje topline u izotermnom eksperimentu, diferencijalna pretražna kalorimetrija dinamičan je postupak. Tipični kalorimetar je izolirana komora u kojoj se uzorak stavlja u okolni medij. Tada se uzorak zagrijava s određenom količinom topline. Razlika u temperaturi između uzorka i okolnog medija daje toplinski kapacitet uzorka i informacije o oslobađanju topline. Osim toga, tehnika diferencijalnog pretraživanja koristi uzorak i referencu koji se nalaze pod istim uvjetima i njihovi se signali izravno oduzimaju jedan od drugog. To omogućuje otkrivanje prijelaza kao što su otapanja, amorfizacija i fazne pretvorbe.

### Micro Ramanova spektroskopija

Ramanova spektroskopija je nedestruktivna tehnika koristi za utvrđivanje kemijskih veza u različitim materijala i utvrđivanje njihovih molekulskih simetrija. Osnovni princip Ramanove spektroskopije leži u obasjavanju uzorka monokromatskim svjetlom lasera i analizi spektralnog pomaka upadne svjetlosti koja je raspršena na uzorku. [54] Podaci dobiveni ovom metodom proizlaze iz procesa raspršenja svjetlosti koji pružaju informacije o među- i unutar-molekularnim vibracijama i mogu se koristiti za daljnje razumijevanje kemijskih reakcija. Također se može koristiti za dobivanje određenih vibracija molekule (molekularni otisak) koje se koriste za identifikaciju uzorka. Za istraživanje malih područja, laser se može propustiti kroz optički mikroskop, smanjujući tako površinu uzorka. Ova se tehnika općenito naziva mikro-Raman.

### Teorija funkcionala gustoće

Teorija funkcionala gustoće (*eng*. density functional theory, DFT) jedna je od najčešće korištenih metoda za *ab initio* proračune strukture atoma, molekula, površina kristala i njihovih interakcija. DFT ima dvije glavne prednosti u usporedbi s Hartree-Fock metodom, naime može se u dovoljnoj mjeri nositi s problemima mnoštva čestica s velikom točnošću, a računski je relativno jednostavna. DFT se koristi u problemima klasičnih sustava točkastih čestica s interakcijama, obično elektronskih sustava. Slobodna energija i particijska funkcija ovise o funkciji potencijala, a ne o skalarnom volumenu, i u tom smislu slobodna energija je funkcional. Tijekom godina razvijene su mnoge različite primjene DFT-a budući da znanje o energiji elektronskog osnovnog stanja kao funkciji položaja atomskih jezgri određuje molekulsku i kristalnu strukturu i daje sile koje djeluju na atomske jezgre kad nisu u ravnotežnim položajima. Danas se DFT rutinski koristi za rješavanje problema u fizici kondenzirane tvari kao što su strukture kristalnih rešetaka [55], fazni prijelazi u krutinama [56] i tekućim metalima. [59] Važno je naglasiti da DFT postaje izuzetno važan u problemima koji uključuju velike molekule. [60] Računska snaga (i posljedično vrijeme potrebno za izračune) potrebna za konvencionalne proračune kvantne fizike / kemije raste eksponencijalno s brojem elektrona koji se pojavljuju u problemu, dok u DFT-u ona raste s trećom potencijom ovog broja. U praksi to znači da se DFT može nositi s problemima koji uključuju stotine atoma, dok su konvencionalni kvantni izračuna ograničeni na samo nekoliko atoma.

## Rezultati i rasprava

U ovoj je disertaciji istraživano nekoliko termoodskočnih sustava i riješeno je nekoliko problema. Počeli smo s *N*'-2-propiliden-4-hidroksibenzohidrazidom, tipičnim predstavnikom termoodskočnih materijala koji je opsežno proučavan, ali najvažniji zaključci o mehanizmu termooskočnog učinka u ovom sustavu dobiveni su na temelju teorijskih proračuna putem DFT-a. Skoko i suradnici [9] predložili su da je negativno toplinsko rastezanje - koje je prisutno u gotovo svim termoodskočnim materijalima i za koje se smatra da je glavna pokretačka sila termoodskočnimnim učinkom - posljedica još jedne neuobičajene osobine - negativne linearne kompresibilnosti. Nadalje, ireverzibilnost fazne pretvorbe iz Forme I u Formu II i reverzibilnost faznih prijelaza između Formi II i III objašnjeni tako da se ti fazni prijelazi odvijaju na način da sustav a prolazi kroz put s najmanje naprezanja. U disertaciji je eksperimentalno dokazano postojanje negativne linearne kompresibilnosti, kao i sprega negativne kompresibilnosti s negativnim toplinskim rastezanjem. Ovo je bio vrlo uzbudljiv

trenutak jer nas je to navelo do ideje da je zapravo negativna linearna kompresibilnost razlog termoodskočnog efekta. Mjerenja Ramanovom spektroskopijom potvrdila su teoretsku pretpostavku omekšavanja fononskih modova pri približavanju sustava faznom prijelazu, a upravo to omekšavanje pomaže sustavu da se prijeđe iz jedne termoodskočne faze u drugu. Nadalje, istraživanja propagacije zvuka u ovom sustavu potvrdila su da njegova elastična svojstva određuju reverzibilnost / nepovratnost faznih pretvorbi koje se ovdje dešavaju. I konačno, mehanizam negativnog toplinskog rastezanja i negativne linearne kompresibilnosti u potpunosti je razjašnjen.

Nakon toga istražen je derivat *N*'-2-propiliden-4-hidroksibenzohidrazida, 4-hidroksibenzohidrazid. Pokazano je da ovaj spoj ne pokazuje teermodskočno ponašanje i time je potvrđena naša pretpostavka da prisutnost međusobno penetrirajućih *cik-cak* lanaca, nalik oprugama, koji čine 3D „*wine-rack*" mrežu ima ključnu ulogu u manifestaciji termoodskočnog učinka u *N*'-2-propiliden-4-hidroksibenzohidrazid. Napokon, obavljeno je nekoliko rekristalizacija iz različitih otapala. Rekristalizacijom is mješavine acetona i diklorometanau omjeru 1:1 dobivena smjesa kristala Formi II i Forme III, što samo pokazuje kako su procesi kristalizacije različitih polimorfnih formi izuzetno osjetljivi na uvjete i da o tim procesima još uvijek moramo puno naučiti .

Nakon ove točke prešli smo na proučavanje termoodskočnog učinka u oksitropijum bromidu i njegovim derivatima, nadajući se da ćemo i u njima otkriti negativnu linearnu kompresibilnost, te njenu spregu s negativnim toplinskim rastezanjem. Oksitropijum bromid opsežno je proučavan u ovoj disertaciji s obzirom na njegovo toplinsko ponašanje prije polimorfnog faznog prijelaza. Utvrđivanje negativnog toplinskog rastezanja nije bilo iznenađujuće, i nanovo je potvrdilo našu tezu da je to upravo to svojstvo glavni razlog termoodskočnognog učinka. Kao i u svim ostalim termoodskočnim sustavima, koeficijenti toplinskog rastezanja bili su neuobičajeno veliki. Naši teorijski izračuni sugerirali su da u ovom sustavu nema negativne linearne kompresibilnosti, pa je naša ideja o negativnoj linearnoj kompresibilnosti kao odgovornoj za termoodskočni učinak postala upitna. Ali, možda su teoretski izračuni bili pogrešni? Naša analiza širenja zvuka pokazala je da se perturbacija kreće izuzetno brzo u oksitropijum bromidu te da je protok energije vrlo fokusiran i bez divergencije te da uključuje i niskofrekventne fonone, što potvrđuje pretpostavku da je termoodskočni učinak uzrokovan skupnim gibanjem molekule u kristalu s izuzetno brzim faznim prijelazom prilikom kojeg dolazi do oslobađanja velike količine energije. U posljednjem koraku, u potpunosti je objašnjen mehanizam negativnog toplinskog rastezanja u oksitropijum bromidu.

U sljedećem koraku pripremljen je skopolamin bromid hidrat. To se pokazalo vrlo oportunim budući je ovo prvi put da je u literaturi objavljen novi, drugačiji, mehanizam termoodskočnog učinka. U suprotnosti s ostalim termoodskočnim materijalima, gdje je skakanje kristala uzrokovano stvaranjem naprezanja u kristalnoj rešetki zbog zagrijavanja, a koje se naglo oslobađa tijekom izrazito anizotropnog polimorfnog faznog prijelaza, u ovom je sustavu skakanje kristala izazvano izlaskom vode iz kristalne rešetke. Iznenađujuće, dehidracija je kontinuirani proces, pa se skakanje kristala odvija u širokom temperaturnom intervalu od oko 20 °C. U ostalim termoodskočnim materijalima to se događa u temperaturnom intervalu od oko 5 °C. Ali, kao i kod ostalih termoodskočnih materijala, negativno toplinsko rastezanje također je značajka skopolamin bromid hidrata.

Posljednji, i najintrigantniji, slučaj istražen u ovoj disertaciji bio je slučaj skopolamin bromida. U ovom je sustavu uočen još jedan mehanizam termoodskočnog učinka, koji još nije objavljen u literaturi. Sva mjerenja, strukturna i toplinska, pokazuju da u ovom sustavu ne dolazi do faznog prijelaza, niti bilo kakve kemijske promjene (kao npr. u slučaju skopolamin bromid hidrata), a ipak kristali više puta skaču u širokom temperaturnom intervalu od oko 20 °C. Trenutno mehanizam termooskočnog učinka u ovom sustavu nije razjašnjen. Kao i u svim ostalim termoodskočnim materijalima, ovdje je prisutno negativno toplinsko rastezanje. Pretpostavljamo da kao i kod ostalih termoodskočnih materijala, to dovodi do vrlo anizotropne promjene jedinične ćelije što nadalje stvara velike napetosti u kristalnoj rešetki, i ta energija se u jednom trenutku, vrlo brzo, oslobađa u obliku skokova kristala. Ali za razliku od ostalih termoodskočnih materijala, ovdje se to događa bez faznog prijelaza. DFT izračuni u ovom sustavu su također predvidjeli da ne postoji negativna linearna kompresibilnost, stoga smo odlučili eksperimentalno provjerili točnost ovog rezultata. Eksperimenti rendgenske difrakcije pod visokim tlakom doista su pokazali da skopolamin bromid iskazuje pozitivnu kompresibilnost. To je bio konačni dokaz da negativna linearna kompresibilnost nije nužan uvjet za postojanje termoodskočnog učinka i da ne postoji sprega između negativne kompresibilnosti i negativnog toplinskog rastezanja.

## Zaključak

U zaključku, pokazali smo da svi istraženi termoodskočni materijali posjeduju svojstvo negativnog toplinskog rastezanja, što potvrđuje naše pretpostavke da je upravo to svojstvo upravljačka sila koja stoji iza ovog mehanizma. Negativno toplinsko rastezanje omogućava veliku i anizotropnu promjenu jedinične ćelije, što nadalje izaziva naprezanja u kristalnoj

rešetki. U tom procesu dolazi do akumulacije velike elastične energije koja se u jednom trenutku vrlo brzo oslobađa, što izaziva skakanje kristala. Ovo se uobičajeno dešava tijekom polimorfnog faznog prijelaza. Pronašli smo još dva mehanizma termoodskočnog učinka, koji još nisu spomenuti u literaturi. U jednom slučaju skakanje kristala uzrokovano je izlaskom otapala iz kristalne rešetke. U drugom slučaju, kristali skaču bez da u sustavu dolazi do fazne pretvorbe ili kemijske promjenu. U budućnosti bismo se trebali usredotočiti na pronalazak novih termoodskočnih materijala koji bi dodatno proširili naše znanje o ovom fascinantnom učinku. Tak kada ga u potpunosti razumijemo, moći ćemo izrađivati termoodskočne materijale s vrlo prilagodljivim svojstvima što će omogućiti njihovu upotrebu u stvarnom životu.

# TABLE OFCONTENTS

1. STATE OF THE ART ..... 1
1. 1. Introduction ..... 1
1. 2. Thermosalient materials ..... 4
1. 3. Thermal expansion of materials ..... 12
1.3.1. Grüneisen parameter and thermodynamic proprieties ..... 16
1.3.2. Negative thermal expansion ..... 19
1. 4. Compressibility of materials ..... 22
1.4.1. Negative compressibility ..... 23
1. 5. Intramolecular interactions and their frequencies ..... 26
1. 6. Soft modes and phase transitions ..... 27
1. 7. Overview of experimental and theoretical methods ..... 28
1.7.1 X-ray diffraction ..... 28
1.7.1.1. Powder X-ray diffraction technique ..... 29
1. 7. 1. 2. Rietveld refinement ..... 31
1. 7. 1. 3. High pressure measurement and diamond anvil cell ..... 32
1. 7. 2. Thermal methods ..... 33
1. 7. 3. Micro Raman spectroscopy ..... 34
1. 7. 4. Density functional theory ..... 35
1. 7. 5 Elastic anisotropy of crystals and sound waves in materials ..... 36
2. EXPERIMENTAL ..... 37
2. 1. Materials ..... 37
2. 1. 1. *N*'-2-propylidene-4-hydroxybenzohydrazide ..... 37
2. 1. 2. 4-hydroxybenzohydrazide ..... 37
2. 1. 3. Oxitropium bromide ..... 37
2. 1. 4. Scopolamine bromide hydrate ..... 37
2. 1. 5. Scopolamine bromide ..... 37
2. 2. Methods ..... 37
2. 2. 1. Thermal methods ..... 37
2. 2. 1. 1. Hot-stage microscopy ..... 37
2. 2. 1. 2. Thermal analysis ..... 38
2. 2. 2. Ambiental and *in-situ* high-temperature X-ray powder diffraction ..... 38
2. 2. 3. *In-situ* high-temperature X-ray single crystal diffraction ..... 39
2. 2. 4. *In-situ* high-pressure X-ray single crystal diffraction ..... 40
2. 2. 5. *In-situ* high-temperature Raman spectroscopy ..... 41
2. 2. 6. Density functional calculations ..... 42
3. RESULTS AND DISCUSSION ..... 43
3. 1. *N*'-2-propylidene-4-hydroxybenzohydrazide ..... 43
3.1.1. Thermosalient effect in *N*'-2-propylidene-4-hydroxybenzohydrazide ..... 43
3. 1. 2. Derivatives of *N*'-2-propylidene-4-hydroxybenzohydrazide ..... 56
3. 1. 2. 1. The case of 4-hydroxybenzohydrazide ..... 56
3. 1. 2. 2. Recrystallization of *N*'-2-propylidene-4-hydroxybenzohydrazide ..... 59
3. 2. Oxitropium bromide ..... 60
3. 2. 1. Thermosalinet effect in oxitropium bromide ..... 60
3. 2. 2. Derivatives of oxitropium bomide ..... 74
3. 2. 2. 1. The case of scopalamine bromide hydrate ..... 74
3. 2. 2. 2. The case of scopolamine bromide ..... 83
4. CONCLUSION ..... 95
5. REFERENCES ..... 98
6. LIST OF FIGURES ..... 104
7. LIST OF TABLES ..... 107
8. CV TEODORO KLASER ..... 108

# 1. STATE OF THE ART

## 1. 1. Introduction

The thermosalient crystals are adaptive crystalline solids that are thought of as candidates for active actuating elements in all-organic micromachines. The term *"thermosalient effect"* was first used in 1983 by Etter and Siedle while observing the jumping of crystals of (phenylazophenyl)palladium hexafluoroacetylacetonate. [1] Crystals, of course, respond, in various ways, when exposed to changes in temperature, pressure, chemical surroundings or light. When subjected to thermal treatment, one expects that crystals undergo chemical reactions, such as oxidation, thermal decomposition, or experience some physical changes such as phase transitions, sublimations or melting, but it is extremely exotic when crystals, due to the thermal energy, start to – jump. There have been occasional reports of crystals that jump in the course of these thermal phase transitions – the thermosalient effect – in organic crystals [2] [3] [4] and inorganic crystals. [5] The hopping or jumping of the crystal, visible on a macro scale, is usually associated with a thermally induced polymorphic phase transition from low- to high- temperature form. Materials that provide mechanical response to the temperature change are called thermosalient materials, more colloquially known as *"jumping crystals"*. [6] Apart from being visually attractive and, in general, very fun, this effect is particularly important form both scientific and technological point of view since these materials represent media for the conversion of heat energy to mechanical work. Often, even though the structures of low- to high- temperature form are known, the macrostructural manifestations that accompany of those phase transition remains a considerable mystery. Most thermosalient phase transitions are topotactic, as well as isosymmetric. The crystal structures of two polymorphs (before and after phase transition) are highly superimposable. Slightly different packing and some movements of molecular moieties lead to dramatic changes in the unit cell parameters (10% or more).

Thermosalient materials are among the fastest switching materials reported to date due to a concerted structural change associated with a martensitic phase transition that occurs $10^4$–$10^5$ times faster than other, noncooperative transitions in the same or other materials. For example, the rate of progression of the habit plane during the thermosalient transition (approximated by linear growth and averaged over three crystals) in (phenylazophenyl)palladium hexafluoroacetylacetonate was 0.54 m $s^{-1}$, which corresponds to

a turnover number of $1.272 \times 10^9$ molecules per second. This propagation rate is four orders of magnitude faster than that of the second, non-thermosalient transition in this material where the habit plane moves at $4.34 \times 10^{-5}$ m $s^{-1}$ and $1.026 \times 10^5$ molecules are converted per second. This rate also supersedes greatly the common spin-crossover (low spin–high spin) transitions, which occur on a time scale of $10^{-5}$ m $s^{-1}$. [7] Together with the analogous phenomena, that is triggered by light or mechanical stimulation (photosalient and mechanosalient effects, respectively), they provide a new addition and irreplaceable tool in the expanding of the current materials engineering toolbox. [8] Of one the most intriguing aspect found in thermosalient materials is related to one unusual property in the solid-state physics - the presence of negative thermal expansion correlated to a negative compressibility with values usually order of magnitude higher compared to typical organic materials and even inorganics solids. In fact, values of negative compressibility coefficients in thermosalient materials are rivalled only by the ones of the molecular frameworks, the class of compounds showing the most pronounced negative linear compressibility behaviour. [9]

In this thesis, a synergetic approach, that combines vast experimental methods and theoretical calculations, will be used and aimed not so much on the thermosalient phase transitions itself yet to process that precede the manifestation of thermosalient effect, in particular, the role of negative thermal expansion in the mechanism of thermosalient effect and its correlation to the negative linear compressibility but also to the importance of low energy phonons that assisting a phase transition. Investigations in this thesis are directed towards two, conditionally speaking, different target groups of thermosalient compounds; first, *on the materials in which the effect is already know and observed* and second, *on the potential thermosalient materials which are chemically/structurally/functionally similar to the materials with established thermosalient effect*. *N*'-propylidene-4-hydroxybenzohydrazide is a material in which thermosalient effect was observed but was not fully resolved. From the overview of the research conducted hitherto it is obvious that two assumptions still need to be confirmed (or rejected): (*i*) existence of negative linear compressibility and (*ii*) role of the low-energy phonons in the thermosalient phase transitions. Since the mechanism behind the thermosalient effect cannot be fully explained based on the experiments reported so far, and most certainly it cannot be predicted, we felt necessary to expand the investigations to the group of the compounds obtained by the selected and careful modification of the compounds in which the existence of the effect was previously confirmed. It is to be expected that the thermosalient effect will be extremely sensitive to the subtle changes in the chemical composition (change of

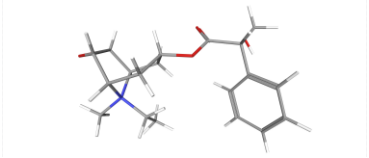
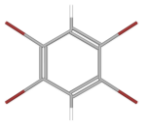
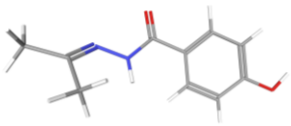
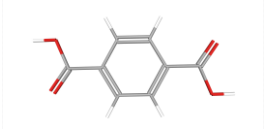
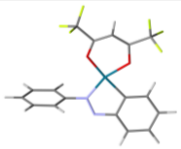
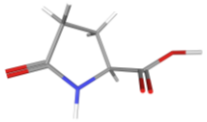
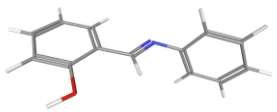
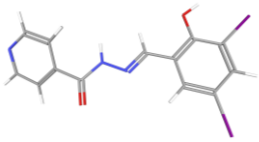
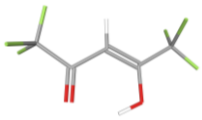
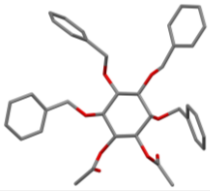
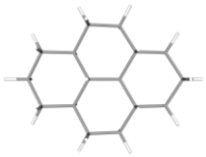
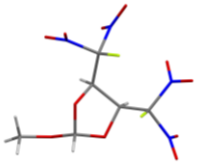
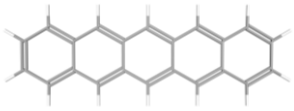
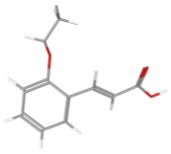
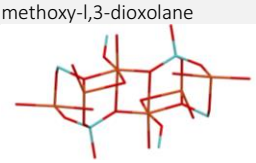
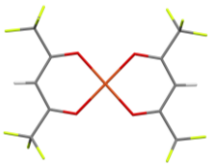
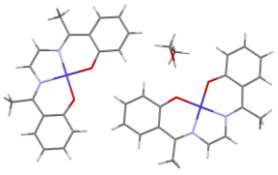
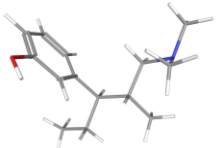
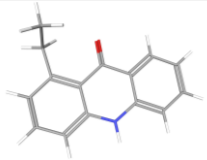
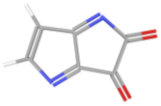
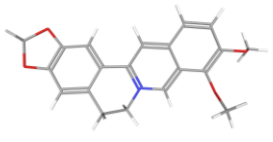
anion, change of the functional group, change of the number of the functional groups, change of the position of functional groups within the aromatic ring) and these investigations of thermosalient derivatives were aimed to pinpointing the specific chemical/structural parameters necessary for the manifestation of thermosalient behaviour. Representative of the second group, the derivative group, that is oxitropium bromide. It is important to stress out that the main aim was not, necessary, to obtain new thermosalient compounds but to gather as many information as possible about the compounds which were obtained by the modification of current thermosalient ones. We felt the no matter if the new compounds exhibit thermosalient behaviour or not, comparison of the information about the original thermosalient materials with the information about their derivatives will in any case help in elucidation of the factors responsible for the existence of the thermosalient effect and provide us with new guidelines for modelling of new thermosalient materials.

At the first sight, investigation of thermosalient materials seem fun, studying this alluring effect, with crystals joyfully jumping around, just as a bag of popcorn. But digging deeper into this fascinating effect one discovers that there is, in fact, a complex background mechanism responsible for the jumping of crystals that requires the utilization of vast number of experimental and theoretical methods on the borderline between physics, chemistry, crystallography, mathematics and material engineering.

# 1. 2. Thermosalient materials

Selected thermosalient materials, studied so far in great details, are shown in Table 1. In further text, an overview of thermosalient effect in those materials will be presented.

Table 1 Examples of thermosalient materials

| | | |
|---|---|---|
|  |  |  |
| Oxitropium Bromide | 1,2,4,5-tetrabromobenzene | *N*'-2-Propylidene-4-hydroxybenzohydrazide |
|  |  |  |
| Terephthalic acid | (phenylazophenyl)palladium hexafluoroacetylacetonate | *L*-Pyroglutamic acid |
|  |  |  |
| *N*-salicylideneaniline | *N*'-(3,5-diiodo-2-hydroxybenzylidene) isonicotinohydrazide | Naphthalene-2,3-diyl-bis(4-fluorobenzoate) |
|  |  |  |
| (±)-3,4-di-O-acetyl-1,2,5,6-tetra-O-benzyl-myo-inositol | *trans,trans,anti,trans,trans*-perhydropyrene | 4,5-bis(fluorodinitromethyl)-2-methoxy-l,3-dioxolane |
|  |  |  |
| Benzo[b]naphthacene | *ortho*-ethoxy-*trans*-cinnamic acid | Copper molybdate |
|  |  |  |
| Cobalt(II) hexafluoro-acetylacetonate hydrate | 2,2'-(ethene-1,2diyl) bis (azaneylylidene) bis(ethan-1-yl-1-ylidene))diphenolate cobalt(II) | Tapentadol hydrochloride |
|  |  |  |
| Ethylacridone | Diketopyrrolopyrrole | Tetrahydrate berberine chloride |

Crystals of 1,2,4,5-tetrabromobenzene jump several centimetres in height during the phase transition from the low-temperature $\beta$-form to the high-temperature $\gamma$-form. [10] Hopping of the crystals occurs at 45.0 °C for single crystals while twinned once jump at 45.5 °C. Layered structures are characteristic for both forms, and the thermosalient effect is influenced by intermolecular Br···Br and C−H···Br interactions. During the phase transition a change in the dihedral angle between the neighbouring rings occurs, flattens the molecular stacks finally generating a strain that in turn causing the crystals to leap when the strain is released. [4] [11] A significant lattice softening was also observed close to the transition point, with the structure becoming more rigid after the phase transition. [12] Among all, only three vibration modes monotonically soften up prior to the phase transition, with complex behaviour exhibited by the remaining lattice modes. Lattice dynamics calculations revealed significant lattice softening at the temperature close to the phase transition from $\beta$ to $\gamma$ phase that is accompanied with increase in the structural strain. [12] The authors propose that, in fact, mentioned anisotropic structural strain is responsible for the large thermosalient effect that is observed, despite a large structural similarity of the low- and high- temperature polymorphs and a small volume change across the phase transition. Investigations by Brillouin light scattering results showed that the thermosalient effect is triggered by elastic instability and that the large intermolecular anharmonic interaction is associated with molecular motions in the (110) plane. [13]

Form II of terephthalic acid transforms into Form III around 90 – 95 °C. During the transition, rhomboid-shaped crystals transform into the rectangular plates and some of the crystals jump during the transition. The transformation is reversible, but temperature hysteresis was noticed during cooling. It has been reported that crystals that did not transform can be triggered by touching them with a sharp metal needle. [14]

Crystals of (phenylazophenyl)palladium hexafluoroacetylacetonate can switch between five crystal structures that are related by four phase transitions including that is accompanied with thermosalient effect. The mechanical effect is driven by a uniaxial negative expansion that is compensated by large positive axial expansion ($260 \cdot 10^{-6}$ $K^{-1}$) that is among the highest values reported in molecular solids so far. The habit plane advances at ~$10^4$ times the rate observed with regular, non-thermosalient phase transitions. Crystals expand by 10% along their longest (crystal) axis at $T$ between 85 and 95 °C, and literally “fly off” the hot stage. Neighbouring stacks of molecules in the low temperature form slip together along [011] suggesting that the thermosalient mechanism could be analogous to the well-known martensitic-type phase transitions. [7] By direct measurement of the actuation force generated by upon reversible α to

γ phase transition, crystals, that are sub-millimeter to millimeter size, exert forces in the range of 1–100 mN upon longitudinal and lateral expansion. This work translates to a volumetric power density of about 1–3 MW $m^{-3}$ and efficiency comparable to the existing multicomponent actuators. [15]

Enantiomerically pure forms of pyroglutamic acid exhibit a particularly interesting thermosalient effect; the crystals jump at least 15 times without any breaking or shattering. The effect happens only when the crystal is not lying on the surface that expands the most. [16]

Upon heating, oxitropium bromide crystals exhibit an endothermic phase transition from form A to form B. The transition from Form A to From B that occurs at 331 K is accompanied by a highly anisotropic expansion by 4% of the cell, in which the *b* axis increases by 11% and the *c* axis decreases by 7%. The phase transition is reversible and shows thermal hysteresis. Both phases are orthorhombic, space group is preserved, differing only significantly in the *b* and *c* cell axes, which is reflected as a difference in the cell volumes of ~ 80 $Å^3$. [17]

Polymorphs of the dichloro derivative of N-salicylideneaniline exhibit mechanical responses such as jumping (Forms I and III) as well as exploding (Form II). [18] The behaviour of jumping exhibited by the polymorphic crystals of Forms I and III is due to the layered sheet morphology and the transmission of thermal stress in a single direction, compared with the corrugated sheet structure of Form II where the heat dissipation is more isotropic causing blasting of crystals. The bromo- and iodo-derivatives did not exhibit any thermal responses. The importance of weak Cl···O interactions on the mechanical response of chloromolecular crystals were also considered. [18] Also, the authors of that paper hypothesize that during heating of Form I and Form III, the heat is transferred uniformly from the face resulting in the transmission of thermal stress largely in a single direction, thereby causing a thermosalient effect. In Form II, however, due to the corrugated wave-like arrangement of molecules, heat transmission is non-uniform resulting in a sudden blast of the crystal.

Importance of theoretical calculations on the investigations of thermosalient effect was first time demonstrated for the *N*'-2-propylidene-4-hydroxy-benzohydrazide. [9] Namely, first-principles electronic structure calculations show that negative thermal expansion, which is present in almost all thermosalient systems known so far, arises from the elastic properties of the crystal which show uniaxial negative compressibility (NLC). Form III exhibits a negative linear compressibility which is an order of magnitude larger than that of any organic compound and, in fact, is comparable with the compressibilities of molecular frameworks that often exhibit pronounced NLC behaviour. Elastic properties seem also to be responsible for the

reversibility of the Form II to Form III transition in contrast to the irreversible Form I to Form II transition. Probably, most important discovery is that low energy spring-like phonons are easily thermally excited and can assist in overcoming the energy barrier between the two phases that must be surmounted for the thermosalient transition to take place, and this might provide an insight into the governing force for the thermosalient effect.

One of the most recently published thermosalient compounds, N'-(3,5-diiodo-2-hydroxybenzylidene) isonicotinohydrazide exists in three polymorphic forms, two RT polymorphs (Forms I and II) and one high-temperature modification (Form III). [19] The transformation for Form I to Form III is reversible and thermosalient and occurs at ~ 55 – 60 °C whereas the transformation from Form II to Form III is irreversible and non-thermosalient. The crystal structures of all three forms are known, but no mechanism for the thermosalient transition is provided, except a very broad generalization that "a probable reason for the thermal response is ascribed to the rapid release of accumulated strain during the phase transition and anisotropy in the structural parameters." [19]

Crystals of Form I of naphthalene-2,3-diyl-bis(4-fluorobenzoate) undergo a reversible phase transition (441 – 443 K) accompanied by thermosalient effect. Form I also undergoes a non-thermosalient reversible phase transition to From III in the temperature range of 160 to 170 K. Comparison of the structures and the mechanical responses of the two polymorphs revealed that the thermosalient effect of Form I was due to reversible closing and opening of the arms of the diester molecules in a tweezer-like action [20].

Another example of thermosalient crystals can be found in the system of three polymorphic forms of inositol (±)-3,4-di-O-acetyl-1,2,5,6-tetra-O-benzyl-myo-inositol. The thermosalient effect is observed during the phase transition from Form II to Form III. Two forms have almost identical packing, with the molecules exhibiting slight offset with respect to each other. Thermosalient behaviour in this case is explained by the cooperative motion of structural constituents. [3]

Crystals of *trans,trans,anti,trans,trans*-perhydropyrene jump about 6 cm high, during the phase transition which occurs at 71.5 °C. The cyclohexane rings in the low-temperature form are in a chair conformation so the perhydropyrene molecules form rough layers parallel to the *ac* plane. Heating causes a slight change in the molecular positions, which generates strain within the lattice. The strain is relaxed during the rapid phase transition, molecular layers slide with respect to each other, and the crystals hop in this process. [21]

Crystals of 4,5-bis(fluorodinitromethyl)-2-methoxy-l,3-dioxolane possess the layered structure with molecules within layers and pairs between layers connected by O···O interactions. Crystals jump off the hot stage, up to 1 cm, at ~ 40 °C. Apart from jumping, the crystals also shatter during the thermosalient transition. [22]

Colourless crystals of the cyclophane "blink" when heated up to 300 °C and jump several times in the range $T$ = 340 – 380 °C. The crystal structure of the high temperature phase is yet unknown, thus impeding any prediction of the thermosalient mechanism in this system. [23]

The thermosalient effect has been noticed during the polymorphic phase transition in pentacene from the low- to high-temperature phase that occurs at ~190 ºC. [24] Determination of crystal structure of the high-temperature phase was not successful since crystals crack and sublime, therefore the mechanism has not been explained in detail.

Thermosalient system with strong hydrogen bonding, ortho-ethoxy-trans-cinnamic acid, was reported. [25] The α-polymorph undergoes a reversible single-crystal-to-single-crystal phase transformation at 60 °C. The new high-temperature polymorph (α') is stable between 60 and 120 °C with three molecules in the asymmetric unit, space group $P$1, and unlike other polymorphs of the same compound, two of the molecules in α' deviate significantly from planarity. Even though the detailed crystal structures of the two forms are given, the explanation for the thermosalient effect is lacking.

A loosely fused azomethine boron complex presenting aggregation-induced emission, crystallization-induced emission enhancement, and thermosalient behaviour accompanying thermochromic luminescence during was recently reported. [26] Boron complex shows large structural relaxation and forms bent structure in the excited state, followed by emission annihilation in the absence of structural restriction. In addition, it was shown that interconversion between these polymorphs could be reversibly induced by heating and cooling. Crystals showed unusual mechanical behaviour, such as hopping and fragmentation by heating and cooling, respectively. It was suggested that the loosely fused structure could be responsible for expressing unique optical and mechanical properties.

$AMoO_4$ compounds (A = Co, Mn, Fe, Ni, Cu, or Zn) exhibit a first-order phase transition associated with piezochromic and thermochromic phenomena. [27] The authors report Birch–Murnaghan model of phase transition, assigning the transition to higher compressibility coefficient, despite the presence of the shorter bonds for the high-temperature form. The cell-volume difference of 13% between the high and low temperature form induces the thermosalient effect associated with a certain crystallite fracture (along the [101] plane).

Two polymorphs of a *N,N′*-dipropylated diketopyrrolopyrrole dye were studied. [28] The yellow polymorph exhibits mechanical response upon transformation to its orange polymorph. No detail on the mechanism itself have been provided.

Recently, it was reported that thermosalient effect occurs in 2,2′-((1*E*,1′*E*)-(((*Z*)-ethene-1,2-diyl) bis(azaneylylidene))bis(ethan-1-yl-1-ylidene))diphenolate cobalt(II) hemisolvate caused by the release of solvent. [29] Two solvents were used to synthetize the solvate complexes, MeOH and EtOH. The black needle-like crystals jump suddenly at ~ 210 and 150 °C, respectively. Single-crystal XRD studies revealed that both complexes possess a stacked assembly of planar molecules in which one of the two crystallographically distinct cobalt molecules are hydrogen-bonded to an alcohol solvent.

Tapentadol, (2R,3R)-3-(3-hydroxyphenyl)-N,N-2-trimethylpentan-1-amine, is a centrally acting analgesic pertaining to the opioid family and was studied, in detail, by the single-crystal X-ray diffraction, differential scanning calorimetry and Raman scattering measurements. [30] The compound undergoes a first-order reversible phase transition at 318 K, as assessed by the coexistence of both phases in the vicinity of the transition and the abrupt change in the unit-cell parameters with temperature. The process is accompanied by thermosalient behaviour. Structural difference are extremely small, with almost no changes in the stronger, non-covalent interaction scheme involving the 'conventional' (N—H···Cl, O—H···Cl) hydrogen bonds.

Ethylacridone and dicyanomethylenated acridones showed crystal-jumping activity upon heating. [31] This is the first example of thermosalient behaviour in a simple aromatic ketone and its derivatives. A systematic investigation of the jumping behaviour of derivatives with different alkyl chains by variable-temperature XRD crystal-structure analyses revealed the mechanism of this phenomenon. Anisotropic dissociation of π stacking in a dimer seems to be responsible for inducing crystal jumping of ethylacridone whereas the collective flipping motion of a dicyanomethylene unit caused the thermosalient effect in the case of dicyanomethylenated acridones.

The crystals of heterospin complexes [*M*(hfac)$_2$L$_2$] (*M* = Cu, Ni, Co, or Mn; hfac = hexafluoroacetylacetonate; and L= nitronyl nitroxide, 4,4,5,5-tetramethyl-2-(1-methyl-1H-imidazol-5-yl)-4,5-dihydro-1H-imidazole-3-oxide-1-oxyl) were found to make unusual jumping motions. [32] Under ambient conditions, the jumping and various displacements of crystals lasted for several weeks. The mechanical motion was accompanied by the cracking

and disintegration of crystals as a result of spontaneous elimination of oxygen, the source of which was the nitronyl nitroxyl fragment of coordinated ligands.

The crystals of tetrahydrate berberine chloride exhibit a variety of instantaneous mechanical responses (cracking, bending, and jumping) on cooling as well as on heating at room temperature. [33] In either direction, the thermo-mechanical responses are manifested by rapid dehydration to a new dehydrated phase with the complete loss of crystal integrity due to the sudden release of an energetically unfavourable arrangement of water molecules.

Despite many thermosalient materials reported to far, the elucidation of the exact mechanism behind the thermosalient effect remains a major challenge, although some (partial) mechanisms have been already advanced in several instances. The research on mechanical effects in single crystals was initiated in 1980s while the increasing number of reports and the growing research groups that work on photoinduced and thermally induced mechanical effects in molecular crystals are posed to revive, and finally provide an explanation for thermosalient effect. As one could see from the brief summary given above, a lot of questions still remain open. One of the striking facts is that it seems there is *"no common denominator",* that there is no specific chemical class of compounds that the thermosalient crystals belong to, no specifics structural feature nor crystallographic class regarding their symmetry proprieties. This aspect of *"having nothing in common"* seems to be most confusing and additionally it aggravates the quest for novel thermosalient materials, beside applying trail-and-error approach. When physicists firstly started to study the matter at subatomic level, a variety and splendour of nature on the full display was discovered, with a dizzying array of particles, forces and fields all whizzing and whirring about, governed by nearly inscrutable laws of physics and rather than creating a chaotic mess (a *"particle zoo"*), all their complicated interactions produce the regular, orderly, patterned macroscopic world that we are familiar with. It seems that the nanoworld of acrobatic crystals, at this point, resembles more to a kind of a "*zoo of molecular crystals"* which have only one very unusual macroscopic effect in common, and still waiting for revelation of its ordered pattern. The deciphering process is often aggravated by an additional problem; during the thermosalient phase transition some crystals break, bend, explode, deteriorate in quality or sublimate, which impedes the crystal structure determination of the high temperature phase thus hinder the possibility to truly understand what has happened. Nevertheless, an attempt to classify thermosalient materials, based on their structural features, has been made and depending on the molecular structure and type of hydrogen bonding network, the molecular crystals could be classified into 3 classes. [34]

**Class 1:** The molecules in this class of thermosalient crystals do not contain strong hydrogen bonding donor and acceptor groups. Crystal packing can be described as a layer of stacked molecules. Typical representative of Class 1 is 1,2,4,5-tetrabromobenzene with two polymorphs showing the more pronounced tilt of benzene rings in the γ Form relative to the β Form as shown in Figure 1.

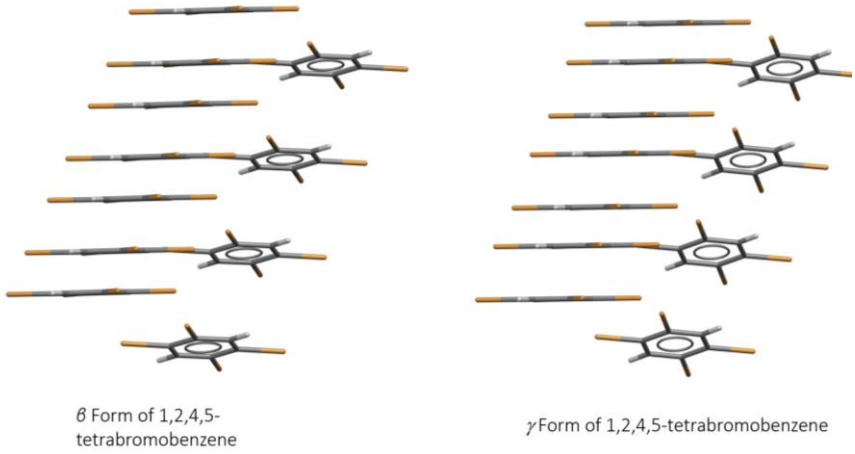



Figure 1 Crystal structures of β Form and γ Form of 1,2,4,5-tetrabromobenzene *[12]*

**Class 2:** In this class of thermosalient molecules, any functional groups that can form strong hydrogen bonds, if present, are sterically hindered thus strong intermolecular interactions are not found in crystal packing of Class 2 of thermosalient compounds. Typical example is (±)-3,4-diO-acetyl-1,2,5,6-tetra-O-benzyl-myo-inositol that have several polymorphs in which the main difference comes from the orientation of the phenyl ether groups (Figure 2)

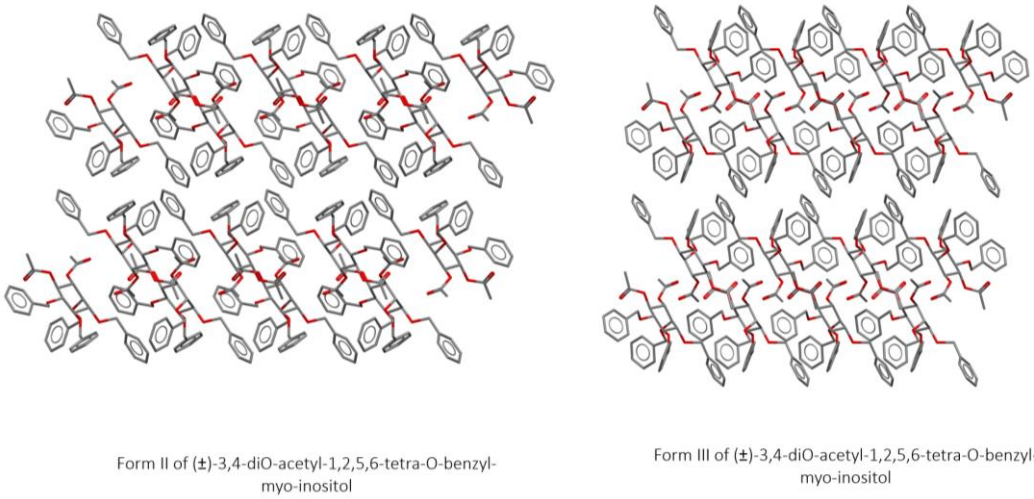



Figure 2 Crystal structure do Form II and form III of (±)-3,4-diO-acetyl-1,2,5,6-tetra-O-benzyl-myo-inositol *[3]*

**Class 3:** The molecules in this class of thermosalient compounds contain functional groups that can form strong intermolecular interactions which often lead to infinite hydrogen bonded tapes or chains. Typical representative is pyroglutamic acid (Figure 3).

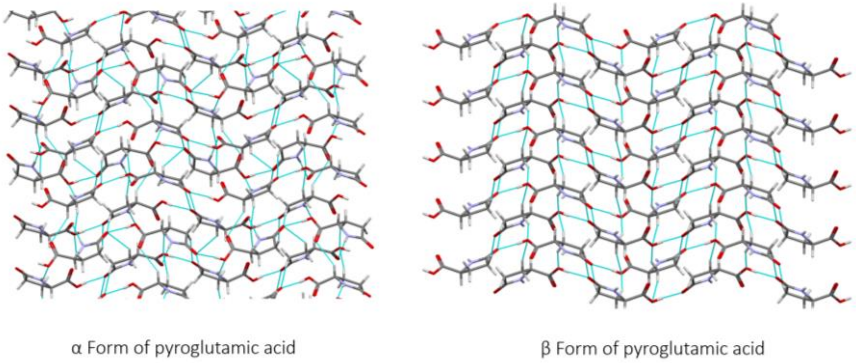



Figure 3 Crystal structure of Form I and Form II of pyroglutamic acid *[16]*

Apart from being visually attractive, thermosalient effect is undoubtedly extremely important from the scientific and technological point of view since these materials represent media for the conversion of (heat) energy to mechanical work. They are prospective candidates for future dynamic active elements, including "smart" medical devices or implants, artificial muscles, biomimetic kinetic devices, electromechanical devices, actuators, materials for electronics and heat-sensitive sensors. [35] [34] [8] [14] Recently, a silver-coated thermosalient crystal was used as a fuse in an electric circuit making this the first application of the thermosalient phenomenon. [36] Silver-coated 1,2,4,5-tetrabromobenzene crystals, a thermosalient compound, are presented as novel electrical fuse materials. These electrically conductive crystals exhibit linear characteristics up to a threshold value where the resistive heating triggers their phase transformation. This causes mechanical motion of the crystals with immediate circuit breakage.

## 1. 3. Thermal expansion of materials

Thermal expansion is the tendency of matter to change its shape, area, and volume in response to a variation of temperature. When a substance is heated, the kinetic energy of its molecules increases. Thus, the vibrations of the molecules increase and usually their average separation becomes larger. To fully understand the mechanism of thermosalient phenomenon it is necessary to understand how thermal treatment influences the crystal structure of thermosalient materials, especially how the strain is generated and accumulated in the crystal lattice. One of the very unique and uncommon properties of the materials which is shared by the vast majority of thermosalient compounds is a negative thermal expansion along at least

one of the principal or crystallographic axes. Therefore, understanding the origin and the effect of this property on the crystal jumping is important.

The relative expansion (also called strain) divided by the change in temperature is called the material's coefficient of thermal expansion and generally varies with temperature. [20] When a material is heated uniformly it undergoes a strain described by the relationship

$$x_{ij} = \alpha_{ij}\Delta T \quad (1)$$

where $\alpha_{ij}$ are the thermal expansion coefficients and $T$ is the change in temperature. Thermal expansion coefficients are often a strong function of temperature. Simple linear relations are insufficient to describe thermal expansion over a wide temperature range. A power series consisting of terms in $\Delta T$, $\Delta T^2$ and higher order terms can be used to describe this thermal expansion over extended temperature ranges. Thermal expansion relates a second rank tensor (strain) to a scalar (temperature change). Strain tensor is symmetric. This means that for the general case (a triclinic crystal), six measurements are required to find the three principal thermal expansion coefficients and the three angles needed to orient the principal axes. Four measurements are needed for monoclinic crystals, three for orthorhombic, two for trigonal, tetragonal, and hexagonal crystals, and only one for cubic crystals. Unlike the dielectric constant, thermal expansion coefficients can be positive, negative, or both positive and negative. [37]

The thermal expansion coefficients can easily be determined from X-ray powder diffraction. The interplanar $d$-spacing are given by Bragg's Law

$$\lambda = 2d \sin\theta \quad (2)$$

where $\theta$ is the Bragg angle and is the wavelength of incoming radiation. Differentiating this equation with respect to temperature gives

$$\frac{\mathrm{d}d}{\mathrm{d}T} = -\frac{\lambda}{2}\frac{\cos\theta}{\sin^2\theta}\frac{\mathrm{d}\Theta}{\mathrm{d}T} \quad (3)$$

from which the thermal expansion coefficient can be obtained:

$$\alpha_d = \frac{1}{d}\frac{\mathrm{d}d}{\mathrm{d}T} = -\cot\Theta\frac{\mathrm{d}\Theta}{\mathrm{d}T} \quad (4)$$

The shifts in Bragg angle, $\mathrm{d}\theta/\mathrm{d}T$, are determined by recording the powder pattern at two different temperatures.

When the atoms vibrate along a line connecting the pair, the asymmetry in the potential causes an increase in the mean distance between the atoms as the temperature increases and indicates correctly that atomic vibrations give rise to thermal expansion only because of anharmonicity. But this crude picture cannot explain negative thermal expansion, because it considers only the

component of relative vibrational motion directed along the line joining the atoms. For example, relative motion perpendicular to this line tends to decrease the distance between the mean positions of the two atoms, and so to contract the solid, non-vibrational contributions (electronic, nuclear etc) to the thermodynamic properties can in addition cause spectacular effects, particularly at low temperatures where vibrational contributions are small.

The relation to the volume dependence of the entropy can be seen by applying standard thermodynamic transformations to the volumetric thermal expansion coefficient $\beta$, defined by:

$$\beta = \frac{1}{V}\left(\frac{\partial V}{\partial T}\right)_P \tag{5}$$

Using thermodynamic Maxwell equation, we obtain:

$$\beta = \frac{1}{V}\left(\frac{\partial V}{\partial T}\right)_P = -\frac{1}{V}\left(\frac{\partial S}{\partial P}\right)_T = \mathrm{k}_T\left(\frac{\partial S}{\partial V}\right)_T \tag{6}$$

where $k_T$ is the isothermal compressibility $-(\partial V/\partial P)_T/V$. The volume compressibility is always positive, and so the change in volume with heating will always be in the direction of increasing entropy; a negative $\beta$ thus indicates that the entropy increases when the substance is compressed isothermally. Entropy (disorder) would normally be expected to increase with volume, and usually $\beta$ is indeed positive. It is only in this limited sense that negative thermal expansion is 'anomalous'. For an ideal classical or quantum gas, $\beta$ is always positive; the origin of negative thermal expansion must therefore lie in the interactions between the particles.

Further insight is obtained by transforming equation (6):

$$\beta = \mathrm{k}_T\left(\frac{\partial P}{\partial T}\right)_V = \left(\frac{\partial P}{\partial T}\right)_V\left(\frac{-\partial \ln V}{\partial P}\right)_T \tag{7}$$

which expresses thermal expansion as the elastic response to thermally induced stress. Equation (7) shows that we can look at the thermal expansion as occurring in two stages: first, a change in pressure, as the temperature is increased at constant volume; after that, a change in volume, as the material is allowed to relax to the original pressure at the higher temperature. As $T \rightarrow 0$ the compressibility approaches a finite limit, and so at low temperatures the temperature dependence of $\beta$ is like that of the thermal pressure coefficient $(\partial P/\partial T)_V$ that may in turn be expressed as the product of two factors: the heat capacity per unit volume, $C_V/V$, which determines how much energy the material gains during a given temperature increase, and the thermodynamic Grüneisen function, $\gamma$, which determines the effectiveness of that energy in changing the pressure:

$$\left(\frac{\partial P}{\partial T}\right)_V = \left(\frac{C_V}{V}\right)\gamma \tag{8}$$

Grüneisen publication of the ideas that led to the thermodynamic parameter named with his name was at the beginning of the 20th century. [38]

The Grüneisen function thus encapsulates the information given by measurements of thermal expansion not already given by the heat capacity and compressibility. Its sign determines whether the expansion is positive or negative, $\gamma$ is dimensionless, and for many simple materials varies little over a wide range about room temperature.

$$\beta = k_T \left(\frac{\partial P}{\partial T}\right)_V = k_T \left(\frac{C_V}{V}\right)\gamma \tag{9}$$

Usually, thermal expansion measurements on solids are related to linear expansion coefficients $\alpha$. For isotropic or cubic symmetry, the linear expansion is independent of direction, and the coefficients of volumetric and linear expansion are simply related by $\beta = 3\alpha$. For lower symmetry, the linear expansion varies with direction, requiring a more general treatment.

The volumetric expansion coefficient $\beta$ can of course be negative in non-cubic as well as in cubic materials. Even when $\beta$ is positive, one or two of the three principal linear coefficients may be negative. The variety of behaviour is thus even richer than for cubic materials; but underlying mechanisms are similar. To describe changes of shape as well as volume, we need to specify at least two independent parameters, called strains, with their thermodynamically conjugate stresses. In any noncubic material, changing the temperature at fixed strain causes anisotropic thermal stress; the resulting expansion is then determined by the elasticity of the material, which also is anisotropic. A general analysis, applicable to materials of any symmetry under arbitrary stress, is well established. [39] [40] Here we give a simpler analysis dealing only with materials of orthorhombic or higher symmetry, expanding at zero pressure. We look at the orthorhombic crystal where there are three independent dimensions $a$, $b$, $c$ along the three principal axes. Strain coordinates $\eta_\lambda$ could be defined such that

$$\mathrm{d}\eta_1 = d\ln a\,, \quad \mathrm{d}\eta_2 = d\ln b\,, \quad \mathrm{d}\eta_3 = d\ln c \tag{10}$$

The expansion coefficients $\alpha_\lambda = (\partial\eta_\lambda/\partial T)_P$ are

$$\begin{aligned} \alpha_1 = \alpha_a &= (\partial \ln a / \partial T)_P \\ \alpha_2 = \alpha_b &= (\partial \ln b / \partial T)_P \\ \alpha_3 = \alpha_c &= (\partial \ln c / \partial T)_P \end{aligned} \tag{11}$$

The three independent stresses $\sigma_\lambda$ related to the strains are defined by

$$\sigma_\lambda = (1/V)(\partial F / \partial \eta_\lambda)_{\eta',T} \tag{12}$$

where the subscript $\eta'$ denotes that all other strains are kept constant. The $\sigma_\lambda$ have the dimensions of pressure, but are *tensile* stresses; for example, under isotropic pressure $\sigma_1 = \sigma_2 = \sigma_3 = -P$. Thermal stress coefficients are related to dimensionless Grüneisen parameters $\gamma_\lambda$:

$$\left(\frac{\partial\sigma_\lambda}{\partial T}\right)_\eta = -\frac{C_\eta}{V}\gamma_\lambda, \quad \gamma_\lambda = -\left(\frac{\partial\sigma_\lambda}{\partial(U/V)}\right)_\eta \tag{13}$$

where $C_\eta$ is the heat capacity at constant strain; the negative signs arises because $\sigma_\lambda$ refers to tensile stress. The Grüneisen parameters may be written as either $\gamma_1$, $\gamma_2$, $\gamma_3$ or $\gamma_a$, $\gamma_b$, $\gamma_c$. As Munn[74] has emphasized, the elastic response to the thermally generated stress is more complex for anisotropic than for isotropic solids; in particular, the signs of $\alpha_\lambda$ and $\gamma_\lambda$ are not necessarily the same, because a stress applied in one direction affects the dimensions in all three directions. Elastic response to stress is described by a matrix of isothermal or adiabatic compliances, $s^T{}_{\lambda\mu}$ or $s^S{}_{\lambda\mu}$, which together form a generalization of the compressibility:

$$s^T_{\lambda\mu} = \left(\frac{\partial\eta_\lambda}{\partial\sigma_\mu}\right)_{\sigma',T}, \quad s^S_{\lambda\mu} = \left(\frac{\partial\eta_\lambda}{\partial\sigma_\mu}\right)_{\sigma',S} \tag{14}$$

Expansion coefficients are then given by analogues of equation (11):

$$\begin{aligned}
\alpha_1 &= \frac{C_\eta}{V}(s^T_{11}\gamma_1 + s^T_{12}\gamma_2 + s^T_{13}\gamma_3) \\
\alpha_2 &= \frac{C_\eta}{V}(s^T_{21}\gamma_1 + s^T_{22}\gamma_2 + s^T_{23}\gamma_3) \\
\alpha_1 &= \frac{C_\eta}{V}(s^T_{31}\gamma_1 + s^T_{32}\gamma_2 + s^T_{33}\gamma_3)
\end{aligned} \tag{15}$$

While the direct compliances $s_{11}$, $s_{22}$ and $s_{33}$ are always positive, the cross-compliances $s_{12}$, $s_{23}$ and $s_{13}$ are usually negative, and so applying a tension in one direction causes extension in that direction but contraction in the other directions. Negative thermal expansion can therefore sometimes occur even when all the $\gamma_\lambda$ are positive. From this, a connection between the thermal and elastic proprieties of a solid system is established and we understand how a material responds to external heating and hydrostatic pressure. Thermal and elastic proprieties are connected through the dimensionless Grüneisen parameter so by inspecting it we could assume how crystal responds to non-ambiental conditions.

### 1.3.1. Grüneisen parameter and thermodynamic proprieties

The Grüneisen parameter, $\gamma$, which connects expansion coefficient, bulk modulus, density and specific heat, can also be written in terms of elastic moduli and their pressure derivatives, providing a quantitative link between thermal and mechanical parameters. Useful relationships include the adiabatic variation of temperature with density, $(\partial \ln T/\partial \ln \rho)S = \gamma$, an interestingly close analogue of the ideal gas equation.

Starting with the quantum harmonic oscillator of Einstein's theory as a mode of crystal vibration, Grüneisen showed that the volume dependence of mode frequency corresponded to

a dimensionless parameter, denoted by $\gamma$, that is a simple combination of familiar thermal and mechanical properties

$$\gamma = \alpha K_T / \rho C_V \quad (16)$$

where $\alpha$ is volume expansion coefficient, $K_T = -(\partial P/\partial \ln V)_T$ is isothermal bulk modulus, $\rho$ is density and $C_V$ is specific heat at constant volume. The adiabatic bulk modulus, $K_S = -(\partial P/\partial \ln V)_S$, and specific heat at constant pressure, $C_P$, may be substituted by the relationship

$$K_S/K_T = C_P/C_V = 1 + \gamma\alpha T \quad (17)$$

The physical meaning of $\gamma$ can be seen as the ratio of the numerator and denominator in equation (17), each of which has a simple thermodynamic meaning. The numerator is obtained as a familiar derivative

$$(\partial P/\partial T)_V = \alpha K_T \quad (18)$$

that is the increase in pressure with the temperature of a material held at constant volume (the pressure required to prevent thermal expansion). The denominator, $\rho C_V$, is the variation of thermal energy with temperature per unit volume. The combination, $\gamma$, is therefore the variation of pressure with thermal energy (per unit volume) of a material held at constant volume. In this context pressure is referred to as thermal pressure, the excess over the pressure of the same material at the same volume but at 0 K (or some other reference temperature).

Equation (16) is a consequence of Grüneisen theory and not a definition of Grüneisen parameter, but usually it is regarded as a definition for thermodynamic purposes and is referred to as the thermal or thermodynamic $\gamma$. Grüneisen lattice mode definition is useful as it connects macroscopic proprieties with crystal lattice proprieties. The Debye frequency, $\nu_D$ , the upper limit of lattice frequencies in the Debye theory of specific heat, is logically regarded as representative for this purpose. Since $\nu_D$ is proportional to the characteristic Debye temperature $\theta_D$, their logarithmic derivatives are the same. Thus, a Debye version of $\gamma$, identified by $\gamma_D$ (a derivative of $\theta_D$) is sometimes regarded as an effective definition of $\gamma$.

A significance of the lattice mode definition is that thermal and elastic properties are controlled by the same interatomic forces and the Grüneisen parameter makes a theoretical connection. It is central to the thermodynamics of condensed matter and, apart from applications in geophysics and high-pressure studies, it could be a useful tool to understand fundamental mechanisms and proprieties of the thermosalient systems.

From the Einstein theory the thermal energy of a single mode of crystal oscillation with a natural frequency $\nu$ (which is function of $V$, but independent of $T$) is:

$$\bar{E} = \frac{\mathrm{h}\nu}{[\exp(\mathrm{h}\nu/\mathrm{k}T) - 1]} \tag{19}$$

And the dependence of specific heat on temperature in the Einstein model is:

$$C_V = (\mathrm{d}\bar{E})/\mathrm{d}T)_V = k(h\nu/kT)^2 \frac{\exp(h\nu/kT)}{[\exp(h\nu/kT) - 1]^2} \tag{20}$$

The last two equations represent Einstein's theory of specific heat, which explained the observed strong temperature dependences of $C_V$ for solids.

Since the same conclusions apply to any assumed frequency, they also apply to more realistic situations with a wide range of frequencies, including Debye model. But Einstein model is a useful starting point for understanding several peculiarities of Grüneisen's theory.

An individual crystal mode of frequency $\nu_i$ has its own value of the parameter

$$\gamma_i = -(\partial \ln \nu_i / \partial \ln V)_T \tag{21}$$

It is not, in general, identical to the $\gamma_i$ of other modes but, as shown here, an appropriate average of all the $\gamma_i$ is equivalent to the dimensionless combination of thermodynamic parameters. By differentiating the thermal energy of a single mode, we obtain:

$$\begin{aligned}(\partial E_i/\partial V)_T &= \left(\frac{\partial \ln \nu_i}{\partial \ln V}\right)_T \left[\frac{1}{V}\frac{h\nu_i}{\exp(h\nu_i/kT) - 1} - \frac{kT}{V}\frac{(h\nu_i/kT)^2 \exp(h\nu_i/kT)}{[\exp(h\nu_i/kT) - 1]^2}\right] \\ &= \left(\frac{\partial \ln \nu_i}{\partial \ln V}\right)_T \left[\frac{E_i}{V} - \frac{T}{V}\left(\frac{\partial E_i}{\partial T}\right)_V\right] \\ &= -\left(\frac{\partial \ln \nu_i}{\partial \ln V}\right)_T \frac{T^2}{V}\left[\frac{\partial}{\partial T}\left(\frac{E_i}{T}\right)\right]_V\end{aligned} \tag{22}$$

Since $E_i$ is the internal energy attributed to mode *i,* it is possible to make use of a general thermodynamic identity for internal energy, $U$, using the relations $(\partial U/\partial V)_T = \alpha K_T T - P$ and $(\partial P/\partial T)_V = \alpha K_T$. In equating this expression with $(\partial Ei / \partial V)_T$ just the effect of exciting mode *i* has to be considered so the subscript *i* is introduced to the pressure in the last equation as well, because it is the thermal pressure of the excitation. From this follows

$$[\partial(Pi/T)/\partial T]V = - (\partial \ln \nu i/ \partial \ln V)T\ (1/V)\ [\partial(Ei/T)/\partial T]V \tag{23}$$

As already mentioned, at constant $V$, $\nu_i$ is independent of $T$, as assumed in the Einstein theory (in this way we are not considering the effect of anharmonicity), and we can take the ratio of the two temperature derivatives

$$[\partial P_i/\partial(E_i/V)]V = -(\partial ln\nu_i/\partial lnV)T = \gamma_i \tag{24}$$

Thus, the ratio of the thermal pressure caused by excitation of mode *i* and the excitation (thermal) energy per unit volume is equal to the mode $\gamma$ by Grüneisen's definition. It matches the interpretation of the thermodynamic definition of $\gamma$. The elastic moduli of bulk material do

not represent well the moduli controlling the thermal motions of atoms in a solid, which are dominated by frequencies of THz order and wavelengths comparable to the atomic spacing. The lattice discreteness means that wave speeds are not similar to those of waves in a continuum, as observed on a macroscopic scale. However, they are controlled by the same atomic forces and, in applying equation (17), we are interested in relative changes, not absolute changes. The relative changes in the modulus for a lattice mode are the same as the relative changes in interatomic forces controlling both it and the corresponding modulus for bulk material. Thus, variations of conventionally observed moduli with density or pressure are direct indicators of the variations of high frequency thermal vibrations and the Grüneisen parameters, $\gamma_i$. Therefore, the Grüneisen parameter provides a quantitative link between thermal and elastic properties. There are two alternative approaches to the calculation of $\gamma$, both ultimately relying on elastic moduli. For real materials, having numerous lattice modes with a wide range of frequencies, their contributions to the total $\gamma$ are added according to their contributions to thermal energy, that is $C_v \gamma = \sum C_i \gamma_i$. At the high temperatures, at which all modes are fully excited, they contribute equally to $\gamma$, which is a simple average for all modes, but at lower temperatures the high frequency modes become inactive and $\gamma$ increasingly reflects the $\gamma_i$ of low frequency modes. However, despite this the temperature variation of $\gamma$ is normally very small. One reason is that, for low frequency modes of the same type, differing only in wavelength and controlled by the same elastic constants, the volume dependences of the $\nu_i$ are all in proportion and give the same $\gamma_i$. The dispersion of high frequencies by lattice discreteness has no effect on $\gamma$, which is defined as the logarithmic derivative of frequency, and therefore depends on relative variations, which are the same as the relative variations in bond forces. This allows use of the familiar elastic moduli obtained from bond forces with the assumption that a solid is a continuum.

### 1.3.2. Negative thermal expansion

Not all substances expand on heating. Probably the most familiar example of negative thermal expansion from everyday life is the increase in density of liquid water between 0 and 4°C, which is crucial for the preservation of aquatic life during very cold weather. Negative thermal expansion has been studied, both experimentally and theoretically, for decades and can be found in a wide range of solid materials such as Si and Ge, various other tetrahedrally bonded compounds, $\beta$-quartz and some ceramics. In addition, more recently, many organic and metal-organic materials are shown to display this property; the research of negative thermal expansion nowadays relives its glorious days owing to the progress in molecular materials

engineering. Indeed, organic ligands having various coordination modes towards the metal centres, as well as the ability to form versatile intermolecular interactions certainly represents an excellent tailoring tool for the formation of networks having different nuclearity, connectivity and dimensionality, making them ideal platforms for thermal expansion modification.[21] [22] [41] The NTE behaviour in molecular materials usually concerns many factors, including transverse vibration modes, geometric flexibility, host-guest interaction, spin states, molecular packing arrangements, and molecular configurations [41] as shown in the Figure 4. The origin of negative thermal expansion in the solid-state matter is not fully understood and this field emerged, once again, as a hot topic of research during last years.

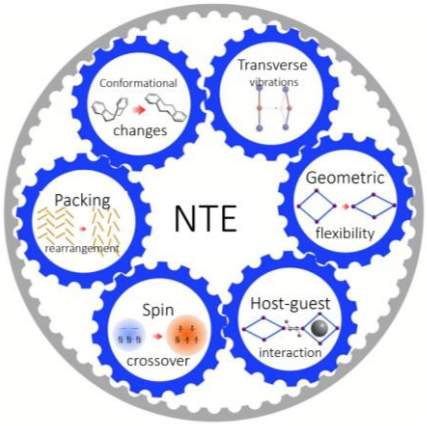



**Figure 4** Principal mechanisms leading to negative thermal expansion in molecular materials [41]

The mechanism of transverse vibration behind the negative thermal expansion has been identified in a lot of single atom bridged materials such as $ZrW_2O_8$ and $ScF_3$ which share a basic structural similarity in which the metal ions bond strongly with bridging atoms forming a network of corner shared polyhedrons as shown in Figure 5. [42] The framework structure can be described or simplified as a 2D perovskite type periodic network.

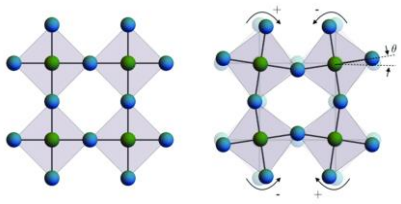


**Figure 5** Negative thermal expansion in materials with 2D perovskite topology [42]

Upon heating, the central bridging atom in the chain M1-O(F)-M2 will vibrate perpendicular to the chain, leading to the shrinkage of the distance between M1···M2 and the material exhibits negative behaviour on the macroscale.

Geometric flexibility is the most outstanding characteristic of molecular materials, and often is the main reason that enable materials to exhibit negative thermal expansion. Figure 6. shows the helical structure of $Cd(eim)_2$ (eim = 2-ethylimidazole) that makes it behave like a spring.[43] Upon heating, the material will shrink along the helical axis, like the spring being compressed, and expand in the perpendicular plane.

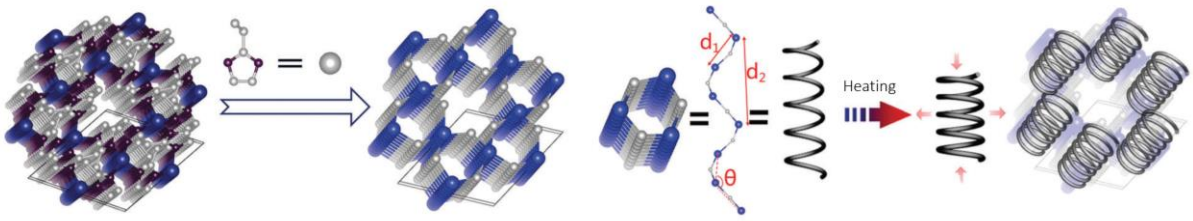



**Figure 6** Spring-like motion causing large anisotropic thermal expansion in nonporous $M(eim)_2$ (M = Zn, Cd) [43]

Another an important class that exhibits negative thermal expansion belongs to the complex systems constructed by two or more molecules or ions that are held together through noncovalent interactions known as "host-guest" compounds. Well known example of host-guest compounds $MPt(CN)_6$ (M=Zn, Cd).[44] The pore size of the two materials is different (45 $Å^3$ and 65 $Å^3$ for Zn and Cd respectively) and individual water molecules usually occupy a volume of 40 $Å^3$. As a result, the existence of water molecules play as a steric hindrance and the coefficient of thermal expansion of $ZnPt(CN)_6$ can be tuned from negative to positive. Similar effect was found for $GaFe(CN)_6$ where thermal expansion can be tailored *via* guest ions and molecules as shown in Figure 7.

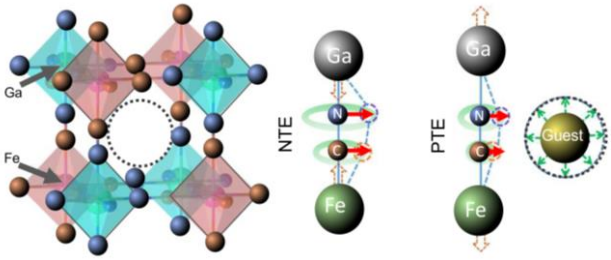



**Figure 7** Cubic structure of $GaFe(CN)_6$ [45]

Finally, many pure organic molecular crystals belong to "soft" materials, which are built from individual molecules and held together by supramolecular interactions including van der Waals forces, π…π interactions, halogen-halogen interactions, as well as hydrogen bonds. Such relatively weak bonded networks are particularly sensitive to temperature changes compared to covalent materials and often exhibit larger coefficients of thermal expansion as well as negative thermal expansion.

## 1. 4. Compressibility of materials

All solids change shape under mechanical force. Under small stresses, the strain $\varepsilon$ is related to stress $\sigma$ by Hooke's Law $(\varepsilon) = (s)(\sigma)$, or the converse relationship $(\sigma) = (c)(\varepsilon)$. The elastic compliance coefficients $(s)$ are generally reported in units of $m^2/N$, and the stiffness coefficients $(c)$ in $N/m^2$. The linear compressibility of a material, $k_L$, is defined as the unit change in length along a given axis as a consequence of a change in hydrostatic pressure, $\Delta P$. Similarly, $k_A$ and $k_V$, the area and volume compressibilities respectively, denote the change in area across a given plane and the change in volume as a result of a change in hydrostatic pressure [46]. These constants are defined symbolically as,

$$\begin{aligned} \frac{\Delta L}{L_0} &= \mathrm{k}_L \Delta P \\ \frac{\Delta A}{A_0} &= k_A \Delta P \\ \frac{\Delta V}{V_0} &= \mathrm{k}_V \Delta P \end{aligned} \tag{25}$$

where $L_0$, $A_0$ and $V_0$ represent the initial length, area and volume respectively, $\Delta L$, $\Delta A$ and $\Delta V$ represent the change in length, area and volume respectively and $\Delta P$ denotes the change in hydrostatic pressure. Nye describes the compressibility as a second rank tensor

$$K = \frac{\partial}{\partial P}\begin{bmatrix} \varepsilon_{11} & \varepsilon_{12} & \varepsilon_{12} \\ \varepsilon_{21} & \varepsilon_{22} & \varepsilon_{23} \\ \varepsilon_{31} & \varepsilon_{32} & \varepsilon_{33} \end{bmatrix} \tag{26}$$

where, $\varepsilon_{ij}$, denotes the strain experienced by the face perpendicular to the $i$-axis and in the direction of the $j$-axis. These strains are a function of the partial differential of the hydrostatic pressure $\partial/\partial P$. The three eigenvalues of this matrix represent the three principal compressibilities of the system and can therefore describe the compressibility of the material. Should any one of the principal values be negative, the material described will exhibit negative linear compressibility. The compliance matrix that describes materials in three dimensions, is a $6 \times 6$ array of constants:

$$\begin{bmatrix} S_{11} & \cdots & S_{16} \\ \vdots & \ddots & \vdots \\ S_{16} & \cdots & S_{66} \end{bmatrix} \tag{27}$$

For structures conforming to the lowest symmetry group, triclinic, 21 unique compliances are required to define the behaviour of the material, although only 15 of these are used to define compressibility, as compliances relating to shear do not affect the linear compressibility. For such materials it is necessary to calculate the principal directions of the linear compressibility

as they are not restricted to lying on the axes of the coordinate system used to define the material. The linear compressibility of the material can be calculated in any direction using

$$\begin{aligned} k_L = {} & (S_{11} + S_{12} + S_{13})L_x + (S_{21} + S_{22} + S_{23})L_y \\ & + (S_{31} + S_{32} + S_{33})L_z + (S_{41} + S_{42} + S_{43})L_xL_y \\ & + (S_{51} + S_{52} + S_{53})L_xL_z + (S_{61} + S_{62} + S_{63})L_yL_z \end{aligned} \quad (28)$$

where $L_x$, $L_y$ and $L_z$ are the components of the unit vector aligned to the axis in which linear compressibility is being calculated. The orthorhombic compliance matrix is shown as Equation 29. The number of unique compliances required to describe the elastic behaviour of the unit-cell increases from six, needed for tetragonal, to nine

$$\begin{bmatrix} S_{11} & S_{12} & S_{13} & & & \\ S_{12} & S_{22} & S_{23} & & \cdots & \\ S_{13} & S_{23} & S_{33} & & & \\ & & & S_{44} & & \\ & \cdots & & & S_{55} & \\ & & & & & S_{66} \end{bmatrix} \quad (29)$$

The presence of these additional constants made it possible for the linear compressibility to be different in each of the three principal axes. The equation for linear compressibility in the direction of a unit vector of components, $Lx$, $Ly$, and $Lz$, is

$$k_L = (S_{11} + S_{12} + S_{13})L_x^2 + (S_{22} + S_{21} + S_{23})L_y^2 + (S_{33} + S_{13} + S_{23})L_z^2 \quad (30)$$

This results in the following equations for linear compressibility in the three principal directions:

$$\begin{aligned} k_x &= S_{11} + S_{12} + S_{13} \\ k_y &= S_{22} + S_{12} + S_{23} \\ k_z &= S_{33} + S_{13} + S_{23} \end{aligned} \quad (31)$$

### 1.4.1. Negative compressibility

Crystalline materials will, in general, have different compressibilities in different directions. For example, a layered material will usually be more compressible along the stacking axis than it is along a perpendicular direction. This directional dependence can be relatively complex, especially for crystals with low symmetry. Looking at the equation 26, parameters $\varepsilon_{ij}$ are functions of hydrostatic pressure and represent the pressure-induced strain experienced by axis *j* along axis *i*. The eigenvectors of Eq. 26 describe an orthogonal coordinate system that brings *K* into diagonal form. These vectors are the so-called "principal axes" of compressibility (sometimes labelled $x_1, x_2, x_3$) which can be interpreted as the crystal directions along which hydrostatic compression does not lead to any shear component. The eigenvalues of *K* correspond to the compressibilities along these principal axes and are the unique

descriptors of linear compressibility for any crystalline material. The formal requirement for negative linear compressibility is that at least one of the eigenvalues is negative and reflect the relative rate of change of the lattice parameters with respect to pressure, and negative linear compressibility materials can be identified as those for which at least one lattice parameter increases under hydrostatic pressure. For the systems with orthorhombic symmetry, or higher, there is an equivalence between lattice and principal axis compressibilities but generally this does not hold for systems with monoclinic or triclinic crystal symmetries. According to the microscopic mechanism likely to be responsible for negative linear compressibility, these can be grouped into four classes. [46] First class of compounds are those for which negative linear compressibility arises as a consequence of proper, improper, or *quasi-ferroelastic phase transitions.* The phenomenon can be considered the mechanical equivalent of ferroelectricity or ferromagnetism, where it is the spontaneous strain, rather than polarization or magnetization, that behaves as the ferroic order parameter. Several simple binary inorganic solids with the $TiO_2$ rutile structure exhibit negative linear compressibility. The ferroelastic instability of the rutile structure type corresponds to a progressive distortion towards a defect NiAs structure and involves expansion in the vertical direction as shown in Figure 8.

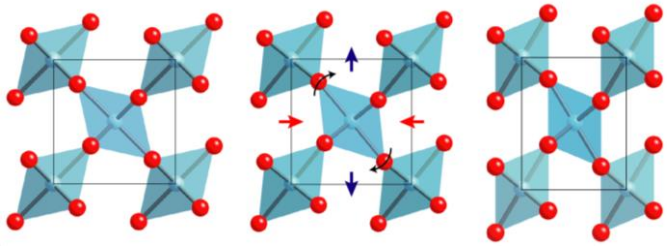


**Figure 8** Ferroelastic NLC mechanism in rutiles [47]

Activation of this tilt system lowers the crystal symmetry from tetragonal to orthorhombic and the lattice is forced to expand along one of the two directions perpendicular to the column axis.

Second class consist of 3D network materials for which the negative linear compressibility is driven by *correlated polyhedral tilts*. The concept that correlated polyhedral tilts might give rise to negative linear compressibility even in the absence of a phase transition is by no means new and is actually more likely to yield practically useful systems since negative linear compressibility is then an intrinsic property of the ambient phase. Because extended structures tend to be less dense than their tilted counterparts, often it will be the case that pressure-driven activation of tilt systems will favour positive linear compressibility rather than negative linear compressibility. Cristobalite-like frameworks are an interesting case of indirect negative linear compressibility materials where negative linear compressibility arises because

a tilt-driven positive linear compressibility mechanism results in a more rapid compression of the crystal lattice than can supported by the bulk material stiffness as shown in Figure 9.

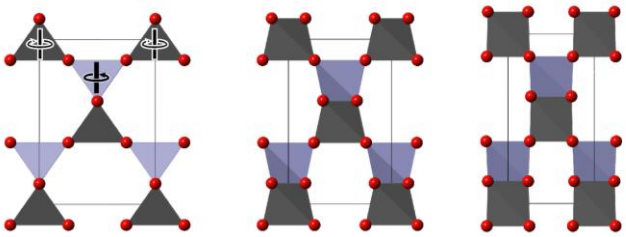


**Figure 9** The β-cristobalite structure of $BEO_4$ (E = P, As) exhibiting subsequent rotation of all tetrahedral units about the tetrad axis. [46]

Third class are *helical systems*. Materials that exhibit negative linear compressibility expand under hydrostatic pressure but also, they contract under negative (*i.e.* internal) pressure. When filled with fluid, the length of helices decreases as the helix cross-section increases. Helical arrays of tendons enable muscle-like contraction and these materials might be exploitable as artificial muscles and actuators if these motifs can be incorporated as part of materials design. On the atomic scale, there are two remarkably simple chemical systems with helical structures, the trigonal polymorphs of elemental selenium and tellurium [48] as shown in Figure 10.

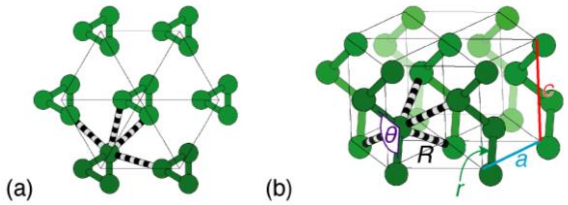



**Figure 10** The crystal structure of selenium and tellurium consists of a triangular array of trigonal helices [48]

Final, forth class of materials exhibiting negative compressibility are the materials possessing a *3D framework based on wine-rack, honeycomb, or related topologies* as shown in Figure 11.[45]

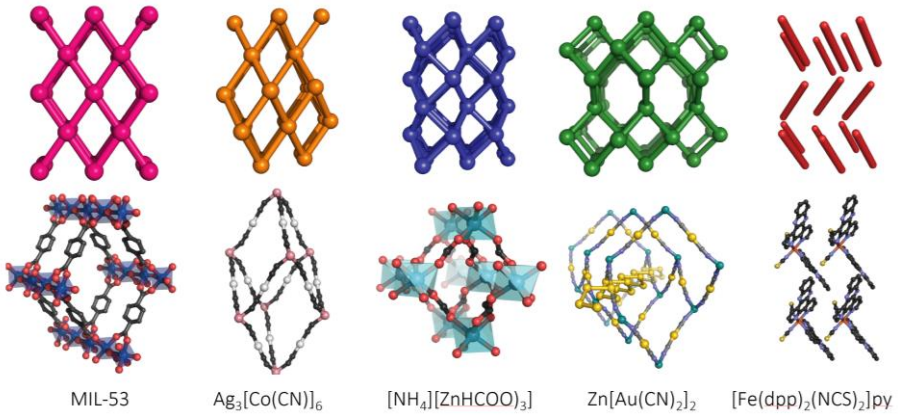



Figure 11 Wine-rack and honeycomb-like topologies known to favor negative linear compressibility and corresponding chemical systems [45]

Those structures are characterized by extreme mechanical anisotropy and both have the property that their volumes are reduced under uniaxial expansion. Typical compounds that belong to this class are molecular frameworks such as ammonium zinc(II) formate, $[NH_4][Zn(HCOO)_3]$ and the zinc alkyl gate (ZAG) family. [45]

## 1. 5. Intramolecular interactions and their frequencies

Terahertz (THz) vibrations in the frequency range of 30–200 $cm^{-1}$ provide direct evidence for the formation of weak bonds in crystals. A fact that weak intermolecular interactions in crystals provide a spectroscopic profile with strongly individual characteristics in the THz region, i.e., the THz method is very sensitive to the weak intermolecular interactions in crystals, enables the unambiguous identification of materials. Its applicability, including for the purposes of pharmaceutical analysis, in identifying biologically active samples has been demonstrated recently. [49] The packing forces in the molecular crystals in the solid state are noncovalent, such as hydrogen bonding and van der Waals interactions. These weak intermolecular forces play a significant role in a great variety of physical, chemical, and biological phenomena. The effects of these forces manifest themselves, e.g., in the behaviour of real gases, in the special properties of water or in the processes of protein folding. Different packing of the same molecules leads to the formation of a new polymorphic crystal structure. Hydrogen bonding is a topic of vital scientific research even though it was discovered more than 100 years ago. The reason for the long-standing interest lies in the eminent importance of hydrogen bonds for the structure, function, and dynamics of a vast number of chemical systems involving mineralogy, materials science, general inorganic and organic chemistry, supramolecular chemistry, biochemistry, molecular medicine, and pharmacy. In the hydrogen

bond denoted by X–H···A, the group, X–H, is called proton donor or electron acceptor, and A is called the proton acceptor or electron donor. The chemical variation of the donor and/or acceptor, and possibly also of the environment, can gradually change the hydrogen bond to another interaction type. The transition to pure van der Waals interactions is very common. The hydrogen bond consists mainly of three interactions: electrostatic, induction and dispersion. The strength of electrostatic interactions depends on the polarity of $X\delta^-–H\delta^+$ or $A\delta$. Induction is the interaction between a permanent dipole and an induced dipole. Dispersion is the interaction between induced dipoles. The polarity of $X\delta^-–H\delta^+$ or $A\delta^-$ (or both) in the array, X–H···A, can be reduced by the suitable variation of X or A. This reduces the electrostatic part of the interaction, whereas the van der Waals component is much less affected.

## 1. 6. Soft modes and phase transitions

The study of phase transitions is at the very core of structural condensed-matter physics and in a large class of phase transitions the system undergoes a symmetry change. Some important aspects of a phase transition are:

- It can be driven by many physical parameters like temperature, pressure, chemical composition, magnetic or electric field etc. If the driving parameter is temperature, the high-temperature phase is almost always more disordered, i.e., has a higher symmetry than the low-temperature phase.
- Phase transitions entail a change in the entropy of the system that could be discontinuous or continuous
- If the phase transition is accompanied by release of heat (latent heat), all the other thermodynamic quantities (internal energy, entropy, enthalpy, volume etc.) are discontinuous as well. Such a phase transition is known as first order transition.
- If phase transition is continuous across the transition temperature (or other transition parameter), the thermodynamic quantities are continuous, but their first derivatives are discontinuous. In particular, the specific heat has a pronounced anomaly (see below) and the thermal expansion coefficient has a step at the transition.
- Some important phase transitions do not entail a change in symmetry, such phase transitions can only be first order.

Large class of phase transitions are displacive, i.e., driven by displacements of atoms or ions. Naturally, the relevant modes will be displacive, i.e., in displacive phase transitions, the modes that drive the transitions are the same phonon modes driving the lattice dynamics. This is not at all an obvious result, as very different timescales are being discussed: phase transitions

typically occur in a matter of seconds, whereas typical phonon frequencies are in the THz range. Nevertheless, this observation cannot be coincidental. Most displacive phase transitions have a dynamical character and are caused by softening of a particular phonon. What this means is that the frequency of a particular phonon starts to decrease as the phase transition is approached (the phonon "softens"), until the frequency reaches zero at the phase transition. At this point, the phonon is "frozen", i.e., it is no longer dynamical. It has, in fact, transformed into a static displacement pattern exactly the mode needed to describe a symmetry lowering through the phase transition. Exactly at the phase transition, the phonons become highly anharmonic at the precise Brillouin zone point, but the crystal remains rather harmonic, and the thermal expansion anomalies are typically small. As the temperature drops below the phase transition, an event must happen to restore the quasi-harmonic character of all lattice vibrations, and this depends on the details of the phase transition.

## 1. 7. Overview of experimental and theoretical methods

### 1.7.1 X-ray diffraction

X-ray diffraction is a non-destructive technique for structural characterization of crystalline materials. It is based on the fact that X-rays are scattered at specific angles from each set of lattice planes in a sample and diffraction maxima are produced by constructive interference of these beams. This method provides information on structures, phases, preferred crystal orientations (texture), and other structural parameters, such as average grain size, crystallinity, strain, and crystal defects. Wavelength of x-rays used in the experiment are in the Ångström range (1 Å = $10^{-10}$ m) which is on the scale with the typical interatomic spacing in the crystal. Electron density can be reconstructed from the diffraction pattern obtained from X-rays scattered on the periodic assembly of molecules or atoms in the crystal. The Braggs provided an interpretation of the diffraction phenomenon by a simpler crystal lattice, substantially based on an approximation of the event as if it were a simple reflection. In the crystal lattice there are several families of planes, each of which may be affected by the "reflection" of the incident waves. However, given the nature of the wave and the characteristics of periodicity of the lattice, reflection it is not always possible, but limited to some special angular relationships between the direction of incidence and the matter plan.

The conditions under which constructive interference is generated are such that sum of the two vectors ***r*** and ***r'*** (difference in incident and diffracted optical path) are equal to an integer number of wavelengths:

$$r + r' = d_{hkl}\sin(\theta) + d_{hkl}\sin(\theta) = n\lambda \quad (32)$$

which allows to derive Bragg's law. By considering a generic plane, the law can be written so to make its generic equivalence:

$$2d_{hkl}\sin(\theta) = n\lambda \quad (33)$$

Note that the waves diffused by the nodes belonging to a plane are necessarily all in phase and therefore always interact constructively since incident and diffracted waves are out of phase with +*r* and -*r* with respect to a lattice point close, and therefore a total of two neighbouring lattices point produce a "phase" wave. An interpretation can be seen in vector terms, remembering the properties of vectors direction of the reciprocal lattice (Figure 12).

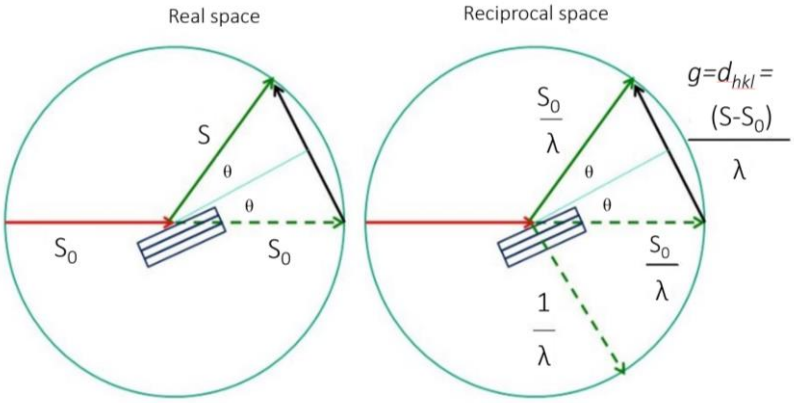



Figure 12 Representation by vectors of Brag's law

The difference vector (*S*-*S*$_0$) between the incident wave (*S*$_0$) and the diffracted one (*S*) is parallel to the vector of the reciprocal lattice *d**$_{hkl}$. If *S* and *S*$_0$ are unit vectors, then | *S*-*S*$_0$ | = 2 sin (*θ*). Using the fact that | *d**$_{hkl}$ | = 1/*d*$_{hkl}$, we obtain:

$$\lambda = 2d_{hkl}\sin(\theta) = |S - S_0|ld^*h_{kkl},$$
$$\lambda d^*_{hkl} = |S - S_0|. \quad (324)$$

From which Bragg's law can be described as:

$$|S - S_0|/\lambda = \mathrm{d}^*_{\mathrm{hkl}} = ha^* + kb^* + l\mathrm{c}^*. \quad (35)$$

Therefore, the conditions *hkl*, for which the Bragg relation is satisfied, also indicate the lattice plane (defined by Miller indexes *hkl*) on which X-rays are diffracting.

### 1.7.1.1. Powder X-ray diffraction technique

Polycrystalline powder consists of many microcrystals (with all possible orientations). In the powder diffraction the diffracted rays enclose cones with the center in the origin the axis in the direction of the incident beam (cones of Debye-Scherrer); this is due to the particular

symmetry of the distribution of microcrystals orientations around the direction of the incident beam. The diffractometer is usually set up in the Bragg-Brentano geometry, in reflection mode thus allowing high intensity of the diffracted beam (Figure 13).

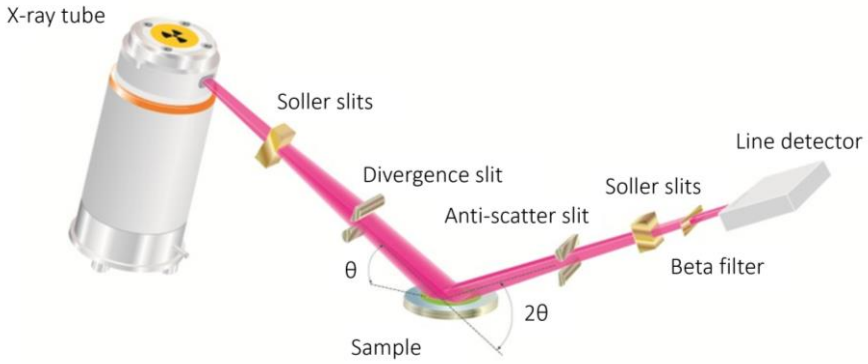



Figure 13 Bragg-Brentano geometry [91]

The incident beam is collimated by a slit to make its path as straight as possible. The crystalline sample is mounted in the holder of X-rays goniometer. The diffracted beams all emerge simultaneously, and a counter mounted on a $2\theta$ circle, similar to that of the single crystal diffractometer, collects them one by one, rotating in the direction of increasing values of $2\theta$ or decreasing. In general, the diffractometer is controlled by a computer which manages the goniometer and controls the acquisition of the data by the detector, also equipped with a rotating arm to acquire diffracted beams at different angles.

Radiation used is in XRD experiments is produced by the characteristic lines of a metallic anode. The wavelengths produced depend on the material used as anode. Some of the wavelengths (Å) most commonly used in XRD experiments are:

| Anode | $K\alpha_1$ (Å) | $K\alpha_2$ (Å) |
|---|---|---|
| Cu | 1.540 | 1.544 |
| Mo | 0.7093 | 0.7135 |
| Ag | 0.5594 | 0.5638 |

The radiation should be monochromatic, using appropriate metal filters. For example, in the case of a molybdenum anode with $Z = 42$, a filter of an element with atomic number Z-1 or Z-2 can be used, possible zirconium with $Z = 40$ to filter the $K\alpha$. Single crystal technique provides very accurate and precisely localized position of the peaks (and therefore of the reciprocal lattice points from which the unit cell of the lattice can be obtained). On the other hand, when polycrystalline sample is measured, the possibility to locate each lattice point gets lost and the „three-dimensional" information of the single crystal is reduced to a one-dimensional function (function of the diffraction angle, $\theta$), making it much more complex to obtaining the information of crystal lattice.

### 1. 7. 1. 2. Rietveld refinement

The Rietveld method uses a least squares approach to refine a theoretical line profile until it matches the measured profile. The method was applied originally by Rietveld to the refinement of neutron intensities recorded at a fixed wavelength and subsequently, it has been used successfully for analysing powder data from neutrons or X-rays experiments. [50] Powder refinements are usually less satisfactory than those on single-crystal data, as the three-dimensional information of the reciprocal lattice is compressed into one dimension in the powder pattern.

The model of the structure is refined by least-squares minimization of the residual:

$$\sum_{i=1}^{N} w_i[y_i(\text{ obs. }) - y_i(\text{ calc. })]^2 \qquad (36)$$

Here, $y_i$(obs.) is the intensity measured at a point $i$ in the diffraction pattern corrected for the background intensity $b_i$, $w_i$ is its weight, and $y_i$(calc.) is the calculated intensity. If the background at each point is assumed to be zero, and if the only source of error in measuring the intensities is that from counting statistics, the weight is given by

$$w_i = [y_i(\text{ obs. })]^{-1} \qquad (37)$$

The sum runs over all $N$ data points. The number of data points can be arbitrarily increased by reducing the interval between adjacent steps. Then the calculated intensity is evaluated using the equation:

$$y_i(\text{ calc. }) = s\sum_{k=k_1}^{k_2} m_k L_k |F_k|^2 G_{ik} \qquad (38)$$

where $s$ is a scale factor, $m_k$ is the multiplicity factor for the kth reflection, $L$ is the Lorentz polarization factor, $F$ is the structure factor and $G_{i,k}$ is the 'peak-shape function'. The summation in is over all nearby reflections, $k_1$ to $k_2$, contributing to a given data point $i$. A fundamental problem of the Rietveld method is the formulation of a suitable peak-shape function. For X-rays, a Pseudo-Voigt function (linear combination of Gaussian and Lorentzian functions) is most used as the tails of a Gaussian distribution fall off too rapidly to account for particle size broadening.

It is given by:

$$G_{ik} = \frac{2\eta}{\pi H_k}\left[1 + 4\left(\frac{\Delta 2\theta_{ik}}{H_k}\right)^2\right]^{-1} + (1-\eta)\frac{2\sqrt{\ln 2}}{\sqrt{\pi}H_k} exp\left[-4\ln 2\left(\frac{\Delta 2\theta_{ik}}{H_k}\right)^2\right] \qquad (39)$$

where $H_k$ is the full width at half maximum (FWHM) of the peak, $\Delta 2\theta_{ik} = 2\theta_i - 2\theta_k$ where $2\theta_i$ is the scattering angle at the ith point, and $\theta_k$ is the Bragg angle for reflection $k$.

The angular dependence of the FWHM for a Gaussian peak- shape function can be written in the form

$$H_k^2 = U \tan^2 \theta_k + V \tan \theta_k + W \quad (40)$$

where $U$, $V$ and $W$ are half width parameters independent of fit. [51] To allow for intrinsic sample broadening and instrumental resolution, $U$, $V$ and $W$ are treated as adjustable variables in the least-squares procedure.

There are two types of parameter used in the least-squares. The first contains the usual structural parameters: for example, fractional coordinates of each atom in the asymmetric unit and the corresponding isotropic or anisotropic displacement parameters. The second type represents 'profile parameters' which are not encountered in a least-squares refinement of single- crystal data. These include the half-width parameters and the dimensions of the unit cell. Further parameters may be added to both groups allowing for the modelling of the background and for the asymmetry of the reflections. The maximum number of parameters that can be safely included in a Rietveld refinement depend on the quality of the diffraction pattern. In the ideal case, with the ideal instrument and the ideal sample (indefinitely large crystals and perfect crystal lattice with no defects) the observed diffraction profile would be the δ-function located at the Bragg angle – as determined by the crystallographic plane spacing. In reality, there are many contributions to the diffraction peak finite width. Profile broadening can be separated into two groups – instrumental broadening and the sample broadening. Instrumental broadening arises from the instrumental imperfections (slit widths, sample size, penetration in the sample, imperfect focusing, unresolved $\alpha_1$ and $\alpha_2$ peaks, wavelength widths of $\alpha_1$ and $\alpha_2$ in cases where the peaks are resolved, etc.). To correct for instrumental broadening, usually a diffraction pattern of a standard is taken. Standard is the sample in which the particle size is large enough to eliminate the broadening due to the small crystallite size and which is deformation-free. The diffraction pattern of standard is taken under the same condition as the sample, so that the broadening of standard is equal to the instrumental broadening. On the other hand, the sample broadening arises from the crystal sample imperfections solely.

#### 1. 7. 1. 3. High pressure measurement and diamond anvil cell

The diamond anvil cell was introduced in the late 1950s and since then it became the most successful method for generating high-pressure conditions providing the opportunity for *in situ* study of matter at pressures above 300 GPa using a wide range of diffraction,

spectroscopic, elastic and inelastic scattering methods. The heart of the device is a pair of polished diamonds (often with (100)-crystal orientation for the highest strength). A metal (Re or steel) gasket with an indentation and a hole is placed between the two opposing diamond anvils forming a sample chamber. The diamonds are mounted on a hard (tungsten carbide, for example) seats and the latter are placed inside a mechanically driven metallic cell as shown in Figure 14. For X-ray powder diffraction many designs are available, there are both commercial and academic research solutions.

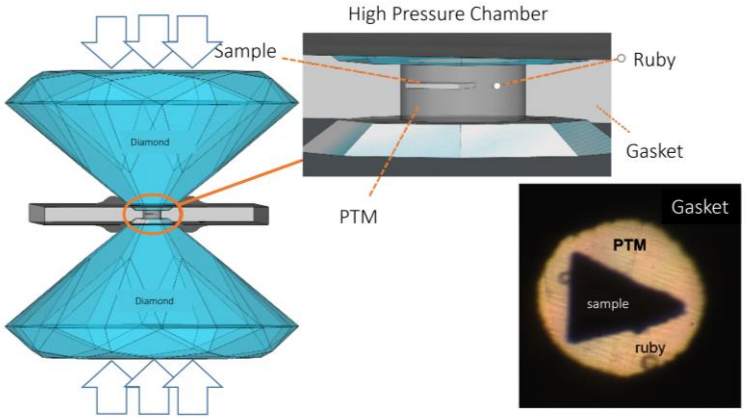



**Figure 14** Diamond anvil cell [52]

## 1. 7. 2. Thermal methods

Thermal techniques, such as differential thermal analysis or differential scanning calorimetry, are based on the calorimetric analysis and used to study the changes in the substance as a function of temperature.[54] Differential scanning calorimetry detects endothermic and exothermic transitions like the determination of transformation temperatures and enthalpy of solids and liquids as a function of temperature. In contrast to classic calorimetry, where a sample is put into an isolated chamber to monitor its heat uptake and release in an isothermal experiment, the differential scanning calorimetry is a dynamic procedure. A typical calorimeter is an isolated chamber where a sample is placed in a surrounding medium. Then the sample is heated with a definite amount of heat. The difference in temperature between sample and surrounding medium gives the heat capacity of the sample and information about heat release and consumption of the sample. Besides that, the differential scanning technique uses a sample and reference that are facing the same conditions and their signal is directly subtracted from each other. This allows the detection of transitions such as melts, glass transitions, phase changes, and curing. Similar technique, differential thermal analysis, is a technique for identifying and quantitatively analysing the chemical composition of substances by observing the thermal behaviour of a sample as it is heated. In differential

thermal analysis, the material under study and an inert reference are made to undergo identical thermal cycles, while recording any temperature difference between sample and reference. The main difference between differential scanning calorimetry and differential thermal analysis is related to the fact that differential scanning calorimetry measures heat flow difference while differential thermal analysis measures temperature differences between a reference sample and a sample of interest.

In thermogravimetric analysis a thermogravimetric analyser continuously measures mass while the temperature of a sample is changed over time. Mass, temperature, and time are considered base measurements in thermogravimetric analysis while many additional measures may be derived from these three base measurements. A typical thermogravimetric analyser consists of a precision balance with a sample pan located inside a furnace with a programmable control temperature. The temperature is generally increased at constant rate (or for some applications the temperature is controlled for a constant mass loss) to incur a thermal reaction. The thermal reaction may occur under a variety of atmospheres including ambient air, vacuum, inert gas, oxidizing/reducing gases, corrosive gases, carburizing gases, vapours of liquids or "self-generated atmosphere" as well as a variety of pressures including: a high vacuum, high pressure, constant pressure, or a controlled pressure. [53]

### 1. 7. 3. Micro Raman spectroscopy

Raman spectroscopy is a non-destructive analysis technique that is used to identify the chemical bonding of different materials and identify their molecular symmetry. Basic principle of Raman spectroscopy lies in illuminating a sample with the monochromatic light of a laser and analysing the spectral shift of the incident light as diffused from the sample. [54] The data obtained by this method originate from light scattering processes that provide information on inter- and intra-molecular vibrations and can be used to further understand chemical reactions. It can also be used to obtain certain vibrations of a molecule (molecular imprint) used to identify a substance, but in addition Raman spectroscopy can be used to obtain additional lower frequency modes and vibrations from which crystal lattice data and thus structure of the molecule. For investigation of small areas, the laser can be passed through an optical microscope, thus reducing the sample area. This technique is generally referred to as micro-Raman. On the incoming path, the laser beam is reflected towards the microscope by the means of special spectral filter, used in injection/rejection mode. On the return path to the spectrograph, the Raman back-scattered light is fully transmitted through the filter towards the

confocal slit-hole located at the entrance of the spectrograph. The spectrograph disperses the panchromatic Raman signal onto the CCD multichannel detector.

### 1. 7. 4. Density functional theory

Usually, a picture of a solid state or molecular system from a theoretician's point of view is an inhomogeneous electron gas [55]. That basically means that we look at the system at as a set of interacting electrons (charged point masses) which move determined by the quantum-mechanical rules in the potential field of static atomic nuclei. This approximation is known as the Born-Oppenheimer approximation. To solve this problem different electron approximations must be used, the most elementary of which are Hartree or Hartree-Fock and which date back to 1920's. In the last 50 years or so, there is another method of choice for tackling such problems – density functional theory (DFT). Density functional theory is one of the most widely used methods for *ab* initio calculations of the structure of atoms, molecules, crystals surfaces and their interactions. DFT has two main advantages compared to Hartree-Fock method, namely it can sufficiently deal with many body problems with high accuracy, and it is computationally relatively simple. DFT is used in the problems of a classical interacting system of point particles, usually electronic systems. Free energy and partition function depend on the potential function rather than on the scalar volume and in this sense free energy is functional. Over the years many different applications of DFT have been developed because knowledge of the electronic ground-state energy as a function of the position of the atomic nuclei determines molecular and crystal structure, and gives forces acting on the atomic nuclei when they are not at their equilibrium positions. Nowadays, DFT is being used routinely to solve problems in the condensed matter physics such as lattice structures [56], phase transitions in solids [57] and liquid metals. [58] Furthermore, DFT made possible development of accurate molecular dynamic solutions in which the forces are evolved quantum mechanically "on the fly". [59] It is important to stress out that DFT becomes extremely important in the problems involving large molecules. [60] The computational power (and consequently time needed for the calculations) needed for the conventional quantum physics/chemistry calculations grows exponentially with the number of electrons involved in the problem, while in DFT it grows roughly as the third power of this number. In practice this means that DFT is able to cope with the problems involving hundreds of atoms, while using conventional quantum calculations one is restricted to only few atoms. Finally, it is important to mention that all practical uses of DFT calculations are based on essentially uncontrolled

approximations and the validity of the method is established its reproducibility of experimental results.

### 1. 7. 5 Elastic anisotropy of crystals and sound waves in materials

Anisotropy and structure–property relationship in materials is related. Tensors and matrices provide the mathematical framework, and symmetry is helpful in determining which coefficients are absent, and which must be equal, but they say nothing about the sizes of the property coefficients. Magnitudes depend more on atomistic arguments. These relationships provide a qualitative understanding of the molecular mechanisms which underlie the choice of materials for various engineering applications. An anisotropy index seeks to quantify how directionally dependent the properties of a system are. Christopher M. Kubea made a study on elastic proprieties of materials on quantifying the elastic anisotropy of crystalline materials. He proposed a new scalar log-Euclidean anisotropy measure $A^L$, which overcomes these deficiencies. It is based on a distance measure in a log-Euclidean space applied to fourth-rank elastic tensors. $A^L$ is an absolute measure of anisotropy where the limiting case of perfect isotropy yields zero. A supplementary material is provided for the analytical expressions for $A^L$ valid for any symmetry (from cubic to triclinic). The supplementary material provides a detailed procedure with a *Matlab* script for calculating the anisotropy for any material assuming the elastic constants are well known. [61] A singular anisotropy index is attractive because of its simplicity when compared to the plurality of anisotropy factors defined for specific planes in crystals. Ranganathan and Ostoja-Starzewski derived a universal anisotropy index $A^U$ to provide a singular measure of anisotropy. This index was termed universal because of its applicability to all crystal symmetries, a short coming of all previous measures. $A^U$ is based on the fractional difference between the upper (Voigt) and lower (Reuss) bounds on the bulk and shear modulus, which introduced the influence of the bulk modulus for the first time.

Solving the Christoffel equation eigenvalue problem by diagonalization; calculating group velocities and enhancement factors analytically as derivatives. [62]

# 2. EXPERIMENTAL

## 2. 1. Materials

### 2. 1. 1. *N*'-2-propylidene-4-hydroxybenzohydrazide

Synthetic preparation of *N*'-2-propylidene-4-hydroxybenzohydrazide was slightly modified from the one reported by Centore et al. [63] The compound has been prepared by refluxing 2.5 g of 4-hydroxybenzohydrazide in 20 mL of acetone for 18 h. Subsequently, half of the solution volume was removed in vacuum and suspension was filtered to obtain 2.3 g of desired product as white crystalline solid. Solid was dried in vacuum oven at 50°C for 2 h.

### 2. 1. 2. 4-hydroxybenzohydrazide

4-hydroxybenzohydrazide was prepared by dissolving 0.5 g *N*'-2-propylidene-4-hydroxybenzohydrazide in 300 ml of distilled water. The mixture was heated up to 60 °C until solute was dissolved. The solution was left to evaporate in a laboratory beaker at room temperature for one week. Obtained crystals were dried in the air.

### 2. 1. 3. Oxitropium bromide

Used as purchased from Sigma Aldrich, CAS Number 30286-75-0, ≥99% (HPLC) in form of powder.

### 2. 1. 4. Scopolamine bromide hydrate

Scopolamine bromide hydrate was recrystallized from0.2 g of scopolamine bromide and 10 ml of distilled water. Distilled water was added to scopolamine bromide the until complete dissolution. The solution was left to evaporate in a laboratory beaker at room temperature for 5 days. Obtained crystals were dried in the air.

### 2. 1. 5. Scopolamine bromide

Used as purchased from Sigma Aldrich, CAS Number 155-41-9, ≥98% (HPLC) in from of powder.

## 2. 2. Methods

### 2. 2. 1. Thermal methods

#### 2. 2. 1. 1. Hot-stage microscopy

*In-situ* macroscopic behaviour of *N*'-2-propylidene-4-hydroxybenzohydrazide, 4-hydroxybenzohydrazide, oxitropium bromide, scopolamine bromide hydrate and scopolamine

bromide during heating and cooling was investigated by polarizing microscope Nikon Aclipse LV150NL equipped with a hot-stage compartment and digital camera Optoteam OPTOCAM II at the Laboratory for microstructure, Department of Physic, Faculty of Science, University of Zagreb, Croatia in the group of Prof. Željko Skoko. The microscope is equipped with a controller (Linkam T95-PE) used to control the temperature profile either manually or by the means of an automated program to a temperature of 0.1° C up to ~ 600 ° C with a resolution of 0.01° C. By varying the temperature, the melting point of a substance can be determined. When appropriate, heating runs can be recorded in video format.

### 2. 2. 1. 2. Thermal analysis

Differential scanning calorimetry for *N*'-2-propylidene-4-hydroxybenzohydrazide was carried out on Mettler Toledo DSC 822e instrument in dynamic helium atmosphere (flowrate 50 mL/min) in the range between -100 °C and 200 °C.

Differential thermal analysis and thermogravimetric analysis for scopolamine bromide hydrate and 4-hydroxybenzohydrazide were performed by Shimadzu DTG-60H at Division for Materials Chemistry, Ruđer Bošković Institute, Zagreb, Croatia in the group of Dr. Marijana Jurić. This instrument varies the sample temperature in accordance with a selected program, and simultaneously measures the change in mass of the sample and the temperature difference between the sample and a standard substance. An analytical balance mechanism (Roberval mechanism) offers precision and high reproducibility.

### 2. 2. 2. Ambiental and *in-situ* high-temperature X-ray powder diffraction

X-ray powder diffraction data for *N*'-2-propylidene-4-hydroxybenzohydrazide, 4-hydroxybenzohydrazide, oxitropium bromide, scopolamine bromide hydrate and scopolamine bromide were collected using a Philips PW 1710 diffractometer at Laboratory for microstructure, Department of Physic, Faculty of Science, University of Zagreb, Croatia in the group of Prof. Željko Skoko. Philips PW 1710 utilizes Brag Brentano geometry and is additionally equipped with a cooling and heating stage that allows *in-situ* non-ambiental measurements. Start and end angle as well as total scan time were determined depending on the sample. Step width must be rounded to a multiple of 0.005 ° (with a minimum of 0.005 °), however, the instrument optics make values below 0.020 ° meaningless. These angular values are given in degrees ($2\theta$). The scan type can be STEP or CONTINUOUS, meaning either one fixed angular value per step at which the counts are collected, or a continuous scan over the angular range of the step during which the counts for that step are collected. For smaller step widths, typically below 0.1°, the difference between these scan types is marginal.

All samples were grounded using mortar and pestle up to the point when a significant decrease in friction is observed. At this point, the average crystallite size is typically at its optimum for X-ray powder diffraction data collection. After the grinding, the powder sample can be 'loosened' to remove any clustering. When necessary, the powder sample was “glued” to a silicon single crystal substrate using a minimal amount of amorphous vacuum grease. The powder samples were further spread out over the surface as evenly as possible. To avoid preferred orientation, no unnecessary force was applied to “glue” the powder sample with vacuum grease. Standard data collection parameters are given in Table 2.

Table 2 Standard parameters for X-ray powder diffraction data collection

| | |
|---|---|
| Start angle (2θ): | 5.0 ° |
| End angle (2θ): | 50.0 ° |
| Scan step width: | 0.02° |
| Scan type: | step |
| Scan step time: | 1 seconds |
| Diffractometer Type: | Philips PW1820/00 |
| Diffractometer Controller: | Philips PW1710/00 |
| Diffractometer Controller: | Philips PW1710/00 |
| Irradiated Length: | 12 mm |
| Receiving Slit: | 0.2 mm |
| Soller Slit Collimator | yes |
| Scatter Slit | 1.0° |
| Sample Holder: | Philips PW1784/25 |
| High Tension Generator: | Philips PW1830/40 |
| Radiation Type: | Cu |
| Radiation Wavelength | 1.54060Å, 1.54438Å α1, α2 |
| Radiation Source: | Philips PW2273/20 Long Fine Focus, 2200W, 60kV max |
| Current: | 30 mA |
| Voltage: | 40 kV |
| Detector: | Philips PW1711/10 Proportional Detector |
| Software package: | Philips PW1877 PC-APD |

Crystal structures were refined by the Rietveld method in HighScoreXpert Plus (Version 4.5, March 2016). The thermal expansion coefficients were calculated from the refined unit-cell parameters obtained from variable temperature diffraction data. The axial thermal expansion coefficients along the principal axes were calculated by using the software PASCal. [64]

### 2. 2. 3. *In-situ* high-temperature X-ray single crystal diffraction

*In-situ* high-temperature single crystal diffraction data for oxitropium bromide, scopolamine bromide and scopolamine bromide hydrate were collected on a Bruker AXS APEXII diffractometer with K-geometry equipped with a CCD area detector (model 1K SMART) at the University of Bari, Italy in the group of Prof. Gennaro Ventruti and in collaboration with Prof. Michele Zema of the University of Pavia, Italy. Experimental

conditions were: graphite-monochromatized Mo*K*α radiation, anode operating at 50 kV and 30 mA, 40 mm crystal-to-detector distance. Full-sphere data collection was used with ω and ϕ scans. In-situ measurements were performed on a home-made device [65] based on the Bruker FR559 heater, that utilizes a vertical air or gas flow to heat the sample. It is mounted externally, just above the crystal at a fixed angle, and therefore it allows full liberty to the rotation of all goniometer circles. A thermocouple is placed at the exit of the gas flow. The blower can make use of air, $N_2$ or other gases to heat the sample, thus allowing studying the high temperature behaviour of crystals under different atmospheric conditions. Standard mounting in quartz vials is also compatible with this set-up for mounting by making use of quartz wool to keep the crystal in position and avoid the use of glues or cements and for sealing the vial under vacuum or other conditions, this method was for the first time employed on the study of thermosalient materials. Temperature precision is ±2 K in the whole temperature range. Data reduction, including intensity integration, correction for Lorentz and polarization effects, was done using the software SAINT-IRIX [66]. A semi-empirical absorption correction was applied to all data using the SADABS package [67]. Preliminary lattice parameters and an orientation matrix were obtained from the xyz centroids of reflections from three sets of frames and refined during the integration process of the intensity data.

Ambiental single crystal diffraction data for scolpolamine hydrate and 4-hydroxybenzohydrazide were collected on Enraf-Nonius CAD-4 with scintillation counter at the Division for Physical Chemistry, Ruđer Bošković Institute, Zagreb, Croatia in the group of Dr. Krešimir Molčanov. The structures were solved using SHELXS97 and refined with SHELXL-2017using the full-matrix least squares refinement [68].

### 2. 2. 4. *In-situ* high-pressure X-ray single crystal diffraction

*In-situ* high pressure single-crystal X-ray diffraction data for scopolamine bromide were measured with a four-circle KUMA X-ray diffractometer with graphite monochromatic Mo *K*α radiation at Adam Mickiewicz University, Poznań, Poland in the group of Prof. Andrzej Katrusiak. Sample was mounted inside the modified Merrill–Bassett diamond anvil cell. Daphne oil was used as the pressure-transmitting medium. Pressure was calibrated with a Photon Control spectrometer by the ruby-fluorescence method with a precision of 0.03 GPa. Data collection, UB-matrix determinations and data reductions were performed with the program CrysAlisPro [69]. Structures were solved by direct method by program ShelXS and refined by full-matrix least-squares on F2 using program ShelXT incorporated in Olex2. [70]

*In-situ* high pressure measurements of the single crystals of *N*'-2-propylidene-4-hydroxybenzohydrazide were performed at the Institute for mineralogy and crystallography, University of Vienna, by dr. sc. Martin Ende. hanol−ethanol. The data sets were measured on a Stoe StadiVari X-ray diffractometer using a DECTRIS Pilatus 300 K detector with a 450 μm silicon layer and an air-cooled Incoatec IμS molybdenum high-brilliance microfocus tube source (50 kV, 1 mA, beam size ≈ 110 μm). Intensities were integrated using the X-area 1.72 (STOE& Cie GmbH) software and corrected for absorption through the sample and DAC components by using the ABSORB code.

### 2. 2. 5. *In-situ* high-temperature Raman spectroscopy

*In-situ* high temperature Raman spectroscopy for *N*'-2-propylidene-4-hydroxybenzohydrazide and oxitropium bromide were measured by Horiba Jobin Yvon T64000 Raman spectrophotometer with a Coherent Innova Argon Laser 400 at the Division for Materials Physics, Ruđer Bošković Institute, Zagreb, Croatia in the group of Dr. Mile Ivanda. It is an integrated confocal micro-Raman system with the confocal microscope coupled to a 460 mm focal length spectrograph equipped with a PC-controlled four interchangeable gratings-turret. The different excitation wavelengths (532 and 633 nm) are supplied by two internal lasers. The T64000 system is designed to provide a versatile platform for Raman analysis. It has an integrated triple spectrometer design for unprecedented optical stability. The instrument incorporates the proven technology of the confocal LabRAM Raman microprobe. The mechanical coupling is rigid and stable. The optical coupling is efficient, and throughput is limited only by theoretical considerations. In using the double subtractive configuration of the T64000, it is possible to obtain spectral information very close into the laser line. The subtractive mode is ideal for studying such detail as LA modes in polymer systems and crystal lattice modes. With the use of the ultra-high resolution triple additive configuration of the T64000 triple system, it is possible to study the position of Raman bands very accurately. This is of particular importance for the measurements of stress in semiconductor materials such as GaN, SiC and diamond where stress induced shifts in the order of 0.1 $cm^{-1}$ are often studied. The high resolution also offers the level of accuracy required for the authentication and certification of materials for Raman standards. With the final mode of operation, the direct spectrograph entrance, the system can be used with holographic notch filter technology and as a more conventional single spectrometer-based system.

## 2. 2. 6. Density functional calculations

DFT calculations were performed at the Division for Theoretical Physics, Ruđer Bošković Institute, Zagreb, Croatia in the group of Dr. Ivor Lončarić. For all DFT calculations a plane-wave basis set code Quantum Espresso [71] with the GBRV pseudopotentials [72] and vdW-DF-cx [73] [74] exchange-correlation functional were used. The plane wave basis set cut-off for wave-functions is 820 eV for stress calculations. In each calculation atoms were relaxed until the change in the total energy was $<10^{-4}$ eV for oxitropium bromide and scopolamine bromide, and $<10^{-5}$ eV for N'-2-propylidene-4-hydroxybenzohydrazide and all the forces were smaller than $2 \cdot 10^{-3}$ eV/Å for oxitropium bromide and scopolamine methyl bromide, while for N'-2-propylidene-4-hydroxybenzohydrazide they were smaller than $5 \cdot 10^{-4}$ eV/Å. Elastic constants were obtained using thermo pw extension of Quantum Espresso package. First Brillouin zone was sampled by the Monkhorst-Pack *k*-point meshes with densities of at least 3 Å

# 3. RESULTS AND DISCUSSION

## 3. 1. *N*'-2-propylidene-4-hydroxybenzohydrazide

### 3.1.1. Thermosalient effect in *N*'-2-propylidene-4-hydroxybenzohydrazide

*N*'-2-propylidene-4-hydroxybenzohydrazide is a typical representative of thermosalient materials that has until now been extensively studied. [9] [63] [75] *N*'-2-propylidene-4-hydroxybenzohydrazide (Figure 15) crystalizes in orthorhombic crystal system with space group $Pna2_1$ and unit cell parameters $a$ = 9.157(4) Å, $b$ = 7.196(3) Å and $c$ = 15.566(6) Å.

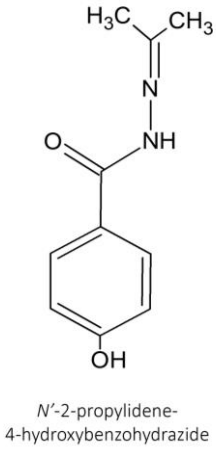



**Figure 15** Chemical formula of N'-2-propylidene-4-hydroxybenzohydrazide

Prior to discussion of novel results regarding the thermosalient effect of *N*'-2-propylidene-4-hydroxybenzohydrazide found in the scope of this thesis, it is important to summarize main conclusions found by Skoko *et. al* and to establish what precisely was left unanswered until now.

The results of previous reports of Skoko *et. al* at can be summarized as follows:

1. *N*'-2-propylidene-4-hydroxybenzohydrazide exhibits two thermosalient phase transitions, first one at ~ 147 °C when Form I irreversibly transform into Form II, and second one around 88 °C when Form II reversibly transforms into Form III. [63]
2. Crystal packings of Form I, II and III contain *zig-zag* chains formed *via* H-bonds. The transformation between forms can be described by comparing it to the process of spring relaxation from tightened form (Form III) to more lose one (Form II). These transformations lead consequently to compression in *b* direction and expansion in *c*.

3. Both polymorphs Form II and Form III are exhibiting extremely large values of thermal expansion especially along the *b* and *c* axis; as a matter of fact, Form III exhibits the largest thermal expansion, $\alpha_c = 368 \times 10^6\ \mathrm{K}^{-1}$ ever noticed in organic or metal-organic crystal.
4. Furthermore, as with the large majority of thermosalient materials, both forms are exhibiting unusually large uniaxial negative thermal expansion (Form II $\alpha_b = -132 \times 10^6\ \mathrm{K}^{-1}$, Form III $\alpha_b = -230 \times 10^6\ \mathrm{K}^{-1}$) being among the largest reported values in any molecular crystal.
5. First principle DFT calculations performed on this system suggested that the uniaxial negative thermal expansion results as a consequence of another extraordinary feature – negative linear compressibility (NLC), meaning that one of the edges of the crystal will increase upon the application of pressure on it. *N*'-2-propylidene-4-hydroxybenzohydrazide exhibits noticeable negative compressibility (Form III $\beta_3 = -28\ TPa^{-1}$; negative compressibility is one order of magnitude larger than other NLC organic compounds, larger than other NLC inorganic solids and rivealed only by the ones of the molecular frameworks, the class of compounds showing the most pronounced NLC behaviour.
6. Another remarkable result obtained by DFT calculations is the explanation provided for the irreversibility of the phase transition from Form I to Form II and reversibility of phase transitions between Forms II and III. This explanation lies in the fact that both transitions from Form II to Form III and *vice versa* proceed through path with relatively small stress, whereas once the Form I transform to Form II possible transition back is not possible because such transition would have to proceed through the pathway generating unfavourably large stress in the lattice.

Since main conclusions regarding the thermosalient effect in this material were theoretically addressed, the main motivation for the research conducted in the scope of this thesis is experimental verification of theoretical concepts:

1. DFT calculations suggested that *N*'-2-propylidene-4-hydroxybenzohydrazide exhibits the negative linear compressibility, therefore, in order to verify it experimentally, the *in-situ* high-pressure X-ray diffraction experiments were conducted.
2. DFT calculations showed that enlargement of the unit cell causes small softening of low energy vibrations, suggesting that Grüneisen parameters for *N*'-2-propylidene-4-hydroxybenzohydrazide are positive (for all three forms), therefore, in order to verify it, a

relationship between experimental temperature expansion coefficients and linear compressibility coefficients was investigated in detail.

3. DFT calculations also proposed that the behaviour of low energy phonons, representing joint movements in the crystal lattice, assist the thermosalient transformation between forms. To inspect behaviour of low modes the *in-situ* high temperature Raman spectroscopy at low frequencies was performed on *N*'-2-propylidene-4-hydroxybenzohydrazide.
4. Finally, the propagation of sound through all three forms of *N*'-2-propylidene-4-hydroxybenzohydrazide was studied aiming to determine existence of preferable propagation directions of elastic waves and energy.

Linear compressibility coefficients for *N*'-2-propylidene-4-hydroxybenzohydrazide Form I, theoretically determined by [9] using the methodology described in Section 3.2.7, are shown in Figure 16.

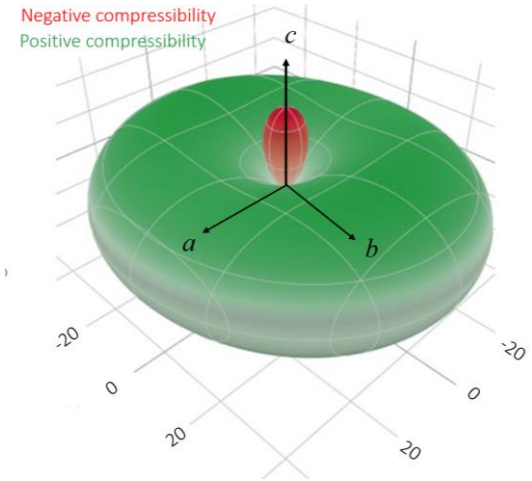



Figure 16 Linear compressibility indicatrix of N'-2-propylidene-4-hydroxybenzohydrazide Form I determined from DFT stiffness matrix calculations.

To confirm the existence of negative compressibility along *c*-direction as obtained with DFT calculations, *in-situ* high-pressure single crystal X-ray diffraction experiments were performed on *N*'-2-propylidene-4-hydroxybenzohydrazide Form I. The temperature of the sample was kept at constant 31°C. A high-pressure experiments were performed in a modified Merrill–Bassett diamond anvil cell. Six sets of diffraction data were collected with pressure varied in the range from 0 to 2.5 GPa. Silicon oil was used as pressure medium because the crystal is solvable in another typical protic solvents such as EtOH. Poor crystal quality prevented structure determination of high-pressure forms, nevertheless, the change in unit-cell parameters and crystal system as a function of pressure were successfully determined. Lattice parameters

of *N*'-2-propylidene-4-hydroxybenzohydrazide Form I as a function of pressure are shown on Figure 17.

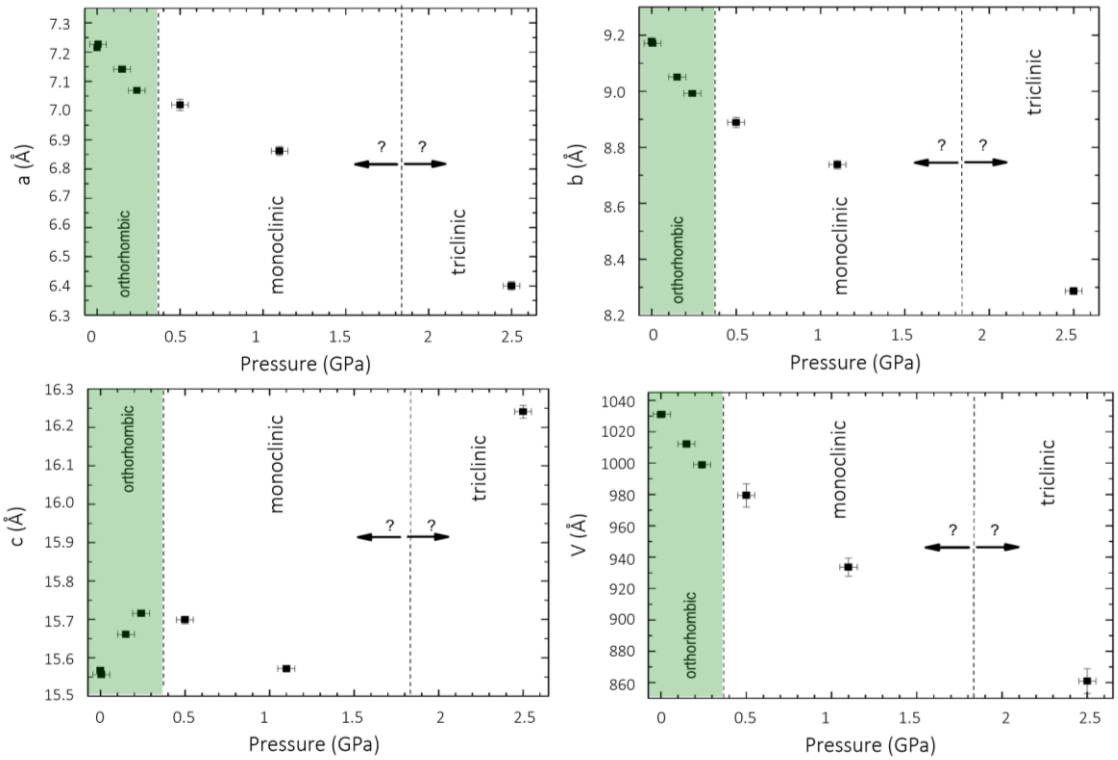



Figure 17 Lattice parameters of N'-2-propylidene-4-hydroxybenzohydrazide Form I as a function of hydrostatic pressure determined by in-situ high-pressure single crystal diffraction.

Figure 17 shows that positive compressibility of Form I along *a* and *b* axis is, indeed, accompanied with the negative compressibility along *c* axis in the pressure range $p$ = 0 - 0.4 GPa (shaded in green). Based on the lattice parameters, the linear compressibility coefficients $K_i$ for *N*'-2-propylidene-4-hydroxybenzohydrazide Form I along the principal axis $i$ = 1, 2 and 3 were calculated and shown in Table 3.

Table 3 Liner compressibility coefficients $K_i$ for *N*'-2-propylidene-4-hydroxybenzohydrazide Form I along principal axis *i*=1, 2 and 3 determined from *in-situ* high-pressure single crystal X-ray diffraction.

| | | *Component of* $\mathbf{x}_i$ *along the crystallographic axes* | | |
|---|---|---|---|---|
| *Principal axis,* i | $K_i$ ($TPa^{-1}$) for Form I | *a* | *b* | *c* |
| *1* | 93 | 0 | -1 | 0 |
| *2* | 86 | -1 | 0 | 0 |
| *3* | -37 | 0 | 0 | 1 |

Corresponding compressibility indicatrix for *N*'-2-propylidene-4-hydroxybenzohydrazide form I along principal axis $i$ = 1, 2 and 3 is visualized in Figure 18.

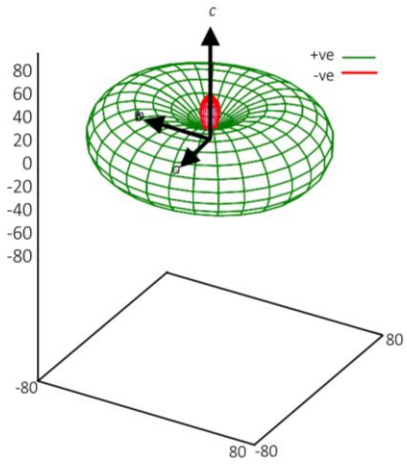



**Figure 18** Compressibility indicatrix for N'-2-propylidene-4-hydroxybenzohydrazide Form I determined by the in-situ high pressure single crystal X-ray diffraction.

Comparison between experimentally determined values of compressibility coefficients $K_i$ and the coefficients determined by DFT calculations is given in Table 4.

**Table 4** Linear compressibilities coefficients for *N*'-2-propylidene-4-hydroxybenzohydrazide Form I as obtained experimental *in-situ* high pressure single crystal X-ray diffraction vs. those obtained by DFT.

| | | | *Component of* $\boldsymbol{x}_i$ *along the crystallographic axes* | | |
|---|---|---|---|---|---|
| | $K_i$ (TPa$^{-1}$) for Form I | | | | |
| Principal axis, i | experiment | DFT | *a* | *b* | *c* |
| *1* | 93 | 51 | 0 | -1 | 0 |
| *2* | 86 | 46 | -1 | 0 | 0 |
| *3* | -37 | -24 | 0 | 0 | 1 |

From Table 4 it can be see that both DFT and experiment showed that compressibilities coefficients for Form I of *N*'-2-propylidene-4-hydroxybenzohydrazide along principal axes 1 and 2 (corresponding to crystallographic direction *a* and *b*) should be of similar values. Although clearly the absolute values of linear compressibilities coefficients obtained from DFT and experiment are not the same, the same trend is, indeed, observed in both cases; both experiment and DFT showed that linear negative compressibility exists along the principal axis 3 (corresponding crystallographic direction *c*) and they, roughly, differ by the factor of two. Negative linear compressibility (NLC) defines an uncommon property of material to expand along at least one direction when subjected to uniform external pressure. Despite the counterintuitive character the phenomenon does not violate basic thermodynamic principle of overall volume reduction under pressure and may lay foundation for development of effectively incompressible materials for various practical applications, including materials for artificial muscles, amplification of piezoelectric response in sensors and actuators, tuneable sieves for filtration, "smart" body armour made of robust shock absorbing materials, sensitive pressure

detectors, materials used at deep sea, etc. Until today, only a handful of NLC materials have been discovered, the majority of which are inorganic systems. The most well-known examples are $LaNbO_4$, elemental Se, and $BAsO_4$ with the α-cristobalite structure. [76] [77] [78]. Goodwin *et al.* ascribed the large NLC effect ($-5\ TPa^{-1}$) in the cyanide framework, $Ag_3[Co(CN)_6]$, to the 'wine-rack' motif [79] [80]. Very recently, the strongest NLC effect ($-12\ TPa^{-1}$) was discovered in the related framework, $KMn[Ag(CN)_2]_3$, in which the inclusion of extra-framework counterions appears to frustrate the soft phonon modes responsible for destroying NLC [46].It has also recently been demonstrated that small molecule organic systems can adopt NLC behavior, such as the hydrogen-bonded 'lattice fence' arrangement in methanol monohydrate, giving rise to NLC of $-3.8\ TPa^{-1}$ [81] [82]. It is most important to emphasize that the negative compressibility of *N*'-2-propylidene-4-hydroxybenzohydrazide that amounts -37 $TPa^{-1}$ represent, indeed, an unprecedent value ever reported; the largest value of NLC reported until now was found by Katrusiak for co-crystal of bis[2-methyl-5-(pyridyl)-3thienyl]cyclopentene with 1,4-diiodotetrafluorobenzene and amounts to -30 $TPa^{-1}$ [83], it is suited to write a remark regarding the fact that NCT was initially found by theoretical calculations and later on confirmed by experiment; it is well known that large unit cells of the crystal, such as the case for *N*'-2-propylidene-4-hydroxybenzohydrazide, often prohibit the use of high-level quantum chemistry calculations, however, with the recent progress in development of density functional theory with the van der Waals interactions, the good accuracy and predictability in modelling of molecular crystals has become accessible. It fair to say that *N*'-2-propylidene-4-hydroxybenzohydrazide represents an excellent showcase where experimental compressibility study using high-pressure X-ray diffraction, indeed, proves that nonempirical vdWDF-cx functional is completely capable to accurately describe the elastic properties for molecular systems.

Beside the determination of compressibility coefficients of *N*'-2-propylidene-4-hydroxybenzohydrazide Form I, another important finding was realized from the *in-situ* high-pressure single crystal X-ray diffraction experiment. As shown in Figure 17, *N*'-2-propylidene-4-hydroxybenzohydrazide Form I experiences two phase transitions in this region of pressure; at $p = 0{,}4$ GPa orthorhombic Form I transforms to monoclinic polymorph. Monoclinic structure remains stable up to ~1,8 GPa where it transforms to triclinic system. Due to the decreased quality of the crystal, it was possible to measure only two points in monoclinic region and one point in triclinic region but seems that triclinic form exhibits negative compressibility along *c* axis.

High cost of Grüneisen parameters calculations for large molecular systems such as *N*'-2-propylidene-4-hydroxybenzohydrazide was addressed in the paper by Skoko. [9] In this paper, the sign of $I(T)$ vector, that is proportional to Grüneisen parameters, has been determined based on single calculation of vibrational frequencies change as a function of lattice constants. A small softening of low energy vibrations was observed for enlarged unit-cell thus a positive value for $I(T)$ have been assumed. If one compares experimental thermal expansivity indicatrix and the compressibility indicatrix shown in Figure 19, it becomes obvious that thermal expansion and compressibility are directly proportional meaning that the sign of $I(T)$ was, indeed, calculated correctly.

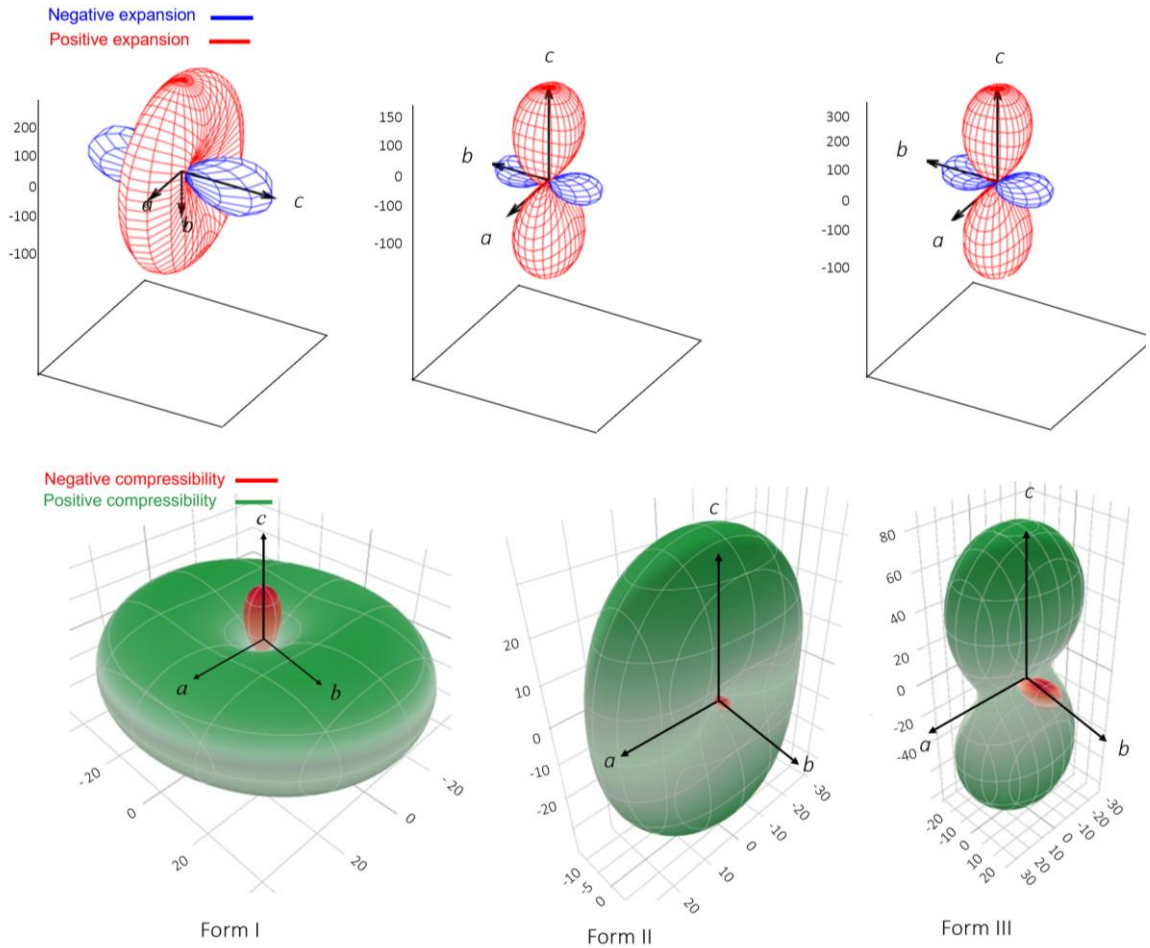



Figure 19 Comparison of thermal expansivity indicatrix and the compressibility indicatrix for N'-2-propylidene-4-hydroxybenzohydrazide Form I, II and III.

As an alternative to squandering of computational resources on the expensive calculation of $I(T)$ sign, in this thesis an alternative approach was proposed: exploitation of the relationship between experimental thermal expansion behaviour and compressibility to determine the exact values for $\gamma_1$, $\gamma_2$ and $\gamma_3$ components of Grüneisen parameter. This approach is, of course,

feasible in the cases when thermal expansion behaviour is already known from the experiments. By using Equation 11 that links the experimental thermal expansion ($\alpha_1$, $\alpha_2$, $\alpha_3$): for Form I: (267, 274, -271) $\times 10^{-6}$ $K^{-1}$, for Form II: (28, -131, 186) $\times 10^{-6}$ $K^{-1}$, for Form III: (63, -230, 368) $\times 10^{-6}$ $K^{-1}$ and elastic compliance matrix ($C_{11}$, $C_{12}$, $C_{13}$, $C_{22}$, $C_{23}$, $C_{33}$ ) for Form I: (22.3, 6.8, 15.2, 27.0, 28.3, 47.3) GPa, for Form II (23.5, 10.8, 11.5, 34.8, 26.7, 24.4) GPa and for Form III (31.3, 11.6, 7.2, 51.7, 27.1, 19.7) GPa., and assuming for hypothesis that the ratio $C_V/V$ is equal to one, $\gamma_1$, $\gamma_2$ and $\gamma_3$ components of Grüneisen parameter for *N*'-2-propylidene-4-hydroxybenzohydrazide Form I, II and III have been calculated (Table 5).

Table 5 Components of Grüneisen parameters $\gamma_1$, $\gamma_2$ and $\gamma_3$ for N'-2-propylidene-4-hydroxybenzohydrazide Form I, II and III

| | $\gamma_1$ | $\gamma_2$ | $\gamma_3$ |
|---|---|---|---|
| Form I | 36981 | 15443 | -9786 |
| Form II | 13822 | 7098 | 13627 |
| Form III | 19535 | -11874 | 14702 |

To avoid the confusion, it is important to strike out that in the case of Form I, $\gamma_1$ and $\gamma_2$ being positive and $\gamma_3$ being negative, resulted in the overall positive proportionally between expansion and compressibility. The same positive proportionally was found for Form II (having all positive components) as well for the Form III (with $\gamma_1$ and $\gamma_3$ being positive and $\gamma_2$ being negative). This positive proportionally, in other words, means that thermal expansion arises as a direct consequence of the elastic properties of a material, meaning that negative expansions, a feature most relevant for thermosalient effect, is caused by another extraordinary property - negative compressibility.

In the paper by Skoko *et al.* [9] it was also proposed that the behaviour of low energy phonons ($\omega < 10$ meV), representing joint movements in the crystal lattice, which can easily be excited at the temperatures of phase transitions, assist the thermosalient transformation between forms. In order to inspect behaviour of low modes in three different forms Raman spectroscopy at low frequencies was performed on *N*'-2-propylidene-4-hydroxybenzohydrazide. *In-situ* variable temperature Raman spectra for Form I (at 300 K and 413 K; approaching phase transition from Form I to Form II) and for Form II (at 443 K and 373 K; approaching phase transition from Form II to Form III) are shown on the Figure 20.

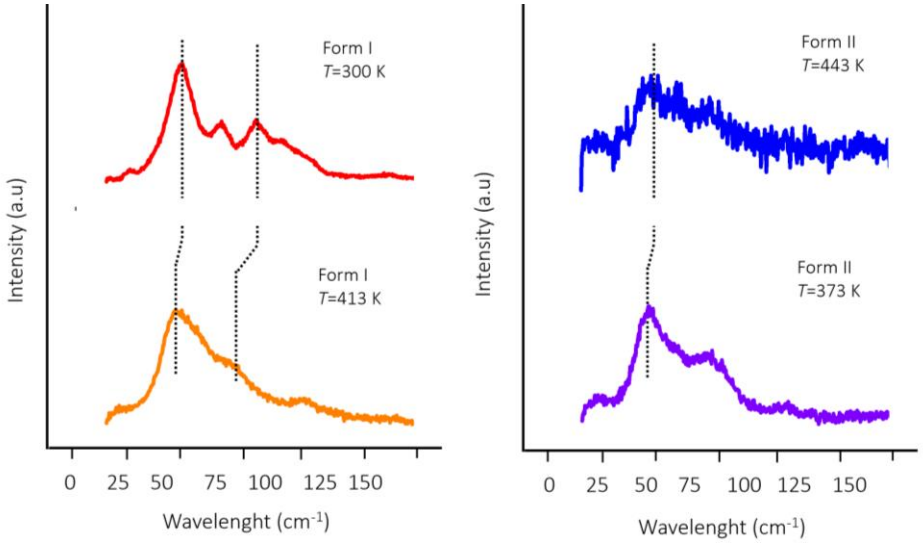



**Figure 20** In-situ high-temperature Raman spectra for N'-2-propylidene-4-hydroxybenzohydrazide Form I (approaching phase transition from Form I to Form II) and for Form II(approaching phase transition from Form II to Form III).

Peak positions of low frequency Raman modes found in the spectra are listed in Table 6.

**Table 6** In-situ high-tempearture low frequency Raman peaks positions of N'-2-propylidene-4-hydroxybenzohydrazide Form I and Form, obtained by Pseud-Voight fitting.

| $\tilde{\nu}$ (cm$^{-1}$) | | | |
|---|---|---|---|
| Form I | | Form II | |
| 300 K | 413 K | 443 K | 373 K |
| 48 | 47 | 48 | 46 |
| 65 | 64 | | 71 |
| 84 | | | |
| | | | 103 |
| 136 | | | |
| 294 | | | |
| | | | 389 |
| 427 | | | |
| 505 | 497 | | |
| | | | 608 |

As stated in Section 1.2. one of the peculiarities of thermosalient phase transitions is their rapidness. In the structural phase transitions, typically, the transformation occurs quasi-stationary. Just before the phase transition happens, the long-range correlation occurs, for $T$=$T_C$ the two phases coexist, order parameter goes to infinity and finally the parameter fluctuations transfer the one crystal phase to another phase. [9] On the other hand, in jumping crystals, thermosalient phase briskly and that transition is non-stationary. Such rapidness can only be obtained by joint molecular displacements. Anwar *et al.* [84] suggested that such transformation, that occurs *via* joint movement, is due to the specific lattice vibration (phonon), which frequency goes to zero on the temperature of transformation and that the molecular displacements associated with that phonon are those that result in the new phase [84]. In the

paper by Skoko *et al.* phonon with frequency approaching zero was not found but instead a softening of several low energy vibrations (frequency decrease up to the order of 10%) was observed. By inspecting the Raman peak positions given in Figure 20 and Table 6 it is obvious that the low frequency modes of Form I shift to lower frequencies with heating, as the system approaches the temperature of phase transition to Form II. On the other hand, for the Form II the modes are shifting towards lower frequencies on cooling, again as the system approaches the temperature of phase transition to Form I. Based on experimental conformation of DFT calculation we propose that even a slight softening of low energy phonon modes helps in overcoming the barrier in the Gibbs potential energy and afterwards the system violently collapses to the new minimum, which in turn might explain such a rapid response and jumping.

Finally, we have extended our study to investigation of sound propagation sound in *N*'-2-propylidene-4-hydroxybenzohydrazide Form I, II and III. Sound propagation was calculated using a software *Christoffel*, a Python tool for calculating direction-dependent phase and group velocities based on the stiffness tensor of a solid. [63] The group velocities for *N*'-2-propylidene-4-hydroxybenzohydrazide Form I, II and III are shown in the Figure 21.

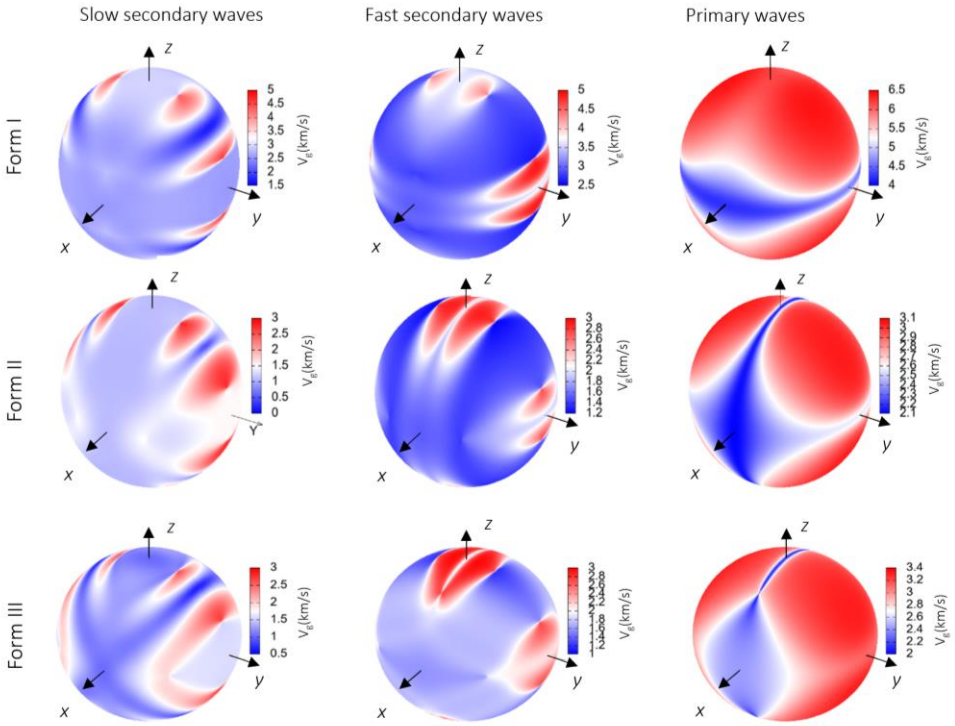



Figure 21 Sound waves group velocities for three forms of N'-2-propylidene-4-hydroxybenzohydrazide.

In general, the phase velocity refers to the velocity of a monochromatic plane however, real sound is never purely monochromatic nor purely planar thus it is better to consider a wave

packet with a small spread both in wavelength and direction of travel. The velocity of such wave packet, formed by the superposition of these phase waves, is called the group velocity. From Figure 21 it is obvious that the group velocity of transversal modes (secondary waves) does not change significantly between the three forms. On the other hand, longitudinal modes (primary waves, sound) change their velocity, and the velocity is significantly reduced from Form I to Form II. Their spatial distribution also changes, with the spatial shape of propagation being similar for Form II and Form III. Speed of the longitudinal waves is 6 km/s in the Form I (in *b* direction), whereas it 3 km/s in both Forms II (in the *ac* plane, diagonal direction) and Form III (in *a* direction). This could provide another support for explanation given in Skoko *et al.* for the irreversibility of the phase transition I – II and the reversibility of the phase transition II – III. It was stated that once the Form II is formed, possible transition back to Form I by cooling would have to proceed through the pathway generating unfavourably large stress in the lattice. Since the speed of longitudinal waves in Form I is much different than in the Forms II and III (where the speed is actually the same) it can be concluded that the elastic properties of the Forms II and III are similar and different from the Form I and therefore it is much easier for the system to transform from Form II into Form III than into Form I.

To confirm this concept, anisotropy indexes, that provide an insight into the most favourable stress pathway, were calculated for all three forms of *N*'-2-propylidene-4-hydroxybenzohydrazide and given in the 6. Anisotropy index is defined in [62] as $A^L = \sqrt{\left[ln\left(\frac{\kappa^V}{\kappa^R}\right)\right]^2 + 5\left[ln\left(\frac{\mu^V}{\mu^R}\right)\right]^2}$, where $\mu^V$ and $\mu^R$ are upper (Voigt) and lower shear moduli (Reuss average), and $\kappa^V$ and $\kappa^R$ are upper and lower bulk moduli. These calculations can be done assuming the elastic constants are well known and are valid for any symmetry (from cubic to triclinic).

Table 7 Anisotropy parameters for three forms of N'-2-propylidene-4-hydroxybenzohydrazide from elastic constants

| | Anisotropy index |
|---|---|
| | $A^L$ |
| Form I | 0.88798 |
| Form II | 2.2104 |
| Form III | 1.6599 |

Anisotropy index of Form II is similar to that of Form III, indicating on a favourable passage between these two configurations, that requires less stress, compared to transformation of Form II to Form I.

In summary, experimental results presented in Section 3.1.1 fully confirmed all the theoretical calculations on *N*'-2-propylidene-4-hydroxybenzohydrazide previously reported by

Skoko *et al.*[9] High pressure diffraction experiments, indeed, proved the existence of negative linear compressibility of *N*'-2-propylidene-4-hydroxybenzohydrazide. Also, the components of Grüneisen parameter for all three forms have been calculated confirming that negative thermal expansion is coupled with negative compressibility. At the end, we feel necessary to address this coupling but to do so, first the structural mechanism that explains uniaxial negative compressibility and negative expansion must be explained. Crystal packing of Form III is shown in Figure 22.

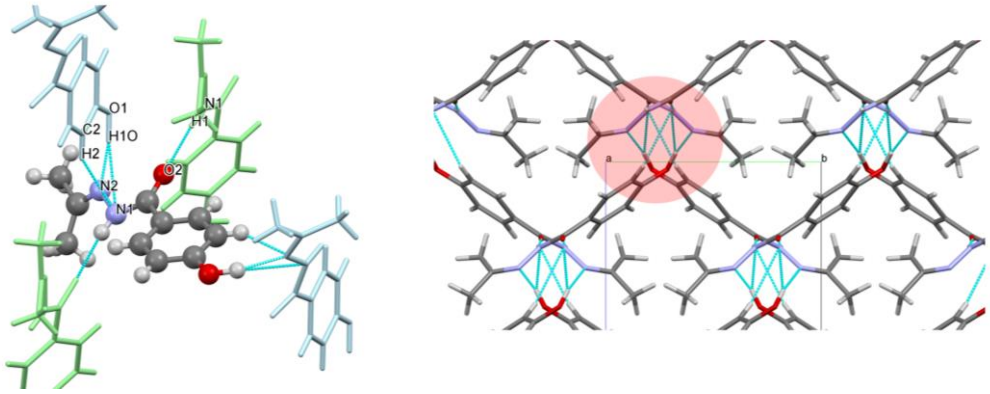



**Figure 22** Crystal packing of N'-2-propylidene-4-hydroxybenzohydrazide Form III

We can observe *N*'-2-propylidene-4-hydroxybenzohydrazide molecule form two hydrogen bonds that involve N1 nitrogen atom from hydrazide group [N1···H10-O1 and N1···H2-C2], one hydrogen bond that involved N2 nitrogen atom from hydrazide group [N2···H2-C2] and one hydrogen bond that involve carbonyl oxygen atom O2 from hydrazide group [O2···H1-N1]. On the right-hand side of the figure, we can observe that such hydrogen bonds form a flexible hinge (coloured in red). Considering the extended packing (Figure 23, left side), a *wine-wrack* network of *N*'-2-propylidene-4-hydroxybenzohydrazide can be observed.

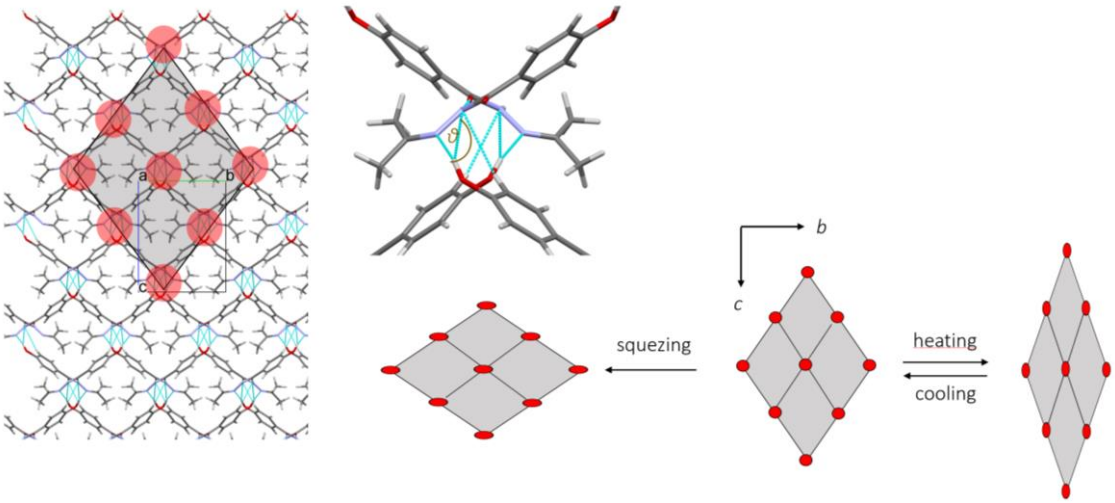



**Figure 23** Inverse relationship of N'-2-propylidene-4-hydroxybenzohydrazide Form III

With heating, the hinge angle $\theta$ increases from 112.81 ° to 115.68 ° that consequently results both the *c*-directed elongation and the shrinkage along *b* axis. Such movement of flexible 'hinges' within the wine-wrack network allows coupling of orthogonally directed negative compressibility with positive linear compressibility as well as orthogonally directed negative expansion with positive expansion. Additionally, we can that the structural changes upon compression are similar to those upon cooling – thus the relationship of expansion and compressibility can be considered as *"inverse"* as shown in bottom part of Figure 23. The general empirical evidence reported so far mainly for many minerals, but also for framework materials, MOFs, as well as organic compounds, show that in most cases, the temperature and pressure, indeed, cause the opposite strain, that is, the negative linear compressibility exists in the direction of negative thermal expansion.

Coupling of negative thermal expansion with negative compressibility was found for Form I, however it is somewhat peculiar that negative thermal expansion (as well as negative compressibility) for Form I is not in the same direction as for Form I and II as shown in Figure 19. Reason for different direction of negative expansion in Form I (compressibility) compared to Form II and III is due to a different motive found in crystal packing network (Figure 24).

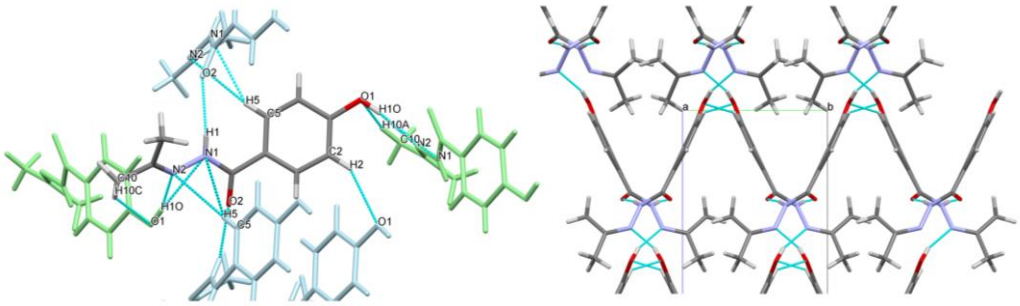



Figure 24 Crystal packing of N'-2-propylidene-4-hydroxybenzohydrazide Form I

We can observe *N*'-2-propylidene-4-hydroxybenzohydrazide molecule Form I form three hydrogen bonds that involve N1 nitrogen atom from hydrazide group [N1···H5-C5, N1···H10-O1 and N1-H1···O2] and two hydrogen bond that involved N2 nitrogen atom from hydrazide group [N2···H10-O1 and N2···H5-C5]. On the right-hand side of the figure, we can observe that such hydrogen bonds form a flexible hinge (coloured in red). Considering the extended packing (Figure 25, left side), a *wine-wrack* network of *N*'-2-propylidene-4-hydroxybenzohydrazide can be observed.

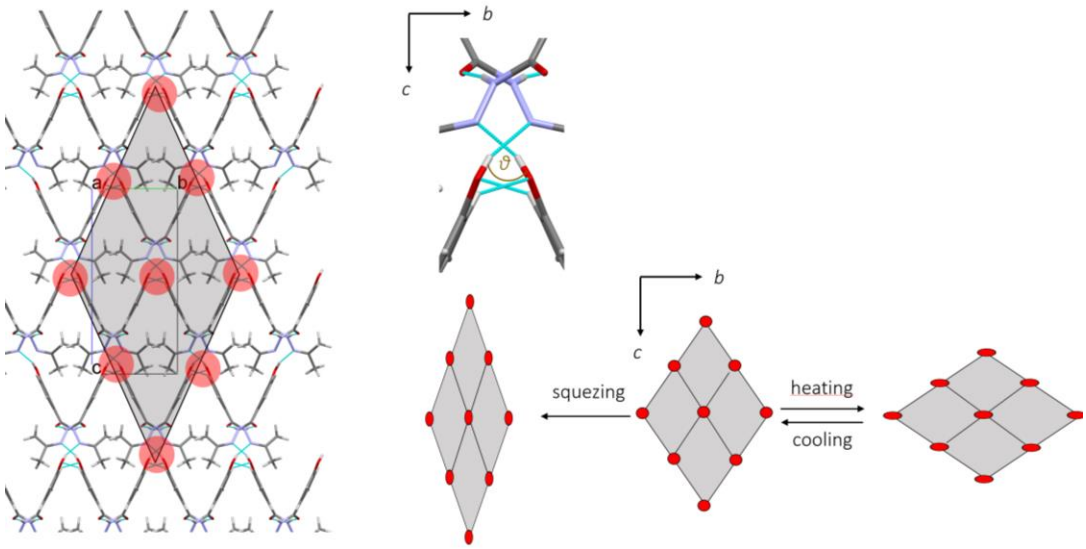



Figure 25 Crystal packing of N'-2-propylidene-4-hydroxybenzohydrazide Form I

With heating, the hinge angle $\theta$ increases from that consequently results both the *c*-directed elongation and the shrinkage along *b* axis. Such movement of flexible 'hinges', as it was the case for Form III, again allows coupling of orthogonally directed negative compressibility with positive linear compressibility as well as orthogonally directed negative expansion with positive expansion. Finally, Results of Raman measurements also suggested that intermolecular changes are occurring during heating, which is in accordance with findings realized by the inspection of wine-wrack network.

## 3. 1. 2. Derivatives of *N*'-2-propylidene-4-hydroxybenzohydrazide

### 3. 1. 2. 1. The case of 4-hydroxybenzohydrazide

In the paper by Skoko *et al*.[9] it was clearly demonstrated that the specific motive found in the crystal packing of *N*'-2-propylidene-4-hydroxybenzohydrazide plays the pivotal role for the observed thermosalient effect. At this point, a new question emerged: what would happen if small, but well-thought, structural modification is introduced into a system already known to exhibit thermosalient behaviour? Considering prior accumulated knowledge, one might expect that thermosalient effect will, indeed, be extremely sensitive to subtle changes in the chemical composition such as changes in a functional group and/or incorporation of solvent molecules. It was shown that interpenetrated spring-like motive with flexible hinges in *N*'-2-propylidene-4-hydroxybenzohydrazide forms, among other, due to the intermolecular hydrogen bonds established between N2 atom of hydrazide group and hydroxy group from benzene moiety however it is also reasonable to assume that hydrogen bonding potential of hydrazide group is

somewhat restricted due to steric hinderance caused by the bulky propylidene group attached to N2 atom. In order to increase the ability of hydrazide group to form more excessive H-bond networking, the ketone elimination reaction (nucleophilic attack of water molecules) was conducted, finally yielding 4-hydroxybenzohydrazide.

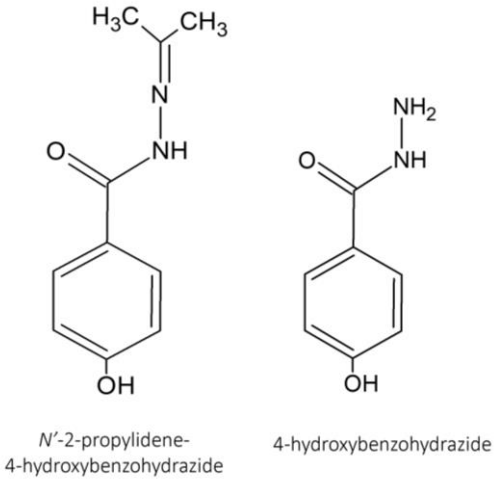



Figure 26 Chemical formula of *N*'-2-propylidene-4-hydroxybenzohydrazide and its derivative 4-hydroxybenzohydrazide

The structure of 4-hydroxybenzohydrazide has been determined by the single-crystal diffraction data; the structure crystallize in the monoclinic system ($P2_1/c$) with the unit-cell parameters $a$ = 5.0666(2) Å, $b$ = 17.2597(5) Å, $c$ = 7.8340(2) Å and $\beta$ = 93.502(3) °. Figure 27 shows the crystal structure of 4-hydroxybenzohydrazide in *bc* plane; the lattice contains four molecules.

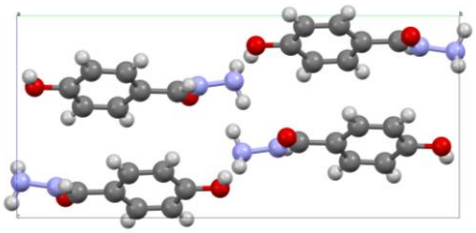


Figure 27 Crystal structure of 4-hydroxybenzohydrazide.

Figure 28 shows hydrogen bonding network of propylidene-deficient derivative 4-hydroxybenzohydrazide.

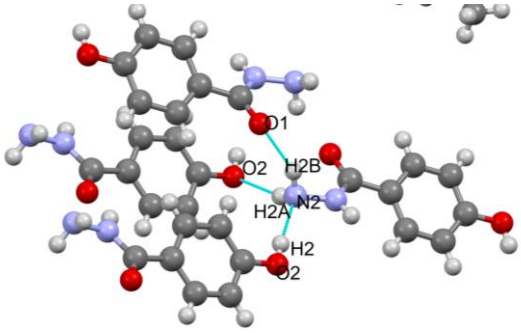



**Figure 28** Hydrogen bonding in propylidene-deficient derivative 4-hydroxybenzohydrazide.

It can be clearly seen that steric effects of propylidene group significantly influences the ability of hydrazide functional groups to participate in the H-bonding. In the case of *N*'-2-propylidene-4-hydroxybenzohydrazide nitrogen atom N2 acts as hydrogen atom acceptor in the hydrogen bond with hydroxyl group from benzene moiety of neighbouring molecule [O1-H10···N2] while in the case of 4-hydroxybenzohydrazide N2 atom participate in the formation of three hydrogen bonds. Atom N2 acts as a hydrogen bond donor towards *i*) carboxylic oxygen atom from first neighbouring molecule [N2-H2B···O1] and *ii*) hydroxylic oxygen atom from second neighbouring molecule [N2-H2A···O2] and finally as a hydrogen bond acceptor towards hydroxylic OH group from third molecule [O2-H2···N2]. Considering such a diverse H-bonding behaviour it does not come a surprise that spring-like crystal packing with flexible hinge as found in *N*'-2-propylidene-4-hydroxybenzohydrazide is not retained in the case of 4-hydroxybenzohydrazide as shown in Figure 29.

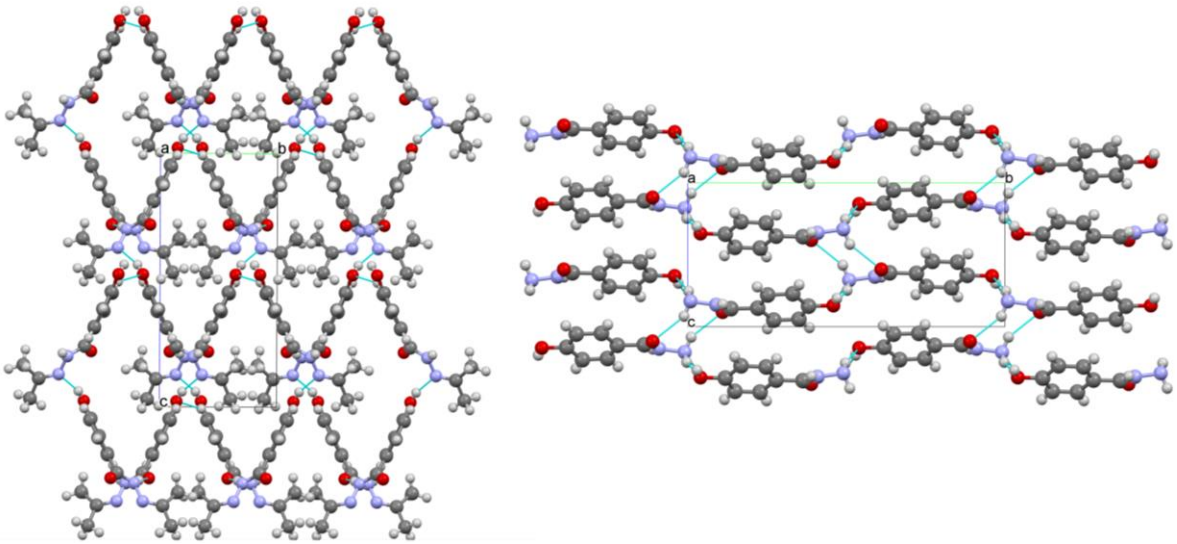



**Figure 29** Crystal packing of N'-2-propylidene-4-hydroxybenzohydrazide and 4-hydroxybenzohydrazide.

Hot-stage microscopy experiment has been performed on 4-hydroxybenzohydrazide and, as suspected, no thermosalient effect was noticed. That finally confirmed that the presence of

interpenetrated *zig-zag* spring-like chains that are mutually connected in 3D wine-wrack network truly play a pivotal role in the manifestation of thermosalient effect.

### 3. 1. 2. 2. Recrystallization of *N*'-2-propylidene-4-hydroxybenzohydrazide

Additionally, attempts to recrystallize *N*'-2-propylidene-4-hydroxybenzohydrazide from several solvents have been conducted. Unlike in the case of oxitropium bromide, where the major idea was to prepare a solvate derivative that possess an increased hydrogen bonding potential, the idea behind the recrystallization attempts in the case of *N*'-2-propylidene-4-hydroxybenzohydrazide was to explore the possibility of formation of high-temperature polymorphic phase at RT. Such approach was demonstrated by Skoko *et al.* [9]; it was reported that high-temperature polymorph can be prepared at room temperature by crystallization from different solvents. While the recrystallization of *N*'-2-propylidene-4-hydroxybenzohydrazide from different polar aprotic solvents (protic solvent could not have been used due to the reactivity with hydrazide group) have not yielded the formation of HT Form II, interesting feature was noticed in the case of recrystallization from 1:1 mixture of acetone and dichloromethane. Figure 30 shows Rietveld refinement of *N*'-2-propylidene-4-hydroxybenzohydrazide recrystalized from acetone-DCM of the X-ray powder diffraction data collected at RT. Refinement was carried out by using the split-type pseudo-Voigt profile function and the polynomial background model. Isotropic vibration modes were assumed for all atoms. During the refinement, a zero shift, scale factor, half-width parameters, asymmetry and peak shape parameters were simultaneously refined.

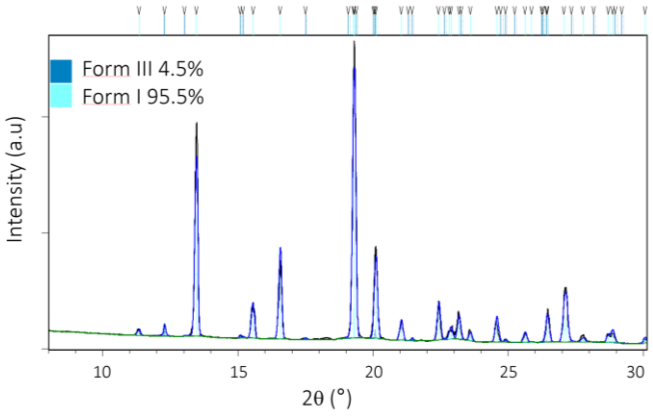



**Figure 30** Rietveld refinements for N'-2-propylidene-4-hydroxybenzohydrazide recrystallized from acetone-DCM. Experimental data are given as black line, calculated diffraction pattern as blue line while the sky blue and turquoise vertical lines represent positions.

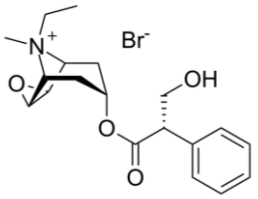
From Figure 30 it is obvious that recrystallization from 1:1 mixture of acetone and dichloromethane led to the simultaneous formation two *N*'-2-propylidene-4-

hydroxybenzohydrazide polymorphs, Form I and Form III. Although this outcome is not what one would usually expect, it is nevertheless not totally surprising when dealing with polymorphs. As stated by Bernstein and Dunitz [85], in molecular crystals free energy differences between polymorphs are usually quite small, a matter of few kilocalories/mole at most, and depend on temperature, mainly because of the entropic contribution to the free energy. Because of the thermodynamic relationship $G = H - TS$, the form with the higher entropy will tend to become the thermodynamically more stable as the temperature is raised. Thus, over a small temperature range, one polymorph or another can change from being the stable form to metastable. The primary crystallization process involves the formation of critical nuclei of the new phase, followed by their growth. The nucleation step is critically dependent of the presence of "suitable" defects and depending on these defects nuclei of the new phase may be formed at different temperatures and grow at different rates. Obviously, recrystallization from 1:1 mixture of acetone and dichloromethane favours the formation of both forms stable at room temperature, Form I and Form III. The processes leading to the formation of certain polymorphs from different solvents is unfortunately still far beyond our understanding, but as Bernstein [85] stated – we believe that once a particular polymorph has been obtained, it is *always* possible to obtain it again; it is only a matter of finding the right experimental conditions. And it is exactly on this premise that the whole field of crystal engineering is based upon, but it goes beyond the scope of this thesis.

# 3. 2. Oxitropium bromide

## 3. 2. 1. Thermosalient effect in oxitropium bromide

Section 4.1. has been dealing with thermosalient effect in *N*'-2-propylidene-4-hydroxybenzohydrazide. As it was realized that the coupling of thermal expansion with compressibility plays an important, if not a pivotal, role in the manifestation of thermosalient effect in *N*'-2-propylidene-4-hydroxybenzohydrazide it seemed just reasonable to inspect both the thermal expansion behaviour and compressibility in yet another system - oxitropium bromide. The thermosalient effect in oxitropium bromide is described by Skoko *et al.* [17] Results presented in this thesis are a natural continuation of previous investigations which revealed that the jumping of the crystals of oxitropium bromide is a macroscopic manifestation of a highly anisotropic change in the unit-cell volume which happens briskly during the thermosalient phase transition. Oxitropium bromide has chemical formula $C_{19}H_{26}BrNO_4$ and it crystalizes in orthorhombic system belonging to space group $P2_12_12_1$ with unit cell parameters $a$ = 7.3914(4), $b$ = 10.1215(6), $c$ = 24.690(1). Molecular formula is shown on Figure 31.




Oxytropium bromide
($C_{19}H_{26}BrNO_4$)

**Figure 31** Molecular formula of oxitropium bromide

The work of Skoko *et al.* [17] represents the first systematic study of a thermosalient material with different experimental techniques. Therefore, prior to the discussion of novel results found in this thesis, it is important to summarize main conclusions found by Skoko *et al.* and to establish what precisely was left unanswered until now. In summary, the facts regarding the thermosalient effect in oxitropium bromide can be summarized as follows:

1. The transition of low temperature oxitropium bromide Form A to high temperature oxitropium bromide Form B, occurring at 318 K, is accompanied by a highly anisotropic volume expansion by 4% of the cell, in which the *b* axis increases by 11% and the *c* axis decreases by 7%.
2. The flexibility at the ester bridge results in conformational differences between the two phases, which are manifested as different orientations of the two terminal groups relative to the molecular backbone: the phenyl ring and the hydroxyl functionality, play an important role in the mechanism of polymorphic transition.
3. Acoustic emission during the phase change were measured experimentally and the detection of this emission proves the existence of mechanical stresses and strains in the crystal undergoing the phase change, consistent with the martensitic transition.
4. Experimental observations suggest that thermosalient phenomena contain many elements of martensitic phase transformations in metals which are characterized by cooperative, homogeneous movements resulting in a change in the crystal structure.
5. The phase transition from oxitropium bromide Form A to Form B can be induced by mechanical pressure and UV-light, not only by heating.
6. Crystals of oxitropium bromide Form A were obtained from dichloromethane and from acetonitrile/dichloromethane and methanol/dichloromethane mixtures. Oxitropium bromide Form B was obtained (stable at room temperature) as prismatic crystals by slow evaporation from dichloromethane, acetone, or chloroform.

7. The authors proposed a possible two-step mechanism of the jumping phenomenon in this system based on the experimental observations. The first step involves the change in conformation of a number of molecules from one conformational local energy minimum to another and results in a packing arrangement that does not stabilize that conformation, resulting in the generation of mechanical strain, as in the compression of a spring. The second step is a simultaneous or concomitant process involving decompression of the "spring", which is released by the crystal jumping, accompanied by a relaxation of the molecules to a conformation similar to that observed at low temperature.

Although much has been done related to the thermosalient effect in oxitropium bromide, it seems that the focus has been set on the phase transition itself, while the processes occurring prior to the point of phase transition have not been studied. Moreover, as novel findings realized in the case of *N*'-2-propylidene-4-hydroxybenzohydrazide pointed out to the importance of interplay between thermal expansion and compressibility, following experiments had also to be performed for the oxitropium bromide in the scope of this thesis:

1. Thermal expansion of oxitropium bromide is studied, in detail, by both *in-situ* high-temperature single crystal and powder X-ray diffraction
2. Compressibility of oxitropium bromide is address by DFT calculations
3. Systematic set of thermal and elastic proprieties is collected, and the mutual relationship is investigated in detail
4. Behaviour of low energy phonons, representing joint movements in the crystal lattice, is inspected by the *in-situ* high temperature Raman spectroscopy
5. Finally, the propagation of sound through in oxitropium bromide is studied aiming to determine existence of preferable propagation directions of elastic waves and energy.

Temperature-induced structural changes of oxitropium bromide Form A and Form B were investigated by the *in-situ* X-ray powder diffraction in the temperature range $T$= -45 – 110 °C as shown in Figure 32.

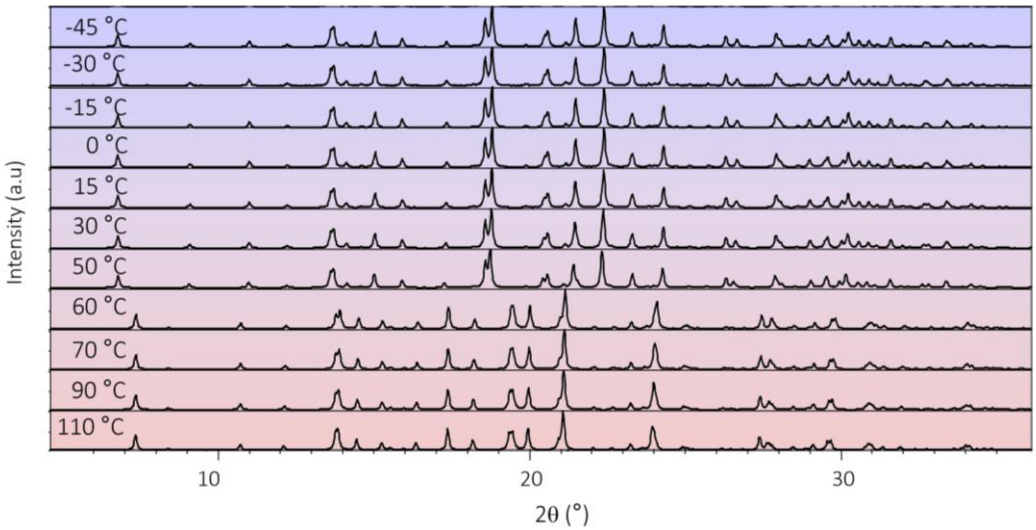



**Figure 32** In-situ high-temperature X-ray powder diffraction data of oxitropium bromide Form A and Form B in the temperature range T=-45 – 110 °C.

It is obvious from the Figure 32 that pronounced structural change caused by the phase transition of oxitropium bromide Form A and Form B occurs in the temperature range 50 – 60 °C. Rietveld structure refinements of oxitropium bromide Form A and Form B at $T$ = 30 °C and $T$ = 60 °C, respectively, are shown in Figure 33. Refinement was carried out by using the split-type pseudo-Voigt profile function and the polynomial background model. Isotropic vibration modes were assumed for all atoms. During the refinement, a zero shift, scale factor, half-width parameters, asymmetry and peak shape parameters were simultaneously refined. The structure of oxitropium bromide Form A, as reported by Bernstein et. al, was used as starting structural model for the Rietveld refinement at $T$ = 30 °C while the structure oxitropium bromide Form B, as reported by Skoko *et al*. [17], was used for the Rietveld refinement of data collected at 60 °C.

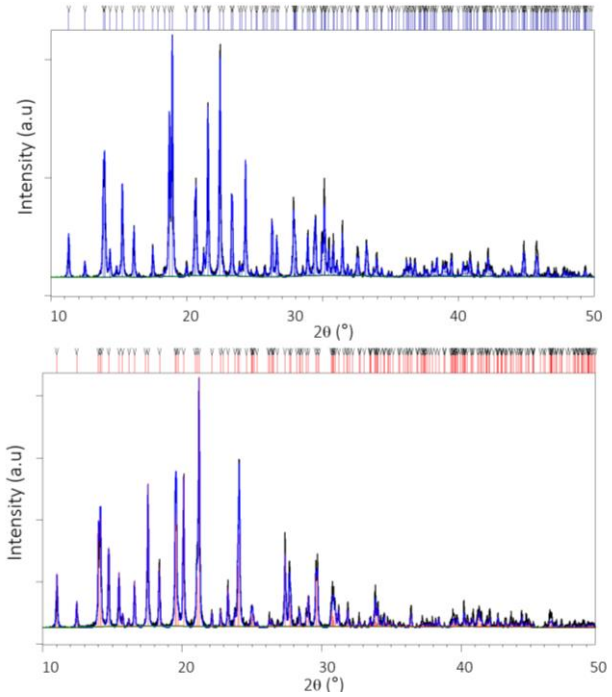



**Figure 33** Rietveld structure refinements of oxitropium bromide 30 °C and 60 °C. Experimental data are given as black line, calculated diffraction pattern as blue line while the dark blue and red vertical lines represent positions of Bragg reflections of oxitropium.

*In-situ* single crystal X-ray diffraction was additionally performed in temperature range $T$ = RT – 138 °C to enable an insight into fine structural changes occurring prior and after the phase transition of oxitropium bromide. Selected crystal was mounted in quartz vials and kept still with the use of quartz wool to avoid mechanical stress on its surfaces, which is a procedure that was performed for the very first time in the world and it greatly helped to preserve the integrity of the crystal during the phase transition. Furthermore, such mounting proved efficient in the study of jumping crystals, as quartz fibres are flexible enough to accommodate crystal movements at the transition and keep the crystal fixed on the sample holder. In this way, we were able to determine thermal behaviour and crystal structure before and after the topotactic thermosalient phase transition. Figure 34 shows the changes of unit-cell parameters of oxitropium bromide Form A and Form B as a function of temperature determined by *in-situ* high-temperature powder X-ray diffraction ($T$ = -45 – 15°C) and *in-situ* high-temperature single crystal X-ray diffraction ($T$ = 24 – 138 °C). Blue and red rectangles denote Form A and B, respectively.

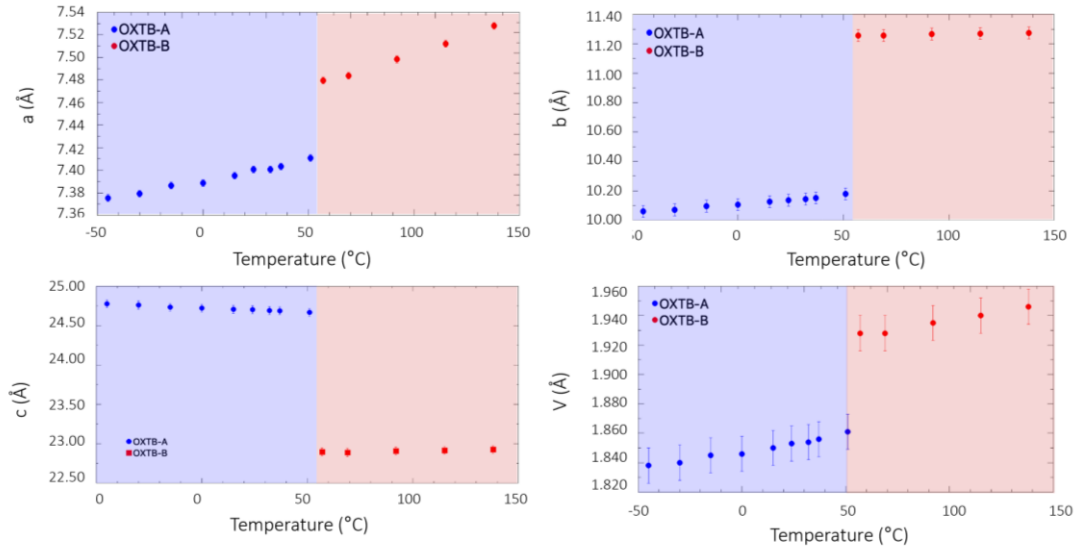



**Figure 34** Unit cell parameters of oxitropium bromide as a function of temperature determined by *in-situ* high-temperature powder X-ray diffraction from -45°C – 15°C and in-situ high-temperature single crystal X-ray diffraction 24°C – 138°C. Blue and red rectangles.

Based on the refined lattice parameters, the thermal expansion coefficients $\alpha$ for oxitropium bromide Form A and Form B along principal axis $i$ = 1, 2 and 3 were calculated and shown in Table 8 and Table 9.

**Table 8** Thermal expansion coefficients αi along principal axis *i* =1, 2 and 3 for oxitropium bromide Form A determined from *in-situ* high-temperature X-ray diffraction

| | | *Component of $x_i$ along the crystallographic axes* | | |
|---|---|---|---|---|
| *Principal axis,* i | $\alpha_i$ ($\times 10^{-6}K^{-1}$) for Form A | *a* | *b* | *c* |
| *1* | 119 (1) | 0 | 1 | 0 |
| *2* | -44 (2) | 0 | 0 | 1 |
| *3* | 48 (2) | 1 | 0 | 0 |

**Table 9** Thermal expansion coefficients αi along principal axis *i* =1, 2 and 3 for oxitropium bromide Form B determined from *in-situ* high-temperature X-ray diffraction

| | | *Component of $x_i$ along the crystallographic axes* | | |
|---|---|---|---|---|
| *Principal axis,* i | $\alpha_i$ ($\times 10^{-6}K^{-1}$) for Form A | *a* | *b* | *c* |
| *1* | 19 (2) | 0 | 0 | 1 |
| *2* | 21 (2) | 0 | 1 | 0 |
| *3* | 81 (3) | -1 | 0 | 0 |

Corresponding thermal expansivity indicatrix for oxitropium bromide Form A and Form B along principal axis $i$ = 1, 2 and 3 are visualized in Figure 35.

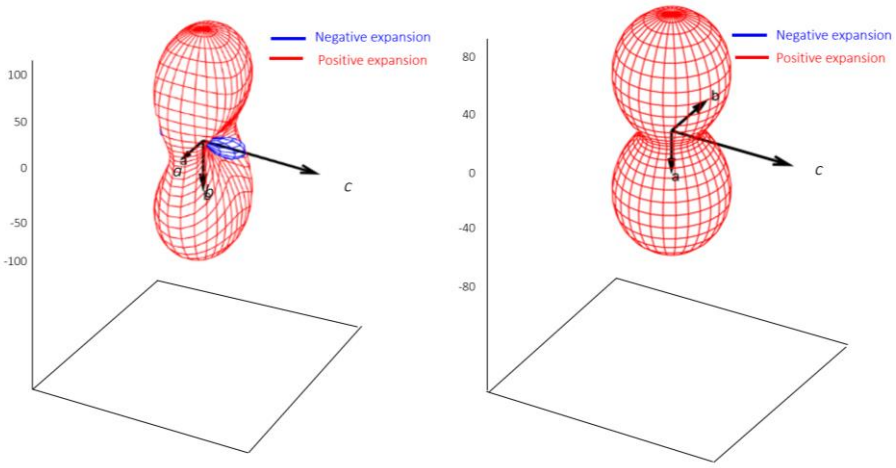



Figure 35 Thermal expansivity indicatrix of oxitropium bromide form A and B determined from in-situ high-temperature single crystal and powder X-ray diffraction.

It is important to highlight that positive thermal expansion coefficients α along crystallographic direction $a$ and $b$ for oxitropium bromide Form A are extremely high. Typically, thermal expansion coefficients for molecular crystals are in the range $0 \times 10^{-6} < \alpha < 20 \times 10^{-6}\ \mathrm{K}^{-1}$, and the values for oxitropium bromide Form A are up to five times larger than the usual maximum value ($\alpha_b = 119 \times 10^{-6}\ K^{-1}$ along the $b$ axis). The thermal expansion in $a$ direction is also quite high and amounts to $\alpha_a = 48 \times 10^{-6}\ K^{-1}$. But the most important realization, found by *in-situ* diffraction experiments, is related to the appearance of negative thermal expansion along crystallographic direction $c$ for oxitropium bromide Form A with the corresponding coefficient of $\alpha_c = -44 \times 10^{-6}\ K^{-1}$. On the contrary, all axes of high temperature form exhibit positive thermal expansion with coefficients given in the Table 9. Also, the values of coefficients of thermal expansion in the high temperature form are much lower than for the low temperature one. Although still high, the coefficients for the $c$ and $b$ axis remain in the usual range for molecular crystals ($\alpha_b = 21 \times 10^{-6}\ K^{-1}$, $\alpha_c = 19 \times 10^{-6}\ K^{-1}$). The thermal expansion in $a$ direction is still extremely high ($\alpha_a = 81 \times 10^{-6}\ K^{-1}$) and almost doubles with respect to the value of the low temperature form.

While diffraction experiments provided us with valuable data regarding the thermally induced structural behaviour of oxitropium bromide, theoretical DFT calculation were additionally conducted to gain the insight into elastic proprieties of oxitropium bromide, such as bulk modulus and compressibilities. In such a way it will be possible to study the anisotropy of this system and to extract the relationship between thermal and elastic properties and

compare it with other thermosalient materials. Elastic constants and elastic compliance constants for oxitropium bromide Form A, calculated according to the procedure as described in section 3.2.7, are represented in Table 10 and Table 11.

**Table 10** Elastic constants Cij for oxitropium bromide Form A

$$C_{ij} = \begin{bmatrix} 300 & 125 & 156 & 0 & 0 & 0 \\ 125 & 271 & 73 & 0 & 0 & 0 \\ 156 & 73 & 438 & 0 & 0 & 0 \\ 0 & 0 & 0 & 177 & 0 & 0 \\ 0 & 0 & 0 & 0 & 127 & 0 \\ 0 & 0 & 0 & 0 & 0 & 114 \end{bmatrix} Kbar$$

**Table 11** Elastic compliance constants Sij for oxitropium bromide Form A

$$S_{ij} = \begin{bmatrix} 4.83 & -1.84 & -1.41 & 0 & 0 & 0 \\ -1.84 & 4.56 & -0.102 & 0 & 0 & 0 \\ -1.41 & -0.102 & 2.80 & 0 & 0 & 0 \\ 0 & 0 & 0 & 5.66 & 0 & 0 \\ 0 & 0 & 0 & 0 & 7.86 & 0 \\ 0 & 0 & 0 & 0 & 0 & 8.77 \end{bmatrix} Mbar^{-1}$$

From elastic compliance constants $S_{ij}$, compressibilities along the principal axis $i$ =1, 2 and 3 were calculated and shown in Table 12.

**Table 12** Principal compressibilities Ki for for oxitropium bromide Forma A along the principal axes *i*=1, 2 and 3 determined from DFT stiffness matrix calculations.

| | | *Component of* $\mathbf{x}_i$ *along the crystallographic axes* | | |
|---|---|---|---|---|
| *Principal axis,* i | $K_i$ (TPa$^{-1}$) for Form A | *a* | *b* | *c* |
| *1* | 15.8 | 1 | 0 | 0 |
| *2* | 26.2 | 0 | 1 | 0 |
| *3* | 12.9 | 0 | 0 | 1 |

Corresponding compressibility indicatrix for oxitropium bromide Form A along principal axis $i$ =1, 2 and 3 is visualized in Figure 36.

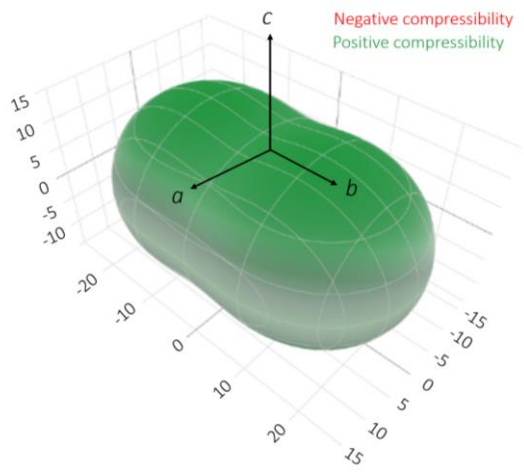



Figure 36 Linear compressibility indicatrix for oxitropium bromide Form A determined from DFT stiffness matrix calculations

DFT calculations, thus, showed that oxitropium bromide Form A exhibits positive compressibility in all three directions, with relatively isotropic change of the unit cell, despite the presence of highly anisotropic thermal expansion, which is negative along the *c*-axis. Unlike in the case of *N*'-2-propylidene-4-hydroxybenzohydrazide, where negative thermal expansion in the *c*-direction was coupled with negative compressibility in *c*-direction, it seems that thermal expansion behaviour of oxitropium, does not arise as a consequence of its elastic properties. In other words, while negative thermal expansion prior to the thermosalient phase transition is, indeed, an important feature shared among *N*'-2-propylidene-4-hydroxybenzohydrazide and oxitropium bromide, negative compressibility does seem to not play a detrimental role for manifestation of jumping effect. As in the case of *N*'-2-propylidene-4-hydroxybenzohydrazide, Grüneisen parameters for oxitropium bromide Form A were calculated from the experimentally determined coefficients of thermal expansion and calculated elastic constants. The values are given in the Table 14.

Table 13 Components of Grüneisen parameters $\gamma_1$, $\gamma_2$ and $\gamma_3$ for oxitropium bromide Form A

| | $\gamma_1$ | $\gamma_2$ | $\gamma_3$ |
|---|---|---|---|
| Form A | 1213 | 1644 | 4910 |

Analysis of oxitropium bromide was also further expanded to Raman spectroscopy in the low frequencies range aiming to provide an insight to soft modes behaviour at different temperatures. Figure 37 shows the *in-situ* high-temperature Raman spectra of oxitropium bromide Form A, recorded at 300 K and Form B, measured at 343 K.

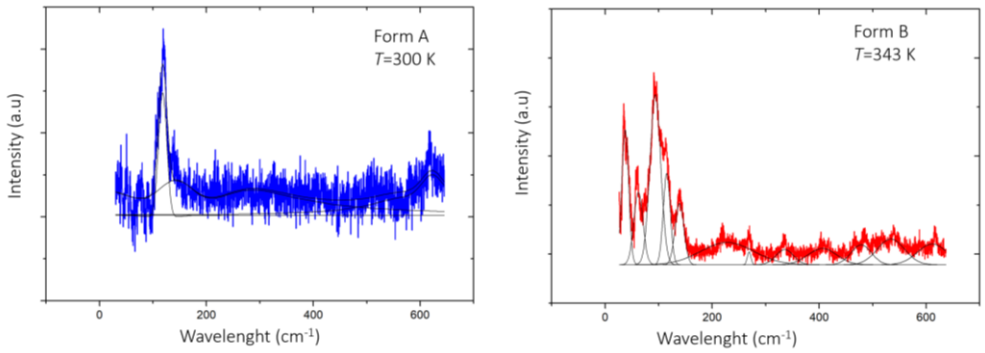



**Figure 37** In-situ high-temperature Raman spectra in low frequencies range of oxitropium bromide Form A and Form B, collected at 300 K and 343 K, respectively.

Peak positions of low frequency Raman modes found in the spectra are listed in Table 15.

**Table 14** In-situ high-tempearture low frequency Raman peaks positions of oxitropium bromide Form A and Form B, obtained by Pseudo-Voigt fitting

| Form A | Form B |
|---|---|
| $\tilde{\nu}$ (cm$^{-1}$) | |
| | 37 |
| | 60 |
| | 94 |
| 118 | 114 |
| 143 | 140 |
| | 222 |
| | 268 |
| | 336 |
| | 466 |
| | 408 |
| | 485 |
| | 535 |
| 623 | 617 |

From Table 12 it can be seen that all modes belonging to oxitropium bromide Phase A are also present in the high temperature Phase B accompanied with a small softening. It is noticeable that Form B is richer in the low frequency modes indicating that the structural changes that occurred during heating, indeed, involve intramolecular dynamics, in particular, regarding the collective motion of molecules in the structure ie. lattice vibrations.

Studies were further expanded to investigation of sound properties in oxitropium bromide Form A using the reported methodology. [63] To inspect how waves are propagating in oxitropium bromide Form A it is convenient to visualize it in a three-dimensional projection. Phase velocity of transversal modes (secondary waves) and longitudinal waves ie. sound (primary waves) for oxitropium bromide Form A is shown in the Figure 38.

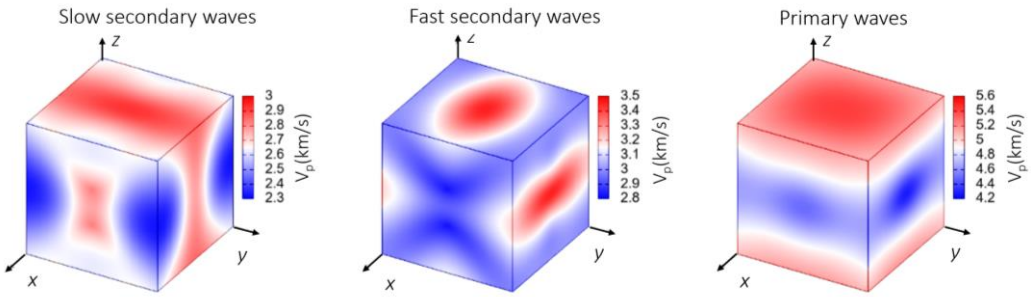



Figure 38 Phase velocity of waves through oxitropium bromide Form A

As can be noticed from Figure 38 phase velocity of the primary mode in oxitropium bromide is faster while the secondary modes are slower. The absolute velocities show that all modes (primary, secondary and slow secondary modes) are fastest in the *z*-direction compared to *x* and *y*, while primary modes are being fastest. Group velocity of sound waves is shown in the Figure 39.

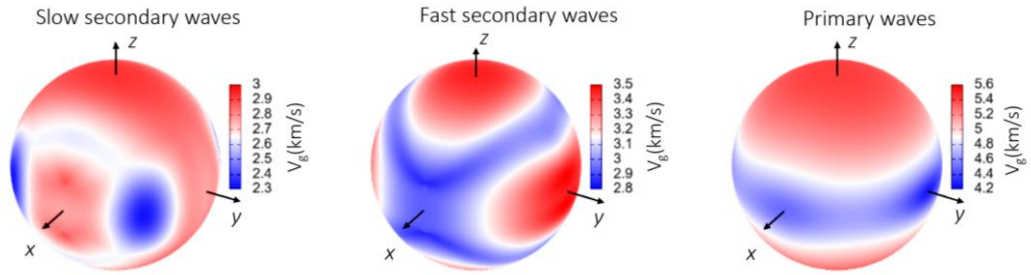



Figure 39 Group velocity of waves through oxitropium bromide Form A

Figure 39. shows that group velocity behaves similar to phase velocity, again pointing out that both primary and secondary waves are fastest in *z*-direction. Enchantment factor of sound waves are showing in Figure 40.

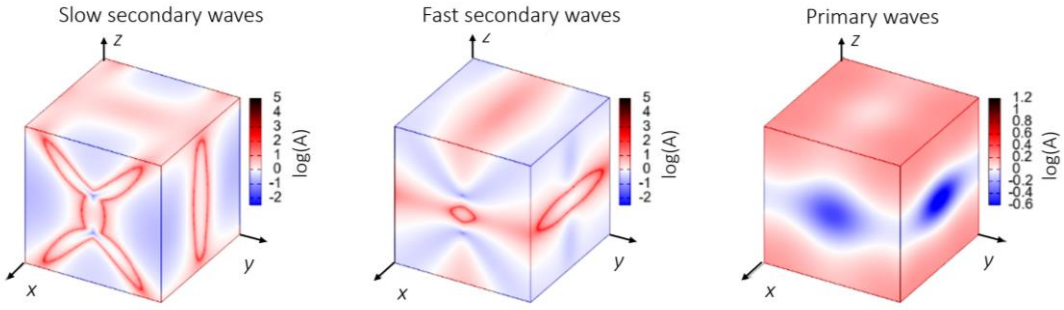



Figure 40 Enchantment factor of waves for oxitropium bromide

Figure 40 shows that secondary modes possess a rich structure, in particular slow secondary modes, exhibiting narrow bands of extremely high enhancement. The primary mode shows

more moderate enhancement, primarily along the *z*-direction faces of cube. Power flows for sound waves for oxitropium bromide are shown in Figure 41.

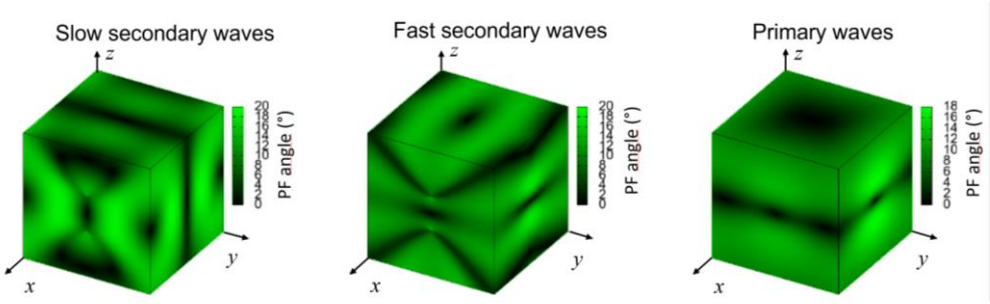



Figure 41 Waves power flow for oxitropium bromide Form A

Figure 41 shows that power flow for primary waves is focused in *z* direction, with almost no divergence, indicating that there is a privileged path for propagation of compressing waves and transfer of the energy. The material in this direction is more flexible and allows the release of accumulated strain energy. Also, speed of the sound waves in Form A of oxitropium bromide are approximately 5 km/s which corresponds to the speed of sound in metals and is much higher than in other molecular solids. This analysis, which shows that perturbation can move in the thermosalient effect very quickly, and that the flow of the energy is focused and not dissipating and involve the low frequency phonons (long wavelength) fully confirms our assumption that thermosalient effect is caused by the cooperative movement of the molecules in crystal, with an extremely energetic and rapid phase transition, with the release of the energy on the time scale of less than a millisecond which, in turn, causes the crystals to jump of the surface.
Main anisotropic index $A^L$ as defined in [62] were calculated with a *Matlab* script for calculating the anisotropy for any material assuming the elastic constants are well known. Values obtained for oxitropium bromide Form A are shown in Table 16.

Table 15 Anisotropy parameters for oxitropium bromide form A calculated from elastic constants

| | Anisotropy parameters | | |
|---|---|---|---|
| | $A^L$ | $A^U$ | $A^C$ |
| Form A | 0.20945 | 0.52453 | 0.045754 |

By comparing the obtained values with the ones found in the literature [62] it is obvious that they are comparable to metals like thallium and platinum, which are the materials with highest anisotropy values.

In summary, once again we observe the existence of negative thermal expansion, however, based on those results, it seems that we do not need to have negative thermal expansion does not need to be coupled with negative compressibility as we originally thought

during the investigation of *N*'-2-propylidene-4-hydroxybenzohydrazide bromide. Negative thermal expansion of oxitropium bromide can be understood if one considers hydrogen bonding network between neighbouring oxitropium molecule as shown in Figure 42.

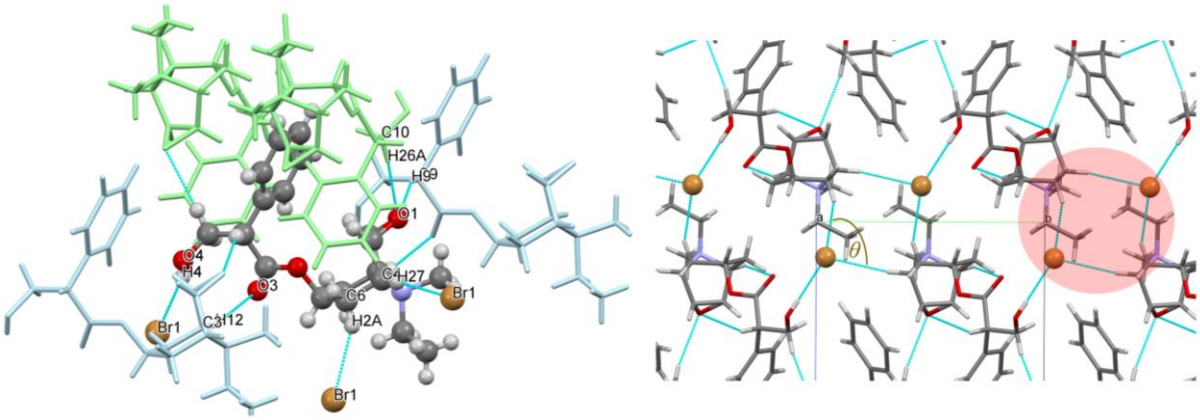



**Figure 42** Crystal packing of oxitropium bromide Form A.

We can observe oxitropium bromide molecules forms two hydrogen bonds that involve oxygen atom O1 from tricyclic ring [O1···H9-C9 and O1···H26-C10], one hydrogen bond that involve carboxylic oxygen atom O3 [O3···H12-C3] and well three hydrogen bonds that involve bromide anion [Br1···H4-O4, Br1···H2A-C6 and Br1···H27-C1]. Among those three H-bonds that include Br anion, the first one that involves hydroxyl oxygen is, as expected, stronger compared to other two. On the right-hand side of the figure, we can observe that hydrogen bonds that involve bromide anion represent an important feature in this crystal packing, forming a flexible double-linked hinge (coloured in red). Considering the extended packing (Figure 43), a *wine-wrack* network of oxitropium bromide can be observed.

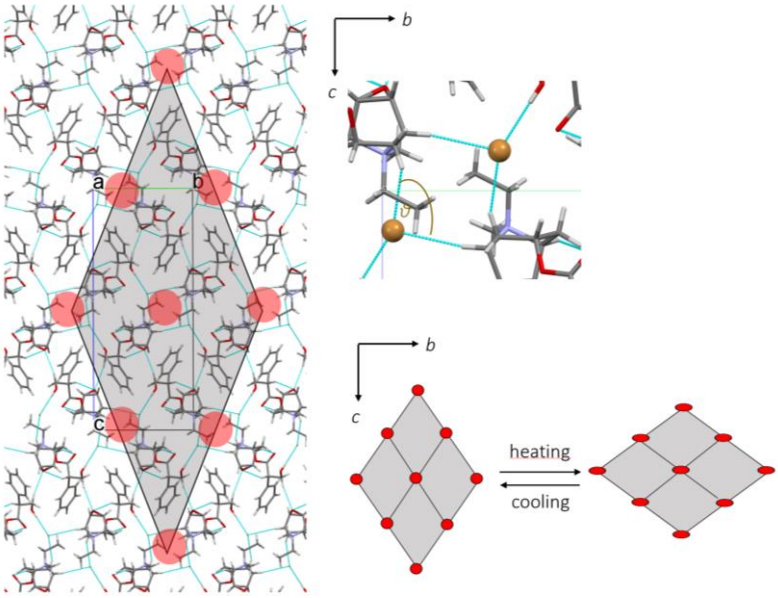



Figure 43 Coupling of orthogonally directed negative expansion with positive expansion for oxitropium bromide Form A

With heating, the hinge angle $\theta$ decreases from 100.88 ° to 98.1 ° that consequently results both the *b*-directed elongation and the shrinkage along *c* axis. Such movement of flexible 'hinges' within the wine-wrack network allows coupling orthogonally directed negative expansion with positive expansion. Results of Raman measurements also suggested that intermolecular changes are occurring during heating, which is in accordance with findings realized by the inspection of wine-wrack network. Sound propagation analysis pointed out that thermosalient phase transition resembles the martensitic one, involving a collective motion of the molecules, along that being extremely brisk and energetic.

## 3. 2. 2. Derivatives of oxitropium bromide

### 3. 2. 2. 1. The case of scopolamine bromide hydrate

As demonstrated in the of case of *N*-2-propylidene-4-hydroxybenzohydrazide, the investigations of derivative compounds are very useful to establish the role and the importance of some specific structural features on the appearance of thermosalient effect. Since the first detailed study, targeted particularly on the elucidation of jumping phenomena, was performed on the oxitropium bromide, it seemed just reasonable to investigate its derivative – scopolamine bromide, and to further investigate how those modifications affect thermosalient behaviour. Figure 44 shows the difference in chemical formula for oxitropium bromide and its derivative scopolamine bromide. The only difference between oxitropium and scopolamine bromide is in the aza-tricyclic part of molecule; in the case of oxitropium bromide, quaternary nitrogen atom has methyl and ethyl group as substituents, while in the case of scopolamine bromide the nitrogen atom bears two methyl groups.

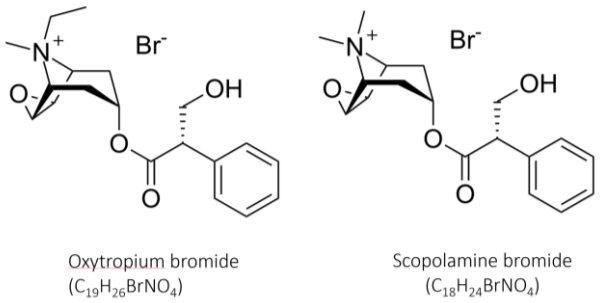



**Figure 44** Chemical structures of oxitropium bromide and scopolamine bromide.

As explained in the introduction, oxitropium bromide belongs to the Class II of thermosalient materials where the existence of the sterically hindered functional groups prevent the formation of the strong hydrogen bonds, however, as it was shown in Section 3.2.1, oxitropium bromide is, nevertheless, capable of formation of wine-wrack 3D network. Despite the fact that 3D network is formed, the fact remains that formed interaction, especially those that involve bromide anion, can be, in general, considered as weak intermolecular interactions. Additionally, since the change on quaternary nitrogen atom most probably will not cause any significant difference in hydrogen bonding network potential, we decided to try to recrystallize scopolamine bromide from several solvents (and their mixtures) in order to prepare solvate/hydrate of scopolamine bromide – a compound that is expected to possess an increased hydrogen bonding potential thus enabling more versatile packing possibilities compared to oxitropium bromide. Scopolamine bromide has been recrystallized from several solvents:

acetone, acetonitrile, dimethyl sulfoxide, ethanol, methanol, chloroform, distilled water, dichloromethane, ether, toluene. It dissolves well in ethanol, dimethyl sulfoxide, methanol and distilled water, while it was either not soluble in other solvents or did not result in solid crystals. Crystals of the best quality were obtained by recrystallization from distilled water; 0.165g of scopolamine bromide (Sigma Aldrich, ≥98% (HPLC), CAS Number 155-41-9) was recrystallized from 4 ml of water. Obtained crystals were large and had well-defined habit. While the crystal structure of scopolamine bromide is thoroughly described by Glaser *et al.* (orthorhombic space group $P2_12_12_1$ at 293 K: $a$ = 7.0403(8), $b$ = 10.926(2), $c$ = 23.364(5) Å, V = 1797.2(6) Å$^3$, $Z$ =4), the structure of its hydrate is novel and unreported. The structure of scopolamine bromide hydrate was solved from single crystal diffraction data at RT and it was found to crystallize in the monoclinic system in the space group $P2_1$ with unit-cell parameters: $a$ = 6.7845 (3) Å, $b$ = 11.0047 (4) Å, $c$ = 12.6710 (5) Å. Figure 45 shows the crystal structure of scopolamine bromide hydrate; the lattice contains two scopolamine cations, two bromide anions and two water molecules.

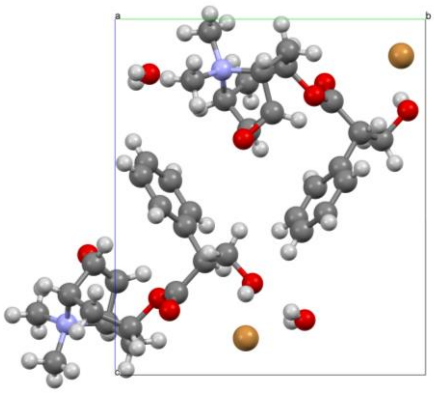


Figure 45 Crystal structure of scopolamine bromide hydrate

Crystal packing of scopolamine bromide hydrate can be described as 2D layers in *bc* plane formed by hydrogen bonding network as shown in Figure 46.

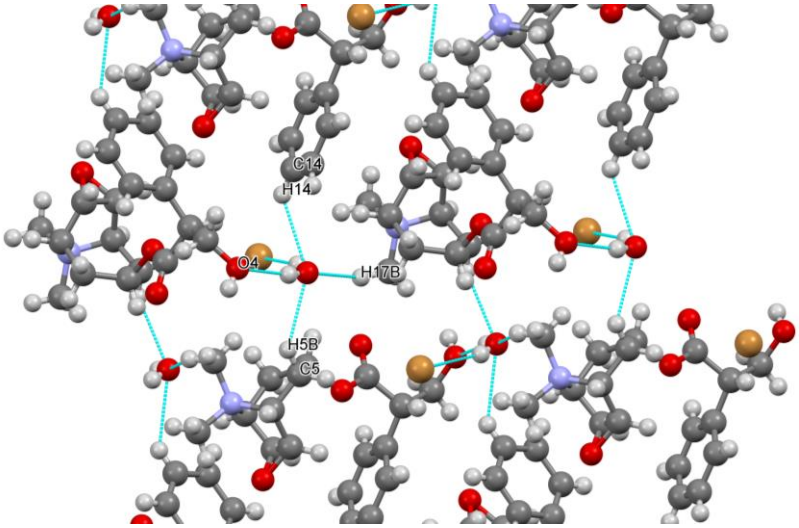



Figure 46 2D layers in *bc* plane formed by hydrogen bond network involving water molecule.

Water molecule is surrounded by four scopolamine molecules; oxygen atom from water molecule acts as a hydrogen acceptor towards CH groups from three neighbouring scopolamine molecules [C14-H4···O5W, C5-H5B···O5W and C17-H17B···O5W] as well as hydrogen atom donor towards hydroxyl oxygen atom from fourth scopolamine molecule [O5W-H5···O4].

Thermosalient behaviour of scopolamine bromide hydrate was investigated by the hot-stage microscopy during heating run in the temperature range from $T$=25-100 °C at a constant rate of 10°C/min. During heating, crystals of scopolamine bromide hydrate start to jump at $T$= 45°C and the jumping proceeds up to 65°C with a nearly constant frequency. While ~ 80% of all the crystals jump off the stage, similar to other TS compound, the difference is observed related to the temperature interval during which the crystals jump – crystals are exhibiting thermosalient behaviour in the temperature interval of almost 20°C, whereas typically the jumping of crystals occurs in the narrow time window of several degrees in the vicinity of the temperature of phase transition (certainly not more than 5°C). Also, it has been noted that SMB-W crystals are jumping only during the heating run and not during cooling. Figure 47 shows hot stage microscopy image of scopolamine bromide hydrate crystals, before heating (left) and after heating (right).

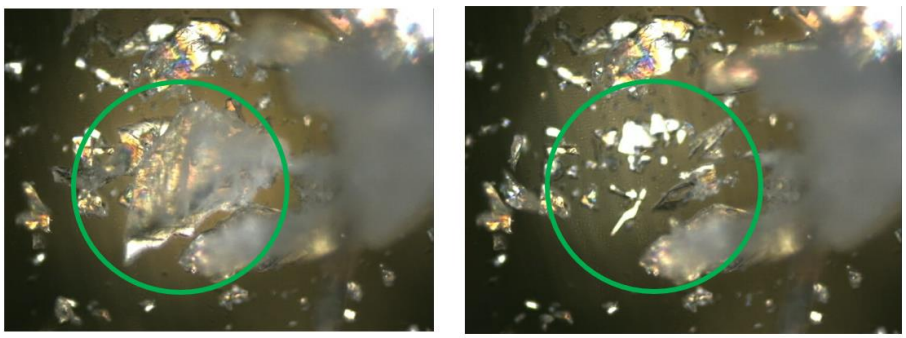


Figure 47 Hot stage microscopy image of scopolamine bromide hydrate crystals, before heating (left) and after heating (right).

On further examination, the heating rate was changed to verify the dependence of crystal jumps on the heating rate. Heating rate was increased to 20 °C/min and it was observed that crystals jumps were a little more energetic and the temperature interval during which the crystals jump is reduced. Additional experiments were performed in the following way: sample was quickly heated from RT to 40° with the rate of 150°C/min and kept at it for 30 minutes. The same procedure was repeated for temperatures of 50, 60 and 80°C. It was observed that the time interval during which crystals jump decreases with the increase of the temperature at which the crystals were held. If the sample was kept at a constant temperature of 40°C crystals jumped for almost 15 minutes, while at 60°C time during which the crystals were observed to jump were reduced to less of 5 minutes. An important aspect is that by increasing the rate of heating the temperatures interval during which the crystals jump get shorter. Since this kind of dependence is usually related to phenomena of absorption or desorption of gas from a material it was checked if there is a release of solvent from scopolamine bromide hydrate. Hot stage analysis was performed with a larger crystal of scopolamine bromide hydrate immersed in oil (P3-oil for rotary vacuum pumps) to check for the possible release of solvent (Figure 48).

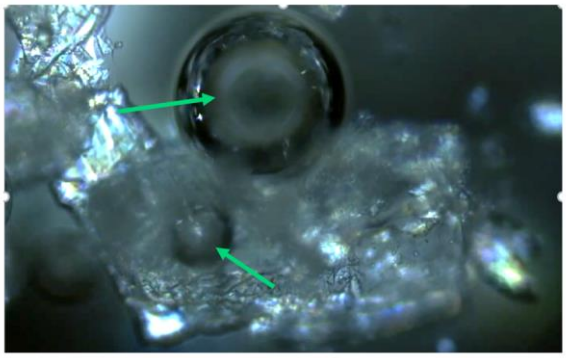


Figure 48 Scopolamine bromide hydrate crystal immersed in oil under heating on hot stage microscope.

During heating from RT to 100°C, with a heating rate of 10°C/min, starting at around 50°C the bubbles exiting the surface of the crystal were clearly visible. This confirmed the assumption that the water molecules is in fact, released from the crystal during heating.

Temperature-induced structural changes of scopolamine bromide hydrate were investigated by *in-situ* X-ray powder diffraction in the temperature range $T$ = 25-75 °C (Figure 49).

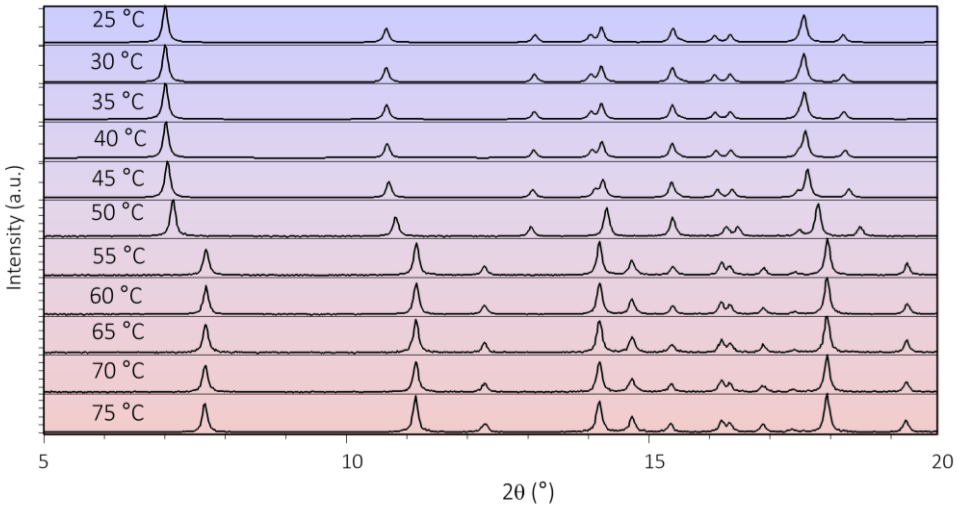



Figure 49 In-situ high-temperature X-ray powder diffraction data of scopolamine bromide hydrate in the temperature range T=25-75 °C.

It is obvious from the Figure 49 that pronounced structural change occurs in the range 50-55°C. Rietveld refinements of scopolamine bromide hydrate and scopolamine bromide at 25 °C and 70 °C, respectively, are shown in Figure 50. Refinement was carried out by using the split-type pseudo-Voigt profile function and the polynomial background model. Isotropic vibration modes were assumed for all atoms. During the refinement, a zero shift, scale factor, half-width parameters, asymmetry and peak shape parameters were simultaneously refined.

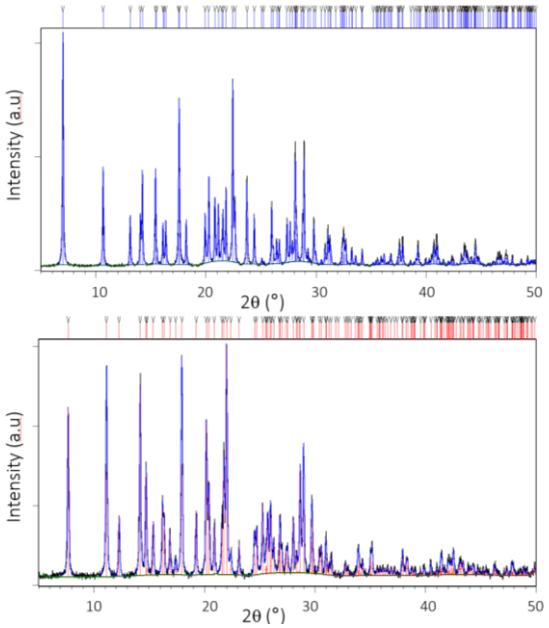



**Figure 50** Rietveld structure refinements of scopolamine bromide hydrate 25 °C and 70 °C. Experimental data are given as black line, calculated diffraction pattern as blue line while the dark blue and red vertical lines represent positions of Bragg reflections of scopolamine bromide hydrate and scopolamine bromide, respectively.

The structure of scopolamine bromide hydrate, as determined by single crystal data, was used as starting structural model for the Rietveld refinement at *T*=25 °C while the structure of scopolamine bromide, as reported by Glaser, was used for the Rietveld refinement of data collected at 70 °C. At this point, it become evident that scopolamine bromide hydrate does not exhibit phase transition, yet it undergoes dehydration as suggested based on hot-stage microscopy experiments.

*In-situ* single crystal X-ray diffraction was performed in temperature range *T*=25-75 °C in order to precisely determine the temperature-induced structural changes occurring during the dehydration. Careful examination of refined structures revealed that the occupancy of oxygen atom (O5) is changing as a function of temperature during heating (red dots) and during consequent colling run (blue square) as shown in Figure 51.

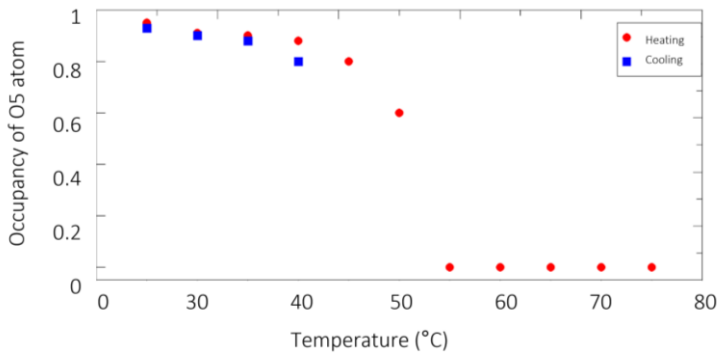



**Figure 51** Occupancy of oxygen atom (O5) from water molecules as a function of temperature determined by *in-situ* high-temperature single crystal X-ray diffraction.

Figure 51 shows that occupancy of oxygen atom (O5) from water molecules slowly decreased from 0.95 (at RT) to 0.5 (at *T*=50°C) and finally diminishes at *T*=55°C (Figure 51) when hydrate completely transformed to its anhydrous form. Such continuous dehydration process is certainly not a typical feature; often water or solvent molecule is expelled from crystal in a quite narrow temperature range. It is particularly interesting to notice that the dehydration is, in fact, a reversible process; it was found that water molecules can easily enter and incorporate itself in scopolamine lattice during cooling as evidenced by increase in occupancy of O5 atoms from 0.80 (at *T*=40 °C) to 0.93 (at RT). In many materials, such reversible process is often not possible since structural rearrangements that occur upon the expel of solvent molecules lead to the formation of denser packing motives that are often unable to accommodate subsequent insertion of water molecules. In order to confirm that dehydration is truly such a continuous process a thermogravimetric analysis (TGA) was performed. Additionally, TGA was used to confirm whether water uptake indeed occurs during cooling run. Figure 52 shows the weight loss of scopolamine bromide hydrate as a function of temperature during heating run (red curve) and weight gain during cooling run (blue curve).

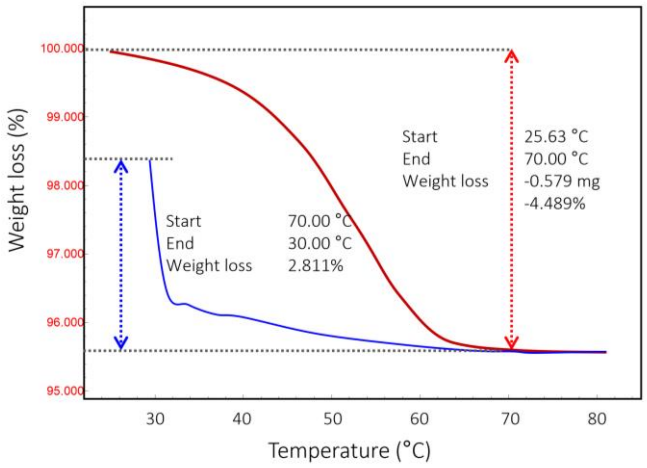



*Figure 52 Weight loss of scopolamine bromide hydrate as a function of temperature during heating run (red curve) and weight gain during cooling run (blue curve).*

Considering the molecular weight of scopolamine bromide hydrate ($C_{18}H_{24}NO_4 \cdot Br \cdot H_2O$) = 434,33 g/mol) and molecular weight of water ($H_2O$) = 18,02 g/mol, a weight loss of 4.15% is expected during the release of one water molecule from the sample. Due to the adsorbed moisture on the surface of the sample, thermogravimetric analysis yielded a somewhat larger weight loss (4.48%) but nevertheless TGA confirmed that the release of one water molecules from scopolamine bromide hydrate, indeed, occurs in the wide temperature (from RT up to ~ 70 °C). Uptake of water molecule, as initially found by single crystal diffraction data collected

during the cooling run, has also been confirmed by TGA. It must be noted that due to experimental TGA setup which does not have a possibility to perform controlled cooling, the full weight gain was not realized during cooling run. Additional obstacle, that might also play a role in not achieving a full weight gain, is related to the fact that measurement was conducted in quite strong flux of synthetic air.

Prior to for further discussion, it is important to highlight that dehydration process is, of course, accompanied with change in chemical composition which means that the changes of lattice parameters and thermal expansion correspond, in fact, to the scopolamine bromide (1-*x*)hydrate, where *x*=0 at RT and 1 at 55 °C. Changes of the unit-cell parameters that accompany the dehydration process are shown in Figures 53.

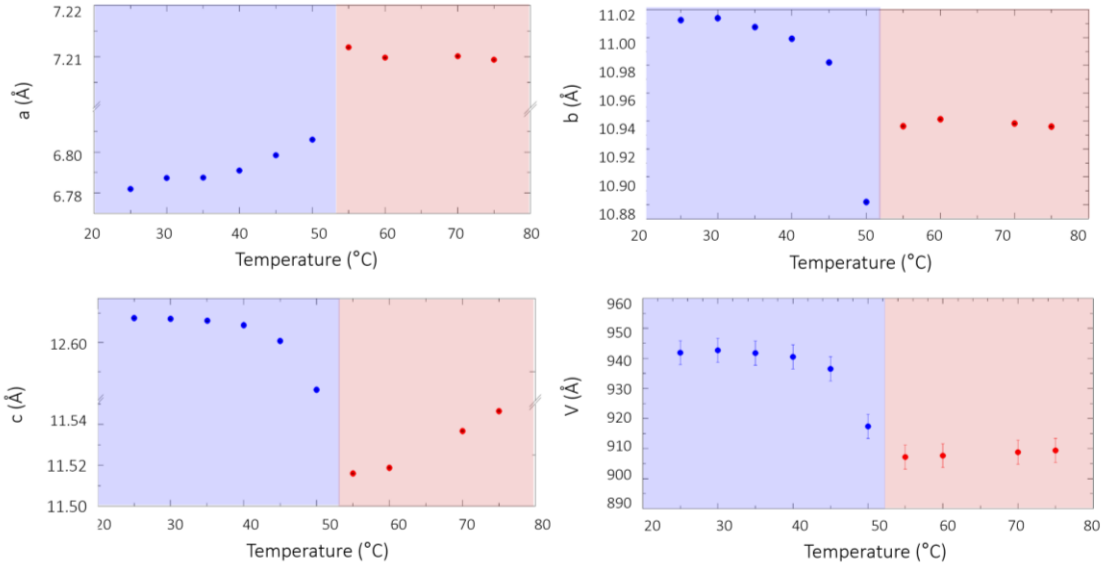



**Figure 53** Unit cell parameters of scopolamine bromide (1-x)hydrate as a function of temperature determined by in-situ high-temperature single crystal X-ray diffraction. Blue and red rectangles denote hydrate and anhydrous form, respectively.

Figure 53 shows that *b* and *c* axes slowly decrease ($\Delta b$= -1%, $\Delta c$= -2%) while *a* axis is increasing ($\Delta a$= 0.5%) as the dehydration process of scopolamine bromide hydrate proceeds from RT to *T*= 55 ° C. With further increase in temperature, more dramatic difference can be observed; in the vicinity of the final dehydration step (between the *T*=50 °C and 60 °C) abrupt decrease of *c* axis ($\Delta c$= -7%) is accompanied with the pronounced increase of *a* axis ($\Delta c$= 6%). Such changes in lattice parameters are caused by the temperature-induced expel of water molecule as shown in the crystal packing of scopolamine bromide hydrate and its anhydrous form (Figure 54).

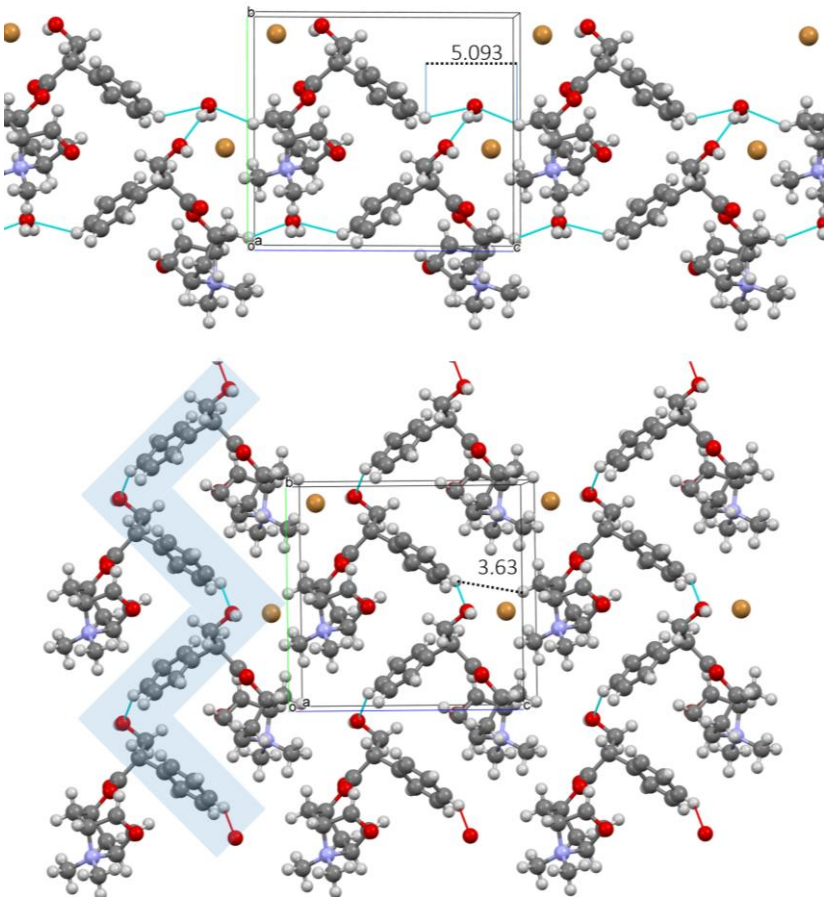



Figure 54 Crystal packing of scopolamine bromide hydrate and its anhydrous form in *bc* plane.

Once water molecule is expelled from the structure a pronounced difference in crystal packing is observed; anhydrous form does not contain 2D layer packing motive as found in the case of hydrate. The crystal packing of anhydrous scopolamine bromide can be described by the isolated tapes in *bc* plane formed between CH group of scopolamine molecule and hydroxyl oxygen from neighbouring molecule [C14-H14···O4]. From Figure 54 it is obvious that in such a crystal packing a neighbouring scopolamine molecule move closer, in particular along the *c* direction, once water molecule is not present; the distance between H14 and H5B decreases from ~ 5.1 Å to 3.6 Å.

To summarize, scopolamine methyl bromide recrystallized from water exhibits thermosalient behaviour with some similarities to other thermosalient systems, but also with striking differences. Even though in all the systems thermosalient effect is caused by the structural changes brought on by thermal treatment, in the case of scopolamine bromide hydrate, this change is not caused by the polymorphic phase transitions (like in the case of N'-2-propylidene-4-hydroxybenzohydrazide and oxitropium bromide) but rather by the expulsion of the solvent molecule (water) from the crystal lattice. Dehydration is a continuous process, and it explains

longer temperature intervals during which crystals jump. Whereas in the case of N'-2-propylidene-4-hydroxybenzohydrazide and oxitropium bromide this interval is about 5°C, this interval can be up to 20 °C for scopolamine bromide hydrate and scopolamine bromide. Nevertheless, it is important to highlight that scopolamine bromide hydrate do share one exotic feature common to almost all thermosalient materials under study: prior to crystal jumps scopolamine bromide hydrate and as well as scopolamine bromide, exhibits negative thermal expansion (in this case negative thermal expansion is biaxial, along *b* and *c* axis).

### 3. 2. 2. 2. The case of scopolamine bromide

As described in Section 3.2.2.1, scopolamine bromide, compared to oxitropium bromide, differs only in quaternary nitrogen atom substituents; while oxitropium contains methyl and ethyl group, in the case of scopolamine bromide the nitrogen atom bears two methyl groups. As explained before, this change on quaternary nitrogen atom is too small to cause any significant difference in hydrogen bonding network potential, thus attempts to prepare the hydrate of scopolamine bromide by the recrystallisation were conducted. Truth be told, we had no particular reason to study scopolamine bromide, besides pure curiosity. As the result will show, that proved to be a good idea.

Thermosalient behaviour of scopolamine bromide was investigated by hot-stage microscopy. During the first heating run, crystals started jumping at ~ 50 °C and crystals continued to experience jumping up to 67 °C. Not all the crystals jumped during heating run, but approximately 50% did. During the cooling run, crystals jumped again, but with a temperature hysteresis - starting at the temperature of ~ 40° K and finishing at around 30°C. During the second heating run, several crystals jumped again at the same temperature as during the first heating, but the number of crystals jumping was much smaller compared to the first heating. Hot-stage experiments were performed many times with different parameters. This included heating/cooling rate (10 to 50 °C/min), number of cooling runs (up to five), crystals monitored for jumping when heating/cooling was stopped at selected temperatures (50 °C, 60 °C, and 70 °C), number of crystals, different crystal sizes, and crystal orientation.

Several features were observed:

1. Jumping (in terms of number of crystals that jumped, their frequency, or strength of the jumps) does not depend on the heating/cooling rate.
2. Jumping does not depend on the size, shape nor the orientation of the crystals in respect to heating stage. As expected, jumps of the smaller crystals were more

forceful, whereas the more massive crystals would only slightly move or turn over to another facet.

3. The number of crystals that jumped decreased drastically with consecutive heating/cooling runs. For example, if 10 crystals jumped during the first heating run, only 2–3 would jump in the second heating run.
4. Crystals continued to jump sporadically when temperature was maintained for some time within the jumping temperature interval between 50 and 60°C. Time period of jumping depended on the temperature. At 323 K, crystals continued to jump for 10 minutes, whereas the jumps ceased after 1–2 minutes at 343 K.
5. No breaking or cracking of the crystals were observed during the jumping.

Overall, the jumps of scopolamine bromide crystals were less energetic compared to the crystals of oxitropium bromide. Figure 55 shows crystals of scopolamine bromide before jumping (left panel, taken during heating at the temperature of 42 °C) and after jumping (right panel, taken during heating at the temperature of 72 °C).

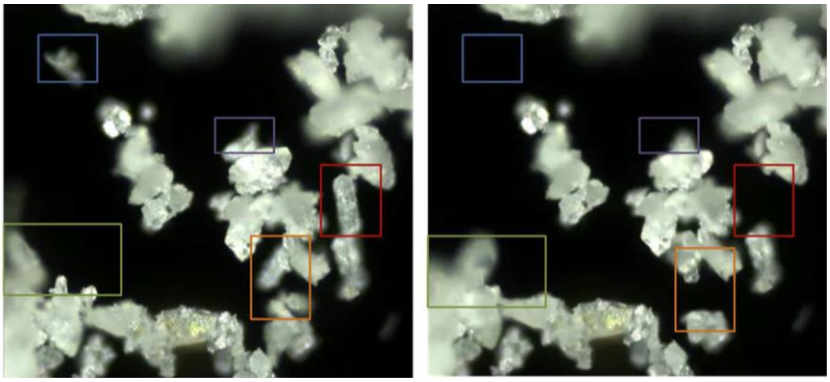


**Figure 55** Crystals of scopolamine bromide before jumping (left panel) and after jumping (right panel).

Crystals that exhibited mechanical motion are marked with blue, green, orange, red, and purple rectangles. Red, blue and orange rectangles mark crystals that jumped off the hot-stage. The green rectangle shows a large crystal that flipped to the other side but remained in more or less the same position. The purple rectangle denotes a crystal that rotated around its axis but was held at the same place by the larger crystal on top of it.

Based on the knowledge accumulated on vast number of thermosalient materials, differential scanning calorimetry was performed to determine the temperature of phase transitions of scopolamine bromide. Differential scanning calorimetry in the temperature interval $T$ = 30-280 °C is shown in Figure 56.

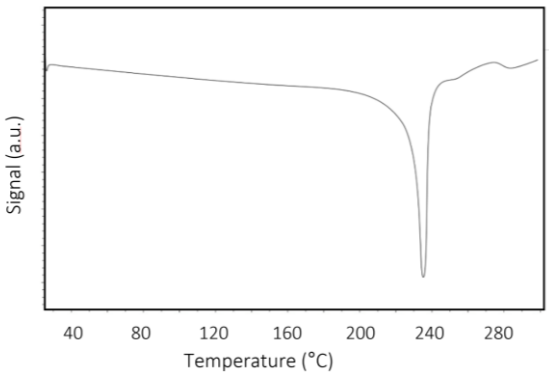



Figure 56 Differential scanning calorimetry of scopolamine bromide.

Much to our surprise, as can be seen from Figure 56, no maxima corresponding to phase transitions were observed before the melting point ~ 230 °C.

Temperature-induced structural changes of scopolamine bromide were investigated by the *in-situ* X-ray powder diffraction in the temperature range $T$ = 35 – 185 °C as shown in Figure 57.

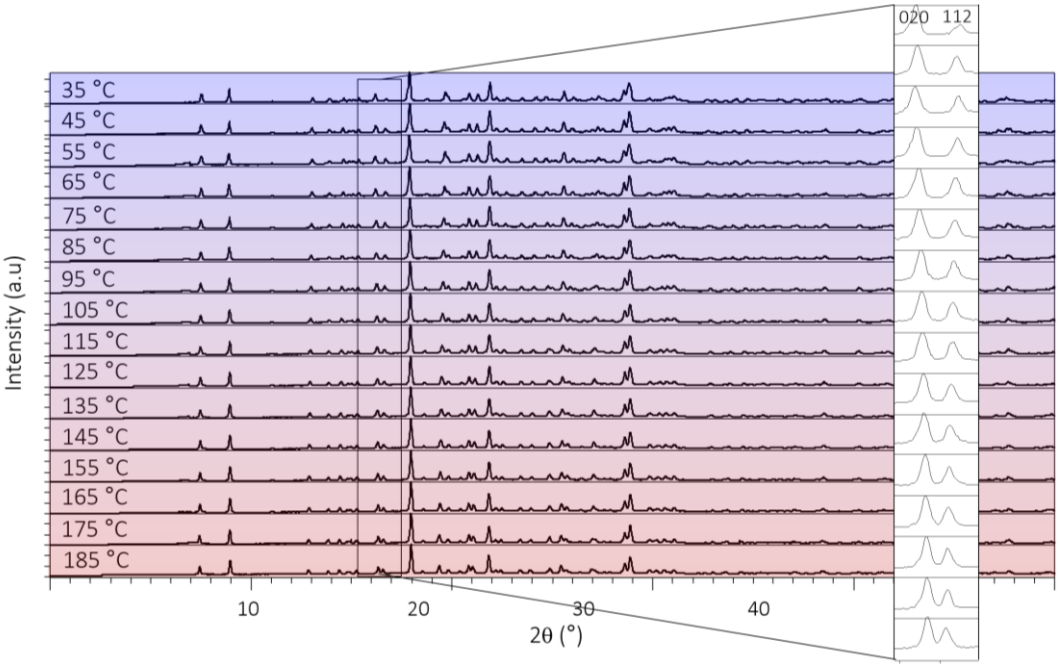



Figure 57 In-situ high-temperature X-ray powder diffraction data of scopolamine bromide in the temperature range T= 35-185 °C.

Careful examination of powder diffraction data collected as a function of temperature (prior to any calculations) revealed quite pronounced shift in diffraction lines. Depending on the *hkl* index, diffraction lines shifted towards a lower or a higher $2\theta$ angle; this was the first indication that scopolamine bromide is characterized by anisotropic thermal expansion. This is best illustrated in the narrow $2\theta$ range between 16° and 17° shown in Figure 57; the diffraction line 020 shifted to higher values of $2\theta$ angle with the increase in temperature, while the diffraction

line 112 shifted towards lower angles, indicating that the unit cell of scopolamine bromide decreased in *b*-direction and expanded in *c*-direction during heating. The shift of the 112 line was greater compared to the 020, suggesting that the absolute value of the thermal expansion coefficient along the *c* axis was larger than along the *b* axis. Rietveld structure refinements of scopolamine bromide at $T$ = 34 °C and $T$ = 175 °C, respectively, are shown in Figure 58. Refinement was carried out by using the split-type pseudo-Voigt profile function and the polynomial background model. Isotropic vibration modes were assumed for all atoms. During the refinement, a zero shift, scale factor, half-width parameters, asymmetry and peak shape parameters were simultaneously refined. Refinements were carried out starting from the structural model of Glaser (ref).

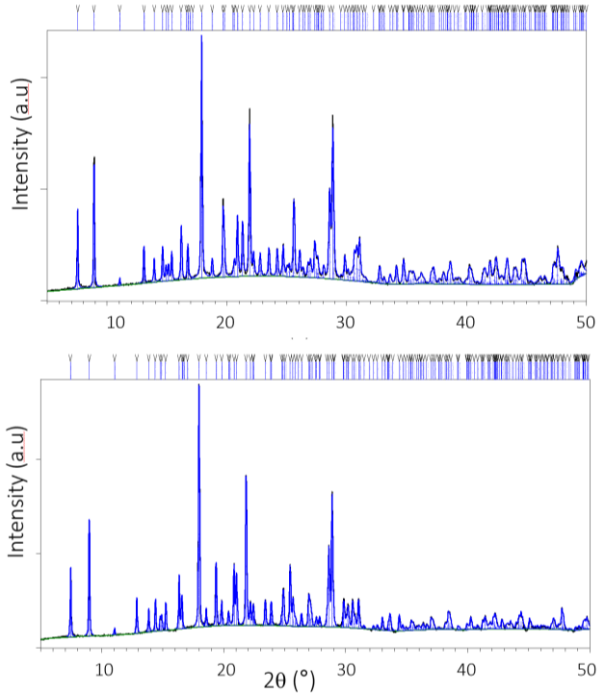



Figure 58 Rietveld structure refinements of scopolamine bromide hydrate 307 K °C and 447 K. Experimental data are given as black line, calculated diffraction pattern as blue line while the dark blue vertical lines represent positions of Bragg reflections of scopolamine bromide.

*In-situ* single crystal X-ray diffraction experiments were additionally carried out to enable an insight into thermally induced fine structural changes. Figure 59 shows the changes of unit-cell parameters of scopolamine bromide as a function of temperature determined by *in-situ* high-temperature single crystal X-ray diffraction in temperature range $T$= 20 -150 °C.

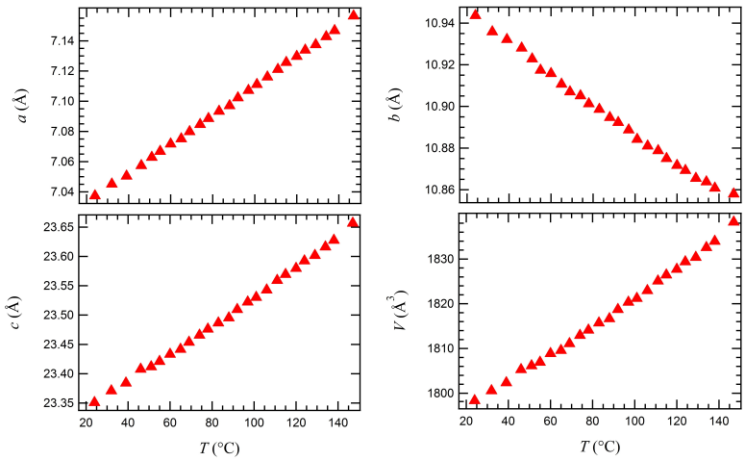



**Figure 59** Unit cell parameters of scopolamine bromide as a function of temperature determined by in-situ high-temperature single crystal X-ray diffraction T= 20 -150 °C.

As the discontinuity in the lattice parameters is not observed even based on measurements in a single crystal, it can be safely stated that the test sample scopolamine bromide does not undergo phase transformation during heating. Based on the lattice parameters, the thermal expansion coefficients $\alpha_i$ for scopolamine bromide along principal axis $i$ = 1, 2 and 3 were calculated and shown in Table 16. For systems of orthorhombic symmetry or higher, such as scopolamine bromide, the principal and (conventional) crystallographic axes coincide. [86]

**Table 16** Thermal expansion coefficients αi along principal axis i=1, 2 and 3 for oxitropium bromide Form A determined from in-situ high-temperature X-ray diffraction.

| | | Component of $\mathbf{x}_i$ along the crystallographic axes | | |
|---|---|---|---|---|
| Principal axis, *i* | $\alpha_i$ $(10^{-6}\mathrm{K}^{-1})$ | *a* | *b* | *c* |
| 1 | -65 (2) | 0 | 1 | 0 |
| 2 | 106 (2) | 0 | 0 | 1 |
| 3 | 138 (3) | 1 | 0 | 0 |

Corresponding thermal expansivity indicatrix for scopolamine bromide along principal axis *i*=1, 2 and 3 are visualized in Figure 60.

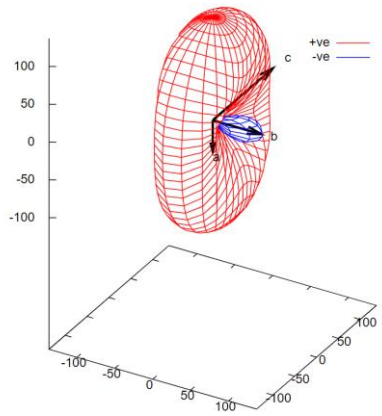



**Figure 60** Thermal expansivity indicatrix of scopolamine bromide determined from in-situ high-temperature single crystal X-ray diffraction.

It is obvious from the Figure 60, that scopolamine positive expansion along *a* and *c* direction and negative thermal expansion along the *b* axis. Scopolamine bromide exhibits six times higher values of positive expansion (along *a* and *c* axis) compared to the typical maximum values for molecular solid (of up to $20\times10^{-6}$ $K^{-1}$) and two times higher values for the negative expansion (along *b* axis). Such a behaviour can be understood if we consider hydrogen bonding network between neighbouring scopolamine molecules as shown in Figure 61.

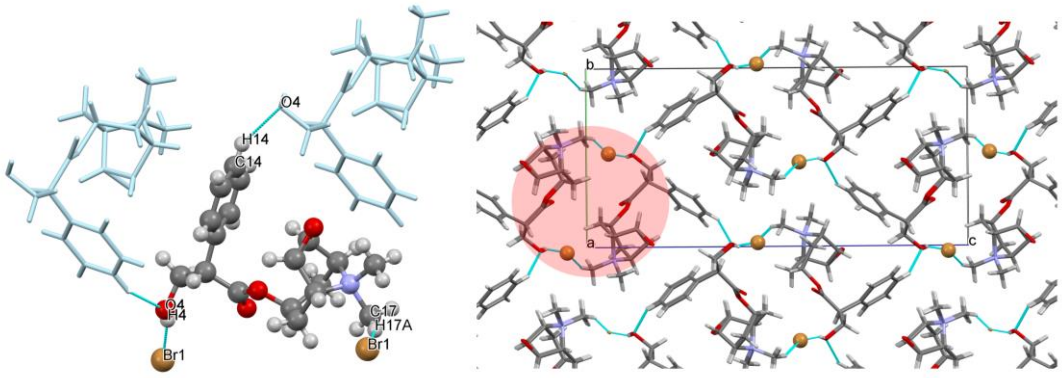



Figure 61 Crystal packing of scopolamine bromide.

We can observe scopolamine bromide molecules form hydrogen bonds that involve oxygen atom O4 from hydroxylic group [O4···H14-C14] and well as two hydrogen bonds that involve bromide anion [Br1···H4-O4 and Br1···H17A-C17]. Among those three H-bonds that include Br anion, the first one that involves hydroxyl oxygen is, as expected, stronger compared to the other. On the left-hand side of the figure, we can observe that hydrogen bonds that involve bromide anion represent an important feature in this crystal packing, forming a flexible double-linked hinge (coloured in red). Considering the extended packing (Figure 62), a *wine-wrack* network of scopolamine bromide can be observed.

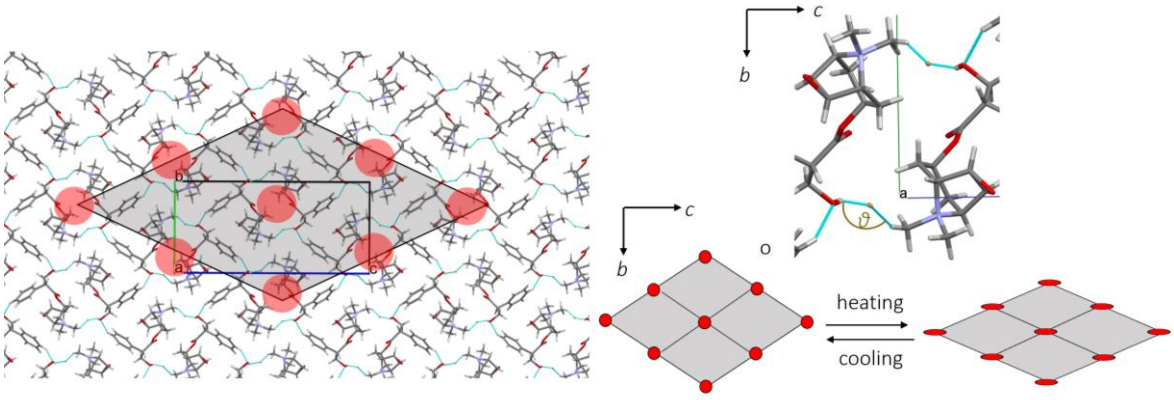



Figure 62 Coupling of orthogonally directed negative expansion with positive expansion for scopolamine bromide

With heating, the hinge angle $\theta$ decreases from 117.1 ° to 115.99 °, that consequently results in both the *b*-directed elongation and the shrinkage along *c* axis. Such movement of flexible 'hinges' within the wine-wrack network allows coupling of the orthogonally directed negative expansion with positive expansion as well as orthogonally directed negative compressibility with positive linear compressibility.

Bulk modulus and compressibility of scopolamine bromide was additionally addressed by DFT calculations. Elastic constants and elastic compliance constants for scopolamine bromide calculated according to the procedure as described in section 3.2.7, are represented in Table 17 and Table 18.

**Table 17** Elastic constants Cij for scopolamine bromide

$$S_{ij} = \begin{bmatrix} 335 & 45.3 & 57.1 & 0 & 0 & 0 \\ 45.3 & 213 & 67 & 0 & 0 & 0 \\ 57.1 & 67 & 240 & 0 & 0 & 0 \\ 0 & 0 & 0 & 117 & 0 & 0 \\ 0 & 0 & 0 & 0 & 128 & 0 \\ 0 & 0 & 0 & 0 & 0 & 107 \end{bmatrix} Kbar$$

**Table 18** Elastic compliance constants Sij for scopolamine bromide

$$S_{ij} = \begin{bmatrix} 0.00315 & -0.000478 & -0.000617 & 0 & 0 & 0 \\ -0.000478 & 0.00521 & -0.00134 & 0 & 0 & 0 \\ -0.000617 & -0.00134 & 0.00468 & 0 & 0 & 0 \\ 0 & 0 & 0 & 0.0085 & 0 & 0 \\ 0 & 0 & 0 & 0 & 0.0078 & 0 \\ 0 & 0 & 0 & 0 & 0 & 0.0093 \end{bmatrix} Mbar^{-1}$$

From calculated elastic coefficients, compressibilities along the along principal axis $i$ = 1, 2 and 3 were calculated and shown in Table 20.

**Table 19** Principal compressibilities Ki for for scopolamine bromide along the principal axes i=1, 2 and 3 determined from DFT stiffness matrix calculations.

| | | Component of $\mathbf{x}_i$ along the crystallographic axes | | |
|---|---|---|---|---|
| Principal axis, *i* | $K_i$ (TPa$^{-1}$) | *a* | *b* | *c* |
| 1 | 2.06 | 1 | 0 | 0 |
| 2 | 3.40 | 0 | 1 | 0 |
| 3 | 2.73 | 0 | 0 | 1 |

Corresponding compressibility indicatrix for scopolamine bromide along principal axis *i*=1, 2 and 3 is visualized in Figure 63.

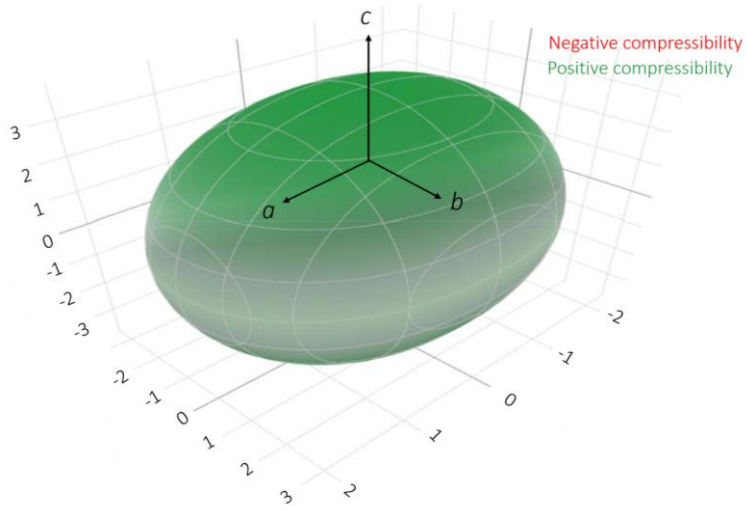



Figure 63 Linear compressibility indicatrix for scopolamine bromide determined from DFT stiffness matrix calculations.

Similar to *N*'-2-propylidene-4-hydroxybenzohydrazide, Grüneisen parameters for scopolamine bromide calculated using experimental data for thermal expansion and compressibility. Obtained values are given in the Table 21.

Table 20 Components of Grüneisen parameters $\gamma_1$, $\gamma_2$ and $\gamma_3$ for scopolamine bromide

| | $\gamma_1$ | $\gamma_2$ | $\gamma_3$ |
|---|---|---|---|
| Scopolamine bromide | -9093.4 | 28879.5 | 36510.5 |

In order to check the compressibility as calculated from DFT, the *in-situ* high-pressure single crystal X-ray diffraction were performed on scopolamine bromide. A high-pressure experiment were performed in a modified Merrill–Bassett diamond anvil cell (DAC). A single crystal was mounted inside the DAC chamber and Daphne oil was used as the pressure-transmitting medium. Pressure was calibrated with a Photon Control spectrometer by the ruby-fluorescence method with a precision of 0.03 GPa. High pressure single-crystal X-ray diffraction data were measured with a four-circle KUMA X-ray diffractometer with graphite monochromate Mo *K*α radiation. Lattice parameters of scopolamine bromide as a function of pressure are shown on Figure 64.

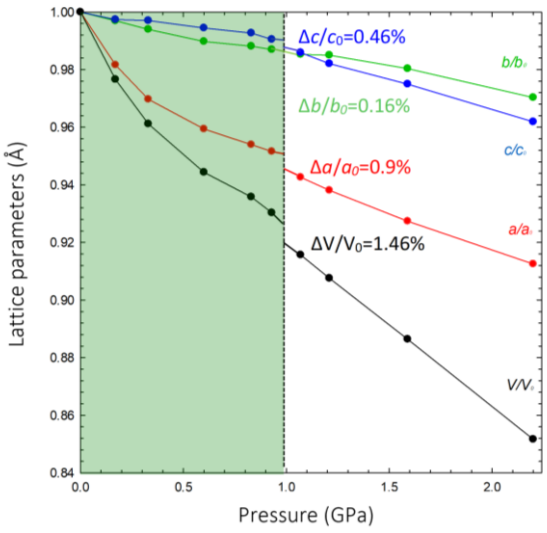



**Figure 64** Lattice parameters of scopolamine bromide as a function of hydrostatic pressure. The phase transition at 0.93 GPa is marked by vertical dashed lines.

Based on the lattice parameters, the linear compressibility coefficients $\alpha_i$ for scopolamine bromide (up to 0.93) along principal axis $i$ = 1, 2 and 3 were calculated and shown in Table 21.

**Table 21** Liner compressibility coefficients Ki for scopolamine bromide along principal axis i=1, 2 and 3 determined from in-situ high-pressure single crystal X-ray diffraction.

| | | Component of $\mathbf{x}_i$ along the crystallographic axes | | |
|---|---|---|---|---|
| Principal axis, *i* | $K_i$ (TPa$^{-1}$) | *a* | *b* | *c* |
| 1 | 31 (1) | 1 | 0 | 0 |
| 2 | 16 (2) | 0 | 1 | 0 |
| 3 | 14 (1) | 0 | 0 | 1 |

Corresponding compressibility indicatrix for scopolamine bromide along principal axis $i$ =1, 2 and 3 is visualized in Figure 65.

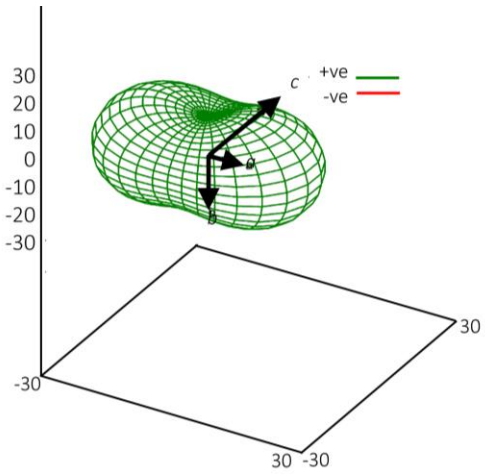



**Figure 65** Compressibility indicatrix for scopolamine bromide determined by the in-situ high pressure single crystal X-ray diffraction

Comparison between experimentally determined values of compressibility coefficients $K_i$ with the coefficients determined by DFT calculations is given in Table 23.

**Table 22** Linear compressibilities coefficients for N'-2-propylidene-4-hydroxybenzohydrazide Form I as obtained experimental in-situ high pressure single crystal X-ray diffraction vs. those obtained by DFT.

| | | | *Component of* $\boldsymbol{x}_i$ *along the crystallographic axes* | | |
|---|---|---|---|---|---|
| | $K_i$ ($TPa^{-1}$) for Form I | | | | |
| *Principal axis, i* | experiment | DFT | *a* | *b* | *c* |
| *1* | 31(1) | 2.06 | 0 | 1 | 0 |
| *2* | 16(2) | 3.40 | 0 | 0 | 1 |
| *3* | 14(1) | 2.73 | 1 | 0 | 0 |

Table 18 shows thar both DFT and experiment show positive compressibility along all principal axes. Although absolute values of compressibility determined by DFT and experiment differ by the factor of two due to the reason that owing to the large number of atoms in the unit cell of scopolamine bromide cruder approximations for the atom positions in all the computational steps had to be applied, the fact remains that compressibility is certainly positive along all three axes.

Beside the determination of compressibility coefficients of scopolamine bromide, another important finding was realized from the *in-situ* high-pressure single crystal X-ray diffraction experiment. As shown in figure 66., at 0.93 GPa scopolamine bromide undergoes the unprecedented isostructural phase transition to the ordered scopolamine bromide Form II. During this phase transition, *a* axis shrinks by 0.46%, *b* axis shrinks by 0.16% and the *c* shrinks the most, by 0.9%. Overall volume of the unit cell decreases by 1.46%. Table 23 shows basic structural information from scopolamine bromide and its ordered phase Form II.

**Table 23** Crystallographic data scopolamine bromide Form I at 0.1. MPa and scopolamine bromide Form II at 0.93 GPa

| Pressure (GPa) | 0.1 MPa (Form I) | 0.93 GPa (Form II) |
|---|---|---|
| Space group | $P2_12_12_1$ | $P2_12_12_1$ |
| Unit cell *a* (Å) | 7.0373(3) | 6.6968(5) |
| *b* | 10.9407(7) | 10.798(3) |
| *c* | 23.3327(14) | 23.112(5) |
| Volume ($Å^3$) | 1796.45(18) | 1671.3(7) |
| $D_X$ [$g/cm^3$] | 1.628 | 2.385 |

Crystal structures of scopolamine bromide Form I and Form II are shown in the overlay manner in Figure 66. Form I is shown in blue while the high-presssure Form II is given in red.

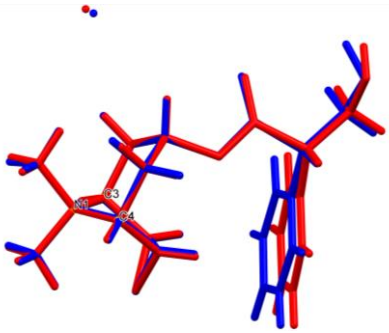


Figure 66 Crystal structures of scopolamine bromide Form I and Form II determined by in-situ high pressure single crystal X-ray diffraction

Fixed positions for an overlay between two forms are set on atoms N1, C3 and C4. It can clearly be seen that high-pressure Form II experiences a small conformation changes in the flexible part of molecule; the difference up to 5° in torsion angles is noticed. Even though the change in molecular structure does not seem very pronounced, crystal packing of high-pressure Form II exhibits quite significant difference as shown in Figure 67.

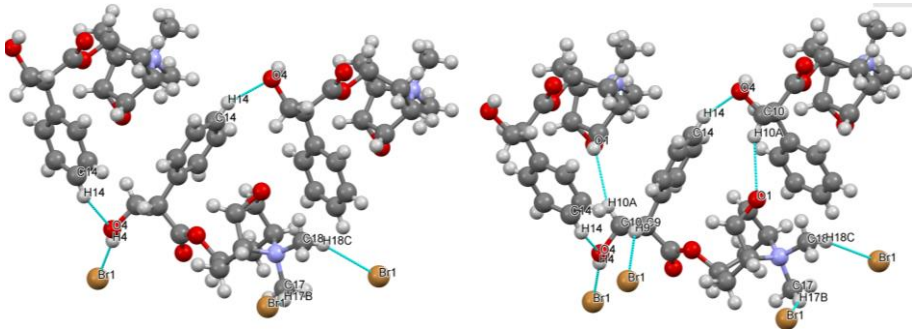



Figure 67 Crystal packing od scopolamine bromide Form I and Form II determined by in-situ high pressure single crystal X-ray diffraction

In the crystal packing of scopolamine bromide Form I several hydrogen bonds exist; oxygen atom O4 from hydroxyl group participates as a hydrogen donor towards Br anion [O4-H4···Br1] as well as hydrogen acceptor of benzene CH group from neighbouring molecule [C14-H14···O4]. Additionally, two interactions between Br anion and methyl group (from quaternary N atom) are formed [C17-H17···Br1 and C18-H18···Br1]. All mentioned H-bonds found in the case of scopolamine bromide Form I exist as in Form II but it is important to notice that new intermolecular interaction also appeared; oxygen atom O1 from tricyclic ring acts as a hydrogen acceptor from $CH_2$ group of neighbouring molecule [C10-H10A···O1].

In summary, proposed mechanism of thermosalient effect in oxitropium bromide, and other thermosalient materials that undergo polymorphic phase transition is as follows: heating of the crystals of the low temperature form causes various conformational changes of the

molecule which in turn induces changes of the crystal packing and anisotropic deformation of the unit cell. During this process, shear strain and elastic energy are accumulating inside the crystal lattice up to a certain point where they overcome the cohesive interactions. At that moment the energy is instantaneously released, the crystals switch from the low temperature polymorph to a high temperature polymorph, and this is accompanied with jumping. Changes of the unit-cell during phase transition are quite drastic – for example in oxitropium bromide the *b* axis increases by nearly 10%, *c* axis shrinks by 8% and this results in the net cell volume expansion of 4%. For comparison, in the whole temperature interval in which the experiments were conducted, from RT to 140 °C, the scopolamine bromide unit cell changes much less drastically; the *a* axis increases by 1.5%, *b* axis decreases by 0.8%, *c* axis increases by 1.2% and the overall volume of the unit cell increases by 2 %. Since phase transition can be ruled out as a governing force for thermosalient effect in scopolamine bromide, the only plausible explanation can be that it is caused by the extremely large and anisotropic thermal expansion. All thermosalient materials are characterized by unusually large thermal expansion coefficients which is to some extent balanced with uniaxial (sometimes even biaxial) negative thermal expansion. This is also true for the scopolamine bromide. This helps preserve the integrity of the crystal lattice and the crystal as a whole during thermal treatment which is causing the accumulation of the stress in the crystal lattice. Furthermore, this helps the accumulation of large elastic energy, up to a certain point after which it is being released and causes the crystals to jump. Contrary to other thermosalient solids, where thermosalient effect takes place on an extremely short time scale (less than 1 ms) because it is happening during the polymorphic phase transition, in the scopolamine bromide it is a continuous process. Thermosalient effect in scopolamine bromide takes place over the broad temperature interval of almost 20 °C, intensity of jumps is lower than for the oxitropium bromide, and all crystals remain intact whereas in the other thermosalient materials some crystals (usually large ones) are regularly shattered. All this confirms the continuity of thermosalient process in scopolamine bromide.

# 4. Conclusion

At the end of this thesis, we cannot help but wonder whether we are closer to the resolving the mystery of thermosalient effect or have we opened the Pandora's box and actually raised more questions about this phenomenon. Transformation of thermal energy into mechanical motion (work) is one of the basic natural processes of energy conversion. Such materials, which are capable of extremely fast and, more important, controllable energy conversion are extremely important candidates for active actuating elements, such as flexible electronic switches, displays, artificial muscles, microfluidic valves and gates, heat sensors etc. Until recently, soft materials such as polymers, elastomers or liquid crystalline materials were used for this purpose. But lately a whole new field is emerging where single crystals are being explored as such active elements. The main advantage of single crystals over their soft counterparts is the quickness of response (these effects take place on the timescale of less than 1 ms) and their ability of recovery to the initial condition. Some of these materials are capable of extreme mechanical motion, jumping to distances $10^5$-$10^6$ times their own size [6]. Even though the number of thermosalient systems reported is still very limited, new examples are emerging on a daily basis and this fact promises a bright future for research of this phenomenon, but also for their practical uses.

In this thesis, several thermosalient systems were investigated and several problems were tackled. We started with *N*'-2-propylidene-4-hydroxybenzohydrazide, a typical representative of thermosalient materials which has been extensively studied but most important conclusions about the mechanism of thermosalient effect in this system were drawn from theoretical studies based on DFT calculations. It was suggested by Skoko et al. [9] that the negative thermal expansion – which is observed in almost all thermosalient materials and is thought of as a governing force for thermosalient effect – is a consequence of another extraordinary feature – negative linear compressibility. Furthermore, the irreversibility of the phase transition from Form I to Form II, and reversibility of phase transitions between Forms II and III was explained by the way these phase transitions proceed which is through the path with least stress. In the thesis, the existence of negative linear compressibility and its coupling to the negative thermal expansion was experimentally proven and it was a very exciting moment because we were led to the idea that negative linear compressibility is the actual reason behind the thermosalient phenomenon. Our Raman measurements proved the theoretical suggestion of the phonon

softening while approaching phase transition, and this softening helps the system transform from one thermosalient phase to another. Furthermore, investigations of the sound propagation in this system confirmed that its elastic properties determine reversibility/irreversibility of phase transitions taking place. And finally, the mechanism of negative thermal expansion and negative linear compressibility was fully determined.

Following that, a derivatives of *N*'-2-propylidene-4-hydroxybenzohydrazide was investigated, 4-hydroxybenzohydrazide. It was shown that this compound does not exhibit thermosalient behaviour and it proved our suggestion that the presence of interpenetrated *zig-zag* spring-like chains that are mutually connected in 3D wine-rack network truly play a pivotal role in the manifestation of thermosalient effect in *N*'-2-propylidene-4-hydroxybenzohydrazide. Finally, several recrystallizations from different solvents were attempted. Recrystallization form 1:1 mixture of acetone and dichloromethane lead to the simultaneous formation of forms I and III and this just goes to prove how processes of crystallization of different polymorphic forms are extremely sensitive to conditions and that we have a lot to learn about these processes.

From this point, we moved on to study the thermosalient effect in oxitropium bromide and its derivatives, hoping to discover negative linear compressibility in them as well. Oxitropium bromide was extensively studied in this thesis regarding its thermal behaviour prior to the polymorphic phase transition. It came to no surprise that negative thermal expansion was discovered, and it yet confirmed our idea that it is the main reason behind thermosalient effect. As in all the other thermosalient systems, coefficients of thermal expansion were unusually large. Our theoretical calculations suggested that there is no negative linear compressibility in this system, so our idea about the negative linear compressibility being responsible for thermosalient effect became questionable. But maybe the theoretical calculations were wrong? Our analysis of the sound propagation show that perturbation can move extremely quickly in the oxitropium bromide, and that the flow of energy is focused and not dissipating, also involving low frequency phonons, which confirms assumption that thermosalient effect is caused by the cooperative movement of the molecules in the crystal with an extremely energetic and rapid phase transition. In the last step, the mechanism of negative thermal expansion was fully explained for oxitropium bromide.

In the next step, scopolamine bromide hydrate was prepared. This proved to be very opportune because it showed different mechanism of thermosalient effect was never reported in the literature before. Contrary to the other thermosalient materials, where the jumping of the crystals was caused by the generation of the stress in the crystal lattice caused by heating which is suddenly released during the highly anisotropic polymorphic phase transition, in this system

the jumping of the crystals is caused by the release of the water from the crystal lattice. Surprisingly, dehydration in this system is a continuous process, so the jumping of the crystals takes place on the broad temperature scale of around 20°C. In other thermosalient materials this happens in the temperature interval of about 5°C. But, as in other thermosalient materials, negative thermal expansion is also a feature of scopolamine bromide hydrate.

Last, and most curious, case investigated in this thesis was the case of scopolamine bromide. In this system, yet another mechanism for thermosalient effect was observed, not yet reported in the literature. All the measurements, structural and thermal, agree that there is no phase transition, nor any sort of chemical change (like in the case of scopolamine bromide hydrate) and yet crystals repeatedly jump in the broad temperature interval of about 20°C. At this point, we are not clear about the mechanism of thermosalient effect in this system. As in all the other thermosalient materials, negative thermal expansion is present here. We suppose that as in other thermosalient materials, it leads to the very anisotropic change of the unit cell which generate large strain in the crystal lattice which is at one point released in the form of the crystal jumps. But contrary to other thermosalient materials, here it happens without phase transition. DFT calculations in this system also suggested that there is no negative linear compressibility, so we checked it experimentally. Alas, the high-pressure experiments did indeed show that scopolamine bromide exhibits positive compressibility. This was the final proof that there is no need for existence of negative linear compressibility for thermosalient effect and that there is no coupling between it and negative thermal expansion.

In summary, we showed that all the thermosalient materials investigated exhibit negative thermal expansion and it confirms our suggestions that it is the governing force behind this mechanism. It enables large and anisotropic change of the unit cell, which causes the accumulation of the stress in the crystal lattice, large elastic energy is accumulated in this process and it is quickly and energetically released at one point, causing the crystals to jump, usually during the polymorphic phase transition. We found two more mechanisms of thermosalient effect, previously unreported in the literature. In one case, the crystals' jumps are caused by the release of the solvent. In other case, the crystals are jumping without phase transition of chemical change. In the future, we should be focused into finding new thermosalient materials which would further expand our knowledge about this fascinating effect. Once we understand it completely, we shall be able of fabricating thermosalient materials with highly tuneable properties which would enable the use of these materials in the real life.

# 5. References


[1] M. C. Etter e A. R. Siedle, «Solid-state rearrangement of (phenylazophenyl)palladium hexafluoroacetylacetonate,» *Journal of the American Chemical Society,* vol. 105, n. 21, pp. 641-643, 1983.

[2] S. Zamir, J. Bernstein e D. Greenwood, «Reversible solid-state phase transition of a 'thermosalient crystal',» *Acta Crystallographica Section A,* vol. 49, pp. 436-436, 1993.

[3] T. Steiner, W. Hinrichs, W. Saenger e R. Gigg, «Jumping crystals : X-ray structures of the three crystalline phases of (±)-3,4-di-O-acetyl-1,2,5,6-tetra-O-benzyl-myo-inositol,» *Acta Crystallographica Section B-structural Science,* vol. 49, n. 4, pp. 708-718, 1993.

[4] H. Lieberman, R. Davey e D. Newsham, «Br center dot center dot center dot Br and Br center dot center dot center dot H interactions in action: Polymorphism, hopping, and twinning in 1,2,4,5-tetrabromobenzene,» *Chemistry of Materials,* vol. 12, 2000.

[5] O. Crottaz, F. Kubel e H. Schmid, «Jumping crystals of the spinels NiCr2O4 andCuCr2O4,» *Journal of Materials Chemistry,* vol. 7, n. 1, pp. 143-146, 1997.

[6] P. Naumov, S. Chizhik, M. K. Panda, N. K. Nath e E. Boldyreva, «Mechanically Responsive Molecular Crystals,» *Chemical Reviews,* vol. 115, n. 22, pp. 12440-12490, 2015.

[7] M. K. Panda, T. Runčevski, S. C. Sahoo, A. A. Belik, N. K. Nath, R. E. Dinnebier e P. Naumov, «Colossal positive and negative thermal expansion and thermosalient effect in a pentamorphic organometallic martensite,» *Nature Communications,* vol. 5, n. 1, pp. 4811-4811, 2014.

[8] L. Zhang, C. Shen, M. Crow, L. Dong, S. Pekarek e S. Atcitty, «Performance Indices for the Dynamic Performance of FACTS and FACTS with Energy Storage,» *Electric Power Components and Systems,* vol. 33, n. 3, pp. 299-314, 2004.

[9] I. Lončarić, J. Popović, V. Despoja, S. Burazer, I. Grgičević, D. Popović e Ž. Skoko, «Reversible Thermosalient Effect of N′-2-Propylidene-4-hydroxybenzohydrazide Accompanied by an Immense Negative Compressibility: Structural and Theoretical Arguments Aiming toward the Elucidation of Jumping Phenomenon,» *Crystal Growth & Design,* vol. 17, n. 8, pp. 4445-4453, 2017.

[10] M. . Lusi e J. . Bernstein, «On the propulsion mechanism of “jumping” crystals,» *Chemical Communications,* vol. 49, n. 81, pp. 9293-9295, 2013.

[11] S. C. Sahoo, S. B. Sinha, M. S. R. N. Kiran, U. Ramamurty, A. F. Dericioglu, C. M. Reddy e P. Naumov, «Kinematic and mechanical profile of the self-actuation of thermosalient crystal twins of 1,2,4,5-tetrabromobenzene: a molecular crystalline analogue of a bimetallic strip.,» *Journal of the American Chemical Society,* vol. 135, n. 37, pp. 13843-13850, 2013.

[12] B. A. Zakharov, A. A. L. Michalchuk, C. A. Morrison e E. V. Boldyreva, «Anisotropic lattice softening near the structural phase transition in the thermosalient crystal 1,2,4,5-tetrabromobenzene,» *Physical Chemistry Chemical Physics,* vol. 20, n. 13, pp. 8523-8532, 2018.

[13] J. H. Ko, K. S. Lee, S. C. Sahoo e P. Naumov, «Isomorphous phase transition of 1,2,4,5-tetrabromobenzene jumping crystals studied by Brillouin light scattering,» *Solid State Communications,* vol. 173, pp. 46-50, 2013.

[14] R. J. Davey, S. J. Maginn, S. J. Andrews, S. N. Black, A. M. Buckley, D. Cottier, P. Dempsey, R. Plowman, J. E. Rout, D. R. Stanley e A. Taylor, «Morphology and polymorphism in molecular crystals: terephthalic acid,» *Journal of the Chemical Society, Faraday Transactions,* vol. 90, n. 7, pp. 1003-1009, 1994.

[15] A. Khalil, D. P. Karothu e P. Naumov, «Direct Quantification of Rapid and Efficient Single-Stroke Actuation by a Martensitic Transition in a Thermosalient Crystal,» *Journal of the American Chemical Society,* vol. 141, n. 8, pp. 3371-3375, 2019.

[16] M. K. Panda, T. Runčevski, A. Husain, R. E. Dinnebier e P. Naumov, «Perpetually Self-Propelling Chiral Single Crystals,» *Journal of the American Chemical Society,* vol. 137, n. 5, pp. 1895-1902, 2015.

[17] Ž. Skoko, S. Zamir, P. Naumov e J. Bernstein, «The thermosalient phenomenon. "Jumping crystals" and crystal chemistry of the anticholinergic agent oxitropium bromide.,» *Journal of the American Chemical Society,* vol. 132, n. 40, pp. 14191-14202, 2010.

[18] S. Mittapalli, D. S. Perumalla e A. Nangia, «Mechanochemical synthesis of N-salicylideneaniline: thermosalient effect of polymorphic crystals,» *IUCrJ,* vol. 4, n. 3, pp. 243-250, 2017.

[19] S. Mittapalli, D. S. Perumalla, J. B. Nanubolu e A. Nangia, «Thermomechanical effect in molecular crystals: the role of halogen-bonding interactions,» *IUCrJ,* vol. 4, n. 6, pp. 812-823, 2017.

[20] M. I. Tamboli, D. P. Karothu, M. S. Shashidhar, R. G. Gonnade e P. Naumov, «Effect of Crystal Packing on the Thermosalient Effect of the Pincer-Type Diester Naphthalene-2,3-diyl-bis(4-fluorobenzoate): A New Class II Thermosalient Solid.,» *Chemistry: A European Journal,* vol. 24, n. 16, pp. 4133-4139, 2018.

[21] J. Ding, R. Herbst, K. Praefcke, B. Kohne e W. Saenger, «A crystal that hops in phase transition, the structure of trans,trans,anti,trans,trans-perhydropyrene,» *Acta Crystallographica Section B-structural Science,* vol. 47, n. 5, pp. 739-742, 1991.

[22] J. M. Corbett e M. H. Dickman, «4,5-Bis(fluorodinitromethyl)-2-methoxy-1,3-dioxolane,» *Acta Crystallographica Section C-crystal Structure Communications,* vol. 52, n. 7, pp. 1851-1853, 1996.

[23] K. Takimiya, N. Thorup e J. Becher, «A Flexible Cyclophane: Design, Synthesis, and Structure of a Multibridged Tris-tetrathiafulvalene (TTF) Macrocycle,» *Chemistry: A European Journal,* vol. 6, n. 11, pp. 1947-1954, 2000.

[24] T. Siegrist, C. Besnard, S. Haas, M. Schiltz, P. Pattison, D. Chernyshov, B. Batlogg e C. Kloc, «A Polymorph Lost and Found: The High-Temperature Crystal Structure of Pentacene,» *Advanced Materials,* vol. 19, n. 16, pp. 2079-2082, 2007.

[25] M. A. Fernandes, D. C. Levendis e F. R. L. Schoening, «A new polymorph of ortho-ethoxy-trans-cinnamic acid: single-to-single-crystal phase transformation and mechanism,» *Acta Crystallographica Section B-structural Science,* vol. 60, n. 3, pp. 300-314, 2004.

[26] S. Ohtani, M. Gon, K. Tanaka e Y. Chujo, «A Flexible, Fused, Azomethine–Boron Complex: Thermochromic Luminescence and Thermosalient Behavior in Structural Transitions between Crystalline Polymorphs,» *Chemistry: A European Journal,* vol. 23, n. 49, pp. 11827-11833, 2017.

[27] L. Robertson, N. Penin, V. Blanco-Gutierrez, D. Sheptyakov, A. Demourgues e M. Gaudon, «CuMo0.9W0.1O4 phase transition with thermochromic, piezochromic, and thermosalient effects,» *Journal of Materials Chemistry C,* vol. 3, n. 12, pp. 2918-2924, 2015.

[28] H.-S. So, T. Minami, T. Jindo e S. Matsumoto, «Thermosalient effect of two polymorphs of a diketopyrrolopyrrole dye with different crystal systems and molecular arrangements,» *CrystEngComm,* vol. 20, n. 36, pp. 5317-5320, 2018.

[29] Y. Kamo, I. Nagaya, R. Sugino e H. Hagiwara, «Jumping Crystals of Stacked Planar Cobalt Complexes: Thermosalient Effect Promoted by Hydrogen-bonded Lattice Solvent Release,» *Chemistry Letters,* vol. 48, n. 9, pp. 1077-1080, 2019.

[30] P. Gaztañaga, R. Baggio, E. Halac e D. R. Vega, «Thermal, spectroscopic and structural analysis of a thermosalient phase transformation in tapentadol hydrochloride,» *Acta Crystallographica Section B Structural Crystallography and Crystal Chemistry,* vol. 75, n. 2, pp. 183-191, 2019.

[31] T. Takeda e T. Akutagawa, «Anisotropic Dissociation of π–π Stacking and Flipping-Motion-Induced Crystal Jumping in Alkylacridones and Their Dicyanomethylene Derivatives,» *Chemistry: A European Journal,* vol. 22, n. 23, pp. 7763-7770, 2016.

[32] V. I. Ovcharenko, S. V. Fokin, E. Y. Fursova, O. V. Kuznetsova, E. V. Tretyakov, G. V. Romanenko e A. S. Bogomyakov, «"Jumping Crystals": Oxygen-Evolving Metal-Nitroxide Complexes,» *Inorganic Chemistry,* vol. 50, n. 10, pp. 4307-4312, 2011.

[33] M. Singh, S. Bhandary, R. Bhowal e D. Chopra, «Observation of bending, cracking and jumping phenomena on cooling and heating of tetrahydrate berberine chloride crystals,» *CrystEngComm,* vol. 20, n. 16, pp. 2253-2257, 2018.

[34] N. K. Nath, M. K. Panda, S. C. Sahoo e P. Naumov, «Thermally induced and photoinduced mechanical effects in molecular single crystals—a revival,» *CrystEngComm,* vol. 16, n. 10, pp. 1850-1858, 2014.

[35] Y. Bar-Cohen e Q. Zhang, «Electroactive Polymer Actuators and Sensors,» *Mrs Bulletin,* vol. 33, n. 3, pp. 173-181, 2008.

[36] A. Khalil, E. Ahmed e P. Naumov, «Metal-coated thermosalient crystals as electrical fuses,» *Chemical Communications,* vol. 53, n. 60, pp. 8470-8473, 2017.

[37] R. E. Newnham, Properties of Materials: Anisotropy, Symmetry, Structure, 2005.

[38] E. Grüneisen, «Theorie des festen Zustandes einatomiger Elemente,» *Annalen der Physik,* vol. 344, n. 12, pp. 257-306, 1912.

[39] D. C. Wallace, «Thermoelastic Theory of Stressed Crystals and Higher-Order Elastic Constants,» *Journal of Physics C: Solid State Physics,* vol. 25, pp. 301-404, 1970.

[40] T. H. K. Barron e R. W. Munn, «Thermodynamics of solids under stress,» *Pure and Applied Chemistry,* vol. 22, n. 3, pp. 527-534, 1970.

[41] Z. Liu, Q. Gao, J. Chen, J. Deng, K. Lin e X. Xing, «Negative thermal expansion in molecular materials,» *Chemical Communications,* vol. 54, n. 41, pp. 5164-5176, 2018.

[42] B. Singh, M. K. Gupta, R. Mittal, M. Zbiri, S. A. Hodgson, A. L. Goodwin, H. Schober e S. L. Chaplot, «Anomalous Lattice Dynamics in AgC4N3: Insights From Inelastic Neutron Scattering and Density Functional Calculations,» *Frontiers in Chemistry,* vol. 6, p. 544, 2018.

[43] Z. Liu, C. Liu, Q. Li, J. Chen e X. Xing, «Spring-like motion caused large anisotropic thermal expansion in nonporous M(eim)2 (M = Zn, Cd).,» *Physical Chemistry Chemical Physics,* vol. 19, n. 36, pp. 24436-24439, 2017.

[44] A. L. Goodwin e C. J. Kepert, «Negative thermal expansion and low-frequency modes in cyanide-bridged framework materials,» *Physical Review B,* vol. 71, n. 14, p. 140301, 2005.

[45] Q. Gao, N. Shi, A. Sanson, Y. Sun, R. Milazzo, L. Olivi, H. Zhu, S. H. Lapidus, L. Zheng, J. Chen e X. Xing, «Tunable Thermal Expansion from Negative, Zero, to Positive in Cubic Prussian Blue Analogues of GaFe(CN)(6),» *Inorganic Chemistry,* vol. 57, n. 22, pp. 14027-14030, 2018.

[46] A. B. Cairns e A. L. Goodwin, «Negative linear compressibility,» *Physical Chemistry Chemical Physics,* vol. 17, n. 32, pp. 20449-20465, 2015.

[47] L. Ming, M. Manghnani, T. Matsui e J. Jamieson, «Phase transformations and elasticity in rutile-structured difluorides and dioxides,» *Physics of the Earth and Planetary Interiors,* vol. 23, n. 4, pp. 276-285, 1980.

[48] J. C. Jamieson e D. B. McWhan, «Crystal Structure of Tellurium at High Pressures,» *Journal of Chemical Physics,* vol. 43, n. 4, pp. 1149-1152, 1965.

[49] M. Takahashi, «Terahertz Vibrations and Hydrogen-Bonded Networks in Crystals,» *Crystals,* vol. 4, n. 2, pp. 74-103, 2014.

[50] R. A. Young, «THE RIETVELD METHOD,» *Crystal Research and Technology,* vol. 30, n. 4, 2006.

[51] L. Lutterotti e P. Scardi, «Simultaneous structure and size-strain refinement by the Rietveld method,» *Journal of Applied Crystallography,* vol. 23, n. 4, pp. 246-252, 1990.

[52] S. Anzellini e S. Boccato, «A Practical Review of the Laser-Heated Diamond Anvil Cell for University Laboratories and Synchrotron Applications,» *Crystals,* vol. 10, n. 6, p. 459, 2020.

[53] A. W. Coats e J. P. Redfern, «Thermogravimetric analysis. A review,» *Analyst,* vol. 88, n. 1053, pp. 906-924, 1963.

[54] E. Smith e G. Dent, Modern Raman Spectroscopy: A Practical Approach, 2005.

[55] N. Argaman e G. Makov, «Density functional theory: An introduction,» *American Journal of Physics,* vol. 68, n. 1, pp. 69-79, 2000.

[56] M. J. Rutter e V. Heine, «Phonon free energy and devil's staircases in the origin of polytypes,» *Journal of Physics: Condensed Matter,* vol. 9, n. 9, pp. 2009-2024, 1997.

[57] V. H. a. O. J. W.-S. Zeng, «The structure of barium in the hexagonal close-packed phase under high pressure,» *J. Phys.: Condens. Matter 9,* p. 3489–3502, 1997.

[58] F. K. e. al., «Structure and bonding of liquid Se,» *J. Phys.: Condens. Matter ,* vol. 8, p. 9353–9357, 1996.

[59] R. C. a. M. Parrinello, «Unified approach for molecular dynamics and density-functional theory,» *Phys. Rev. Lett.,* vol. 55, p. 2471–2474, 1955.

[60] W. Kohn, a. A. D. Becke e R. G. Parr, «Density Functional Theory of Electronic Structure,» *The Journal of Physical Chemistry,* vol. 100, n. 31, pp. 12974-12980, 1996.

[61] C. M. Kube, «Elastic anisotropy of crystals,» *AIP Advances,* vol. 6, n. 9, p. 95209, 2016.

[62] J. W. Jaeken e S. Cottenier, «Solving the Christoffel equation: Phase and group velocities,» *Computer Physics Communications,* vol. 207, pp. 445-451, 2016.

[63] R. Centore, M. Jazbinsek, A. Tuzi, A. Roviello, A. Capobianco e A. Peluso, «A series of compounds forming polar crystals and showing single-crystal-to-single-crystal transitions between polar phases,» *CrystEngComm,* vol. 14, n. 8, pp. 2645-2653, 2012.

[64] M. J. Cliffe e A. L. Goodwin, «PASCal: a principal axis strain calculator for thermal expansion and compressibility determination,» *Journal of Applied Crystallography,* vol. 45, n. 6, pp. 1321-1329, 2012.

[65] M. Zema, G. Ventruti e S. C. Tarantino, «Geometry limitation-free HT device for in situ/operando SCXRD,» *Acta Crystallographica Section A,* vol. 73, 2017.

[66] B. Bruker, «APEX2, SAINT and TWINABS,» *AXS Inc., Madison,* 2008.

[67] G. M. Sheldrick, «SADABS, Program for Empirical Absorption Correction of Area Detector Data,» *SADABS,* 1996.

[68] G. M. Sheldrick, «Crystal structure refinement with SHELXL,» *Acta Crystallographica Section C-crystal Structure Communications,* vol. 71, n. 1, pp. 3-8, 2015.

[69] A. Griffin e A. Bond, «CrysAlisPRO: facilitating variable temperature experiments,» *Acta Crystallographica Section A,* vol. 67, 2011.

[70] O. V. Dolomanov, L. J. Bourhis, R. J. Gildea, J. A. K. Howard e H. Puschmann, «OLEX2: a complete structure solution, refinement and analysis program,» *Journal of Applied Crystallography,* vol. 42, n. 2, pp. 339-341, 2009.

[71] P. Giannozzi, S. Baroni, N. Bonini, M. Calandra, R. Car, C. Cavazzoni, D. Ceresoli, G. L. Chiarotti, m. Cococcioni, I. Dabo, A. D. Corso, S. Fabris, G. Fratesi, S. d. Gironcoli, R. Gebauer, U. Gerstmann, C. Gougoussis, A. Kokalj, M. Lazzeri, L. Martin-Samos, N. Marzari, F. Mauri, R. Mazzarello, S. Paolini, A. Pasquarello, L. Paulatto, C. Sbraccia, S. Scandolo, G. Sclauzero, A. P. Seitsonen, A. Smogunov, P. Umari e R. M. Wentzcovitch, «Quantum ESPRESSO: a modular and open-source software project for quantum simulations of materials,» *arXiv preprint arXiv:0906.2569,* 2009.

[72] K. F. Garrity, J. W. Bennett, K. M. Rabe e D. Vanderbilt, «Pseudopotentials for high-throughput DFT calculations,» *Computational Materials Science,* vol. 81, pp. 446-452, 2014.

[73] K. Berland, V. R. Cooper, K. Lee, E. Schröder, T. Thonhauser, P. Hyldgaard e B. I. Lundqvist, «van der Waals forces in density functional theory: a review of the vdW-DF method.,» *Reports on Progress in Physics,* vol. 78, n. 6, p. 66501, 2015.

[74] D. Sun, D.-H. Kim, D. Le, Ø. Borck, K. Berland, K. Kim, W. Lu, Y. Zhu, M. Luo, J. Wyrick, Z. Cheng, T. L. Einstein, T. S. Rahman, P. Hyldgaard e L. Bartels, «Publisher's Note: Effective elastic properties of a van der Waals molecular monolayer at a metal surface [Phys. Rev. B 82, 201410 (2010)],» *Physical Review B,* vol. 82, n. 23, 2010.

[75] M. K. Panda, R. Centore, M. Causà, A. Tuzi, F. Borbone e P. Naumov, «Strong and Anomalous Thermal Expansion Precedes the Thermosalient Effect in Dynamic Molecular Crystals.,» *Scientific Reports,* vol. 6, n. 1, pp. 29610-29610, 2016.

[76] J. W. E. Mariathasan, L. W. Finger e R. M. Hazen, «High-pressure behavior of LaNbO4,» *Acta Crystallographica Section B-structural Science,* vol. 41, n. 3, pp. 179-184, 1985.

[77] D. R. McCann, L. Cartz, R. E. Schmunk e Y. D. Harker, «Compressibility of Hexagonal Selenium by X-Ray and Neutron Diffraction,» *Journal of Applied Physics,* vol. 43, n. 4, pp. 1432-1436, 1972.

[78] J. Haines, C. Chateau, J. M. Léger, C. Bogicevic, S. Hull, D. D. Klug e J. S. Tse, «Collapsing cristobalitelike structures in silica analogues at high pressure.,» *Physical Review Letters,* vol. 91, n. 1, p. 15503, 2003.

[79] R. H. Baughman, S. Stafström, C. Cui e S. O. Dantas, «Materials with Negative Compressibilities in One or More Dimensions,» *Science,* vol. 279, n. 5356, pp. 1522-1524, 1998.

[80] A. L. Goodwin, D. A. Keen e M. G. Tucker, «Large negative linear compressibility of Ag3[Co(CN)6],» *Proceedings of the National Academy of Sciences of the United States of America,* vol. 105, n. 48, pp. 18708-18713, 2008.

[81] W. Li, M. R. Probert, M. Kosa, T. D. Bennett, A. Thirumurugan, R. P. Burwood, M. Parinello, J. A. K. Howard e A. K. Cheetham, «Negative Linear Compressibility of a Metal–Organic Framework,» *Journal of the American Chemical Society,* vol. 134, n. 29, pp. 11940-11943, 2012.

[82] A. D. Fortes, E. Suard e K. S. Knight, «Negative Linear Compressibility and Massive Anisotropic Thermal Expansion in Methanol Monohydrate,» *Science,* vol. 331, n. 6018, pp. 742-746, 2011.

[83] W. Cai e A. Katrusiak, «Giant negative linear compression positively coupled to massive thermal expansion in a metal–organic framework,» *Nature Communications,* vol. 5, n. 1, pp. 4337-4337, 2014.

[84] J. Anwar, S. C. Tuble e J. Kendrick, «Concerted molecular displacements in a thermally-induced solid-state transformation in crystals of DL-norleucine,» *Journal of the American Chemical Society,* vol. 129, n. 9, pp. 2542-2547, 2007.

[85] D. Bučar, R. W. Lancaster e J. Bernstein, «Disappearing Polymorphs Revisited,» *Angewandte Chemie,* vol. 54, n. 24, pp. 6972-6993, 2015.

[86] J. F. Nye, Physical properties of crystals, 1985.

[87] J.-P. Zhang, H.-L. Zhou, D.-D. Zhou, P.-Q. Liao e S. Kitagawa, «Dynamic Behavior of Porous Coordination Polymers,» *,* vol. 7, pp. 425-474, 2013.

[88] J.-P. Dutasta, «Book Review: Container Molecules and Their Guests. By D. J. Cram and J. M. Cram. (Series: Monographs in Supramolecular Chemistry, Vol. 4),» *Angewandte Chemie,* vol. 34, n. 22, pp. 2563-2564, 1995.

[89] A. Bousseksou, G. Molnár, L. Salmon e W. Nicolazzi, «Molecular spin crossover phenomenon: recent achievements and prospects,» *Chemical Society Reviews,* vol. 40, n. 6, pp. 3313-3335, 2011.

[90] J. G. Delly, «THE MICROCHEMICAL BENCH. PART 6. THE LITERATURE OF CLASSICAL MICROCHEMISTRY,» *Microscope,* vol. 47, n. 1, pp. 13-28, 1999.

[91] M. Paine, U. König e E. Staples, «Application of Rapid X-Ray Diffraction (Xrd) and Cluster Analysis to Grade Control of Iron Ores,» , pp. 495-501, 2012.

[92] J. A. Dean, Analytical Chemistry Handbook, 1995.

[93] J. Abraham, A. P. Mohammed, M. A. Kumar, S. C. George e S. Thomas, «Thermoanalytical Techniques of Nanomaterials,» , pp. 213-236, 2018.

[94] S. Grimme, J. Antony, S. Ehrlich e H. Krieg, «A consistent and accurate ab initio parametrization of density functional dispersion correction (DFT-D) for the 94 elements H-Pu,» *Journal of Chemical Physics,* vol. 132, n. 15, p. 154104, 2010.

[95] I. A. Fedorov, C. V. Nguyen e A. Y. Prosekov, «Study of the Elastic Properties of the Energetic Molecular Crystals Using Density Functionals with van der Waals Corrections,» *ACS Omega,* vol. 6, n. 1, pp. 642-648, 2021.

[96] A. B. Cairns, A. L. Thompson, M. G. Tucker, J. Haines e A. L. Goodwin, «Rational Design of Materials with Extreme Negative Compressibility: Selective Soft-Mode Frustration in KMn[Ag(CN)2]3,» *Journal of the American Chemical Society,* vol. 134, n. 10, pp. 4454-4456, 2012.

# 6. List of figures

**Figure 1** Crystal structures of β Form and γ Form of 1,2,4,5-tetrabromobenzene [12] ..... 11

**Figure 2** Crystal structure do Form II and form III of (±)-3,4-diO-acetyl-1,2,5,6-tetra-O-benzyl-myo-inositol [3] ..... 11

**Figure 3** Crystal structure of Form I and Form II of pyroglutamic acid [16] ..... 12

**Figure 4** Principal mechanisms leading to negative thermal expansion in molecular materials [41] ..... 20

**Figure 5** Negative thermal expansion in materials with 2D perovskite topology [42] ..... 20

**Figure 6** Spring-like motion causing large anisotropic thermal expansion in nonporous $M(eim)_2$ (M = Zn, Cd) [43] ..... 21

**Figure 7** Cubic structure of $GaFe(CN)_6$ [45] ..... 21

**Figure 8** Ferroelastic NLC mechanism in rutiles [47] ..... 24

**Figure 9** The β-cristobalite structure of $BEO_4$ (E = P, As) exhibiting subsequent rotation of all tetrahedral units about the tetrad axis. [46] ..... 25

**Figure 10** The crystal structure of selenium and tellurium consists of a triangular array of trigonal helices [48] ..... 25

**Figure 11** Wine-rack and honeycomb-like topologies known to favor negative linear compressibility and corresponding chemical systems [45] ..... 26

**Figure 12** Representation by vectors of Brag's law ..... 29

**Figure 13** Bragg-Brentano geometry [50] ..... 30

**Figure 14** Diamond anvil cell [53] ..... 33

**Figure 15** Chemical formula of N'-2-propylidene-4-hydroxybenzohydrazide ..... 43

**Figure 16** Linear compressibility indicatrix of N'-2-propylidene-4-hydroxybenzohydrazide Form I determined from DFT stiffness matrix calculations. ..... 45

**Figure 17** Lattice parameters of N'-2-propylidene-4-hydroxybenzohydrazide Form I as a function of hydrostatic pressure determined by in-situ high-pressure single crystal diffraction. ..... 46

**Figure 18** Compressibility indicatrix for N'-2-propylidene-4-hydroxybenzohydrazide Form I determined by the in-situ high pressure single crystal X-ray diffraction. ..... 47

**Figure 19** Comparison of thermal expansivity indicatrix and the compressibility indicatrix for N'-2-propylidene-4-hydroxybenzohydrazide Form I, II and III. ..... 49

**Figure 20** In-situ high-temperature Raman spectra for N'-2-propylidene-4-hydroxybenzohydrazide Form I (approaching phase transition from Form I to Form II) and for Form II(approaching phase transition from Form II to Form III). ..... 51

**Figure 21** Sound waves group velocities for three forms of N'-2-propylidene-4-hydroxybenzohydrazide ..... 52

**Figure 22** Crystal packing of N'-2-propylidene-4-hydroxybenzohydrazide Form III ..... 54

**Figure 23** Inverse relationship of N'-2-propylidene-4-hydroxybenzohydrazide Form III ..... 54

**Figure 24** Crystal packing of N'-2-propylidene-4-hydroxybenzohydrazide Form I ..... 55

**Figure 25** Crystal packing of N'-2-propylidene-4-hydroxybenzohydrazide Form I ..... 56

**Figure 26** Chemical formula of N'-2-propylidene-4-hydroxybenzohydrazide and its derivative 4-hydroxybenzohydrazide ..... 57

**Figure 27** Crystal structure of 4-hydroxybenzohydrazide. ..... 57

**Figure 28** Hydrogen bonding in propylidene-deficient derivative 4-hydroxybenzohydrazide. ..... 58

**Figure 29** Crystal packing of N'-2-propylidene-4-hydroxybenzohydrazide and 4-hydroxybenzohydrazide. ..... 58

**Figure 30** Rietveld refinements for N'-2-propylidene-4-hydroxybenzohydrazide recrystallized from acetone-DCM. Experimental data are given as black line, calculated diffraction pattern as blue line while the sky blue and turquoise vertical lines represent positions. ..... 59

**Figure 31** Molecular formula of oxitropium bromide. ..... 61

**Figure 32** In-situ high-temperature X-ray powder diffraction data of oxitropium bromide Form A and Form B in the temperature range T=-45 – 110 °C. ..... 63

**Figure 33** Rietveld structure refinements of oxitropium bromide 30 °C and 60 °C. Experimental data are given as black line, calculated diffraction pattern as blue line while the dark blue and red vertical lines represent positions of Bragg reflections of oxitropium. ..... 64

**Figure 34** Unit cell parameters of oxitropium bromide as a function of temperature determined by in-situ high-temperature powder X-ray diffraction from -45°C – 15°C and in-situ high-temperature single crystal X-ray diffraction 24°C – 138°C. Blue and red rectangles. ..... 65

**Figure 35** Thermal expansivity indicatrix of oxitropium bromide form A and B determined from in-situ high-temperature single crystal and powder X-ray diffraction. ..... 66

**Figure 36** Linear compressibility indicatrix for oxitropium bromide Form A determined from DFT stiffness matrix calculations. ..... 68

**Figure 37** In-situ high-temperature Raman spectra in low frequencies range of oxitropium bromide Form A and Form B, collected at 300 K and 343 K, respectively. ..... 69

**Figure 38** Phase velocity of waves through oxitropium bromide Form A ..... 70

**Figure 39** Group velocity of waves through oxitropium bromide Form A ..... 70

**Figure 40** Enchantment factor of waves for oxitropium bromide ..... 70

**Figure 41** Waves power flow for oxitropium bromide Form A ..... 71

**Figure 42** Crystal packing of oxitropium bromide Form A. ..... 72

**Figure 43** Coupling of orthogonally directed negative expansion with positive expansion for oxitropium bromide Form A. ..... 73

**Figure 44** Chemical structures of oxitropium bromide and scopolamine bromide. ..... 74

**Figure 45** Crystal structure of scopolamine bromide hydrate ..... 75

**Figure 46** 2D layers in bc plane formed by hydrogen bond network involving water molecule. ..... 76

**Figure 47** Hot stage microscopy image of scopolamine bromide hydrate crystals, before heating (left) and after heating (right). ..... 77

**Figure 48** Scopolamine bromide hydrate crystal immersed in oil under heating on hot stage microscope. ..... 77

**Figure 49** In-situ high-temperature X-ray powder diffraction data of scopolamine bromide hydrate in the temperature range T=25-75 °C. ..... 78

**Figure 50** Rietveld structure refinements of scopolamine bromide hydrate 25 °C and 70 °C. Experimental data are given as black line, calculated diffraction pattern as blue line while the dark blue and red vertical lines represent positions of Bragg reflections of scopolamine bromide hydrate and scopolamine bromide, respectively. ..... 79

**Figure 51** Occupancy of oxygen atom (O5) from water molecules as a function of temperature determined by in-situ high-temperature single crystal X-ray diffraction ..... 79

**Figure 52** Weight loss of scopolamine bromide hydrate as a function of temperature during heating run (red curve) and weight gain during cooling run (blue curve). ..... 80

**Figure 53** Unit cell parameters of scopolamine bromide (1-x)hydrate as a function of temperature determined by in-situ high-temperature single crystal X-ray diffraction. Blue and red rectangles denote hydrate and anhydrous form, respectively. ..... 81

Figure 54 Crystal packing of scopolamine bromide hydrate and its anhydrous form in bc plane. ..... 82

**Figure 55** Crystals of scopolamine bromide before jumping (left panel) and after jumping (right panel). ..... 84

**Figure 56** Differential scanning calorimetry of scopolamine bromide. ..... 85

**Figure 57** In-situ high-temperature X-ray powder diffraction data of scopolamine bromide in the temperature range T= 35-185 °C. ..... 85

**Figure 58** Rietveld structure refinements of scopolamine bromide hydrate 307 K °C and 447 K. Experimental data are given as black line, calculated diffraction pattern as blue line while the dark blue vertical lines represent positions of Bragg reflections of scopolamine bromide. ..... 86

**Figure 59** Unit cell parameters of scopolamine bromide as a function of temperature determined by in-situ high-temperature single crystal X-ray diffraction T= 20 -150 °C. ..... 87

**Figure 60** Thermal expansivity indicatrix of scopolamine bromide determined from in-situ high-temperature single crystal X-ray diffraction. ..... 87

**Figure 61** Crystal packing of scopolamine bromide. ..... 88

**Figure 62** Coupling of orthogonally directed negative expansion with positive expansion for scopolamine bromide ..... 88

**Figure 63** Linear compressibility indicatrix for scopolamine bromide determined from DFT stiffness matrix calculations..... 90

**Figure 64** Lattice parameters of scopolamine bromide as a function of hydrostatic pressure. The phase transition at 0.93 GPa is marked by vertical dashed lines. ..... 91

**Figure 65** Compressibility indicatrix for scopolamine bromide determined by the in-situ high pressure single crystal X-ray diffraction ..... 91

**Figure 66** Crystal structures of scopolamine bromide Form I and Form II determined by in-situ high pressure single crystal X-ray diffraction ..... 93

**Figure 67** Crystal packing od scopolamine bromide Form I and Form II determined by in-situ high pressure single crystal X-ray diffraction ..... 93

# 7. LIST OF TABLES

**Table 1** Examples of thermosalient materials ..... 4

**Table 2** Standard parameters for X-ray powder diffraction data collection..... 39

**Table 3** Liner compressibility coefficients $K_i$ for N'-2-propylidene-4-hydroxybenzohydrazide Form I along principal axis i=1, 2 and 3 determined from in-situ high-pressure single crystal X-ray diffraction. ..... 46

**Table 4** Linear compressibilities coefficients for N'-2-propylidene-4-hydroxybenzohydrazide Form I as obtained experimental in-situ high pressure single crystal X-ray diffraction vs. those obtained by DFT. ..... 47

**Table 5** Components of Grüneisen parameters $\gamma_1$, $\gamma_2$ and $\gamma_3$ for N'-2-propylidene-4-hydroxybenzohydrazide Form I, II and III50

**Table 6** In-situ high-tempearture low frequency Raman peaks positions of N'-2-propylidene-4-hydroxybenzohydrazide Form I and Form, obtained by Pseud-Voight fitting. ..... 51

**Table 7** Anisotropy parameters for three forms of N'-2-propylidene-4-hydroxybenzohydrazide from elastic constants ..... 53

**Table 8** Thermal expansion coefficients αi along principal axis i =1, 2 and 3 for oxitropium bromide Form A determined from in-situ high-temperature X-ray diffraction ..... 65

**Table 9** Thermal expansion coefficients αi along principal axis i =1, 2 and 3 for oxitropium bromide Form B determined from in-situ high-temperature X-ray diffraction ..... 65

**Table 10** Elastic constants Cij for oxitropium bromide Form A..... 67

**Table 11** Elastic compliance constants Sij for oxitropium bromide Form A ..... 67

**Table 12** Principal compressibilities Ki for for oxitropium bromide Forma A along the principal axes i=1, 2 and 3 determined from DFT stiffness matrix calculations..... 67

**Table 13** Components of Grüneisen parameters $\gamma_1$, $\gamma_2$ and $\gamma_3$ for oxitropium bromide Form A..... 68

**Table 14** In-situ high-tempearture low frequency Raman peaks positions of oxitropium bromide Form A and Form B, obtained by Pseud-Voight fitting. ..... 69

**Table 15** Anisotropy parameters for oxitropium bromide form A calculated from elastic constants ..... 71

**Table 16** Thermal expansion coefficients αi along principal axis i=1, 2 and 3 for oxitropium bromide Form A determined from in-situ high-temperature X-ray diffraction. ..... 87

**Table 17** Elastic constants Cij for scopolamine bromide ..... 89

**Table 18** Elastic compliance constants Sij for scopolamine bromide ..... 89

Table 19 Principal compressibilities Ki for for scopolamine bromide along the principal axes i=1, 2 and 3 determined from DFT stiffness matrix calculations..... 89

Table 20 Components of Grüneisen parameters $\gamma_1$, $\gamma_2$ and $\gamma_3$ for scopolamine bromide ..... 90

**Table 21** Liner compressibility coefficients Ki for scopolamine bromide along principal axis i=1, 2 and 3 determined from in-situ high-pressure single crystal X-ray diffraction. ..... 91

**Table 22** Linear compressibilities coefficients for N'-2-propylidene-4-hydroxybenzohydrazide Form I as obtained experimental in-situ high pressure single crystal X-ray diffraction vs. those obtained by DFT. ..... 92

**Table 23** Crystallographic data scopolamine bromide Form I at 0.1. MPa and scopolamine bromide Form II at 0.93 GPa ..... 92

# 8. CV TEODORO KLASER

Teodoro Klaser was born in Banja Luka, Bosnia and Herzegovina, on March 20th, 1987 where he spent his childhood. At the age of six he moved to Trento, where he finished elementary school and high school. Teodoro Klaser obtained his master's degree in Physics (Experimental physics) at the Department of Physics, University of Trento. During his work on master's thesis, he was actively participating at the IDEA laboratories which are part of the Department of Physics, where he was working in the field of electrochemistry and photoelectrochemical cells analyzing thin films deposited by Pulsed Laser Deposition. After the graduation, he received an internship at the *Edmund Mach* foundation where he got acquainted with the food quality analysis techniques and olfactometry analysis. In November 2016 he had started his PhD at the Department of Physics, Faculty of Science, University of Zagreb under the supervision of assoc. prof. Željko Skoko. His work was based on study of selected compounds for new actuating materials that provide mechanical motion as response to thermal stimuli – thermosalient crystals. This topic is at the frontier of the contemporary materials science research. With the final aim of elucidation of the thermosalient phenomenon, he used several experimental techniques (structural, microscopic, spectroscopic, thermal, chemical synthesis) with focus in the structural analysis by powder X-ray diffraction. He is a member of the Croatian Crystallographic Society, the Croatian Microscopic Society and Croatian Vacuum Society. Also, he is a member of the State Commission for Competition in Physics. As professor's assistant he held the exercitation for three courses at the Department of Physics. He coordinated and supervised student's laboratory activities (powder XRD and hot-stage microscopy) during their work on master's thesis and investigations for rector's award. During PhD studies he participated at several conferences and meetings where he presented poster and oral lectures, one of which was invited. He was a member of the Scientific and organizing committee of one international scientific conference (Croatian-Slovenian Crystallographic Meeting, 2018, Poreč).

List of publications:

1) Klaser, T.; Popović, J.; Fernandes, J.; Tarantino, S.; Zema, M.; Skoko, Ž. Crystals, 2018, 8, 301.
2) Burazer, S.; Robeyns, K.; Guénée, L.; Mali, G.; Morelle, F.; Ban, V.; Klaser, T.; Filinchuk, Y.; Černý, R.; Popović, J. Cryst. Growth Des., 2021, 21(2), 770

3) Renka, S.; Klaser, T.; Burazer, S.; Mošner, P.; Kalenda, P.; Šantić, A.; Moguš-Milanković, A. (2020). Nanomaterials, 2020, 10(12), 2515
4) Gilja, V.; Živković, I.; Klaser, T.; Skoko, Ž.; Kraljić Roković, M.; Hrnjak-Murgić, Z.; Žic, M. Catalysts, 2020, 10(4), 400
5) Jakovac, M.; Klaser, T.; Radatović, B.; Skoko, Ž.; Pavić, L.; Žic, M. Materials, 2020, 13(24), 5632
6) Vrankić M.; Šarić, A.; Bosnar S.; Barišić. D.; Pajić D.; Lützenkirchen-Hecht D.; Jelovica Badovina I.; Petravić M.; Altomare A.; Rizzi R.; Klaser T. submitted to Inorganic Chemistry, 2021
7) Burazer, S.; Molčanov, K.; Šantić, A.; Klaser,T.; Wenger,E.; Pajić, D.; Jagličić, Z.; Popović, J.; Jurić, M. submitted to Chemical Communication, 2021
8) Jakovac, M.; Klaser, T.; Radatović, B.; Bafti, A.; Skoko, Ž.; Pavić, L.; Žic, M. submitted to Materials, 2021